OPTICAL CHARACTERIZATION OF LIGHT PIPES:

MEASUREMENT, FABRICATION AND MODELING

A Thesis

by

JIANLONG LIN

Submitted to the Office of Graduate and Professional Studies of
Texas A&M University
in partial fulfillment of the requirements for the degree of

MASTER OF SCIENCE

Chair of Committee,	Christi Madsen
Co-Chair of Committee,	Philip Hemmer
Committee Members,	Samuel Palermo
	Aleksei Zheltikov
Head of Department,	Miroslav Begovic

August 2019

Major Subject: Electrical Engineering

ABSTRACT

Light pipes for optical transmission and distribution have been frequently employed in uses such as solar concentrator designs, and one overarching goal is to predict loss mechanisms and minimize these losses. The aim of this work is to detail the fabrication and measurement of fused silica light pipes, and to provide a method of modeling the optical losses based on input characteristics and geometric considerations of waveguide surface features such as roughness. A laser polishing procedure is outlined, and various statistical quantities for rough surfaces, namely root-mean-square height and slope, are described and estimated. The optical transmission of light pipes of different lengths are measured for different wavelengths and incident angles. A geometric optics method utilizing Fresnel's equations of reflection and transmission is developed to model the optical transmission of light pipes as a function of incident angle and surface roughness statistics. Other possible loss mechanisms are also analyzed. It was shown via simulation that root-mean-square slope plays a significant role in determining loss. Based on surface profile measurements of a test sample, we estimate a benchmark root-mean-square slope of 0.015 or lower. For the measured transmission for various samples, we observe a relatively linear loss trend for different incident angles into the light pipe that Fresnel's equations alone cannot account for. We estimate a constant sidewall loss of approximately 0.4% to 0.5% being common in our light pipe samples from an imperfect fabrication process and, to a lesser extent, constant reflectivity loss from light pipe support mounts to account for this observation.

ACKNOWLEDGEMENTS

First and foremost, I would like to thank my advisor Professor Madsen for affording me this opportunity to gain hands on experience in working with optics. Without her support and guidance throughout this project, I would not have been able to achieve this milestone in my academic career and forward my future goals.

I would also like to thank past graduate students Matthew Morrison and Chehao Hu for their training and insight on various aspects of optics and optical instrumentation, and initial guidance on the project respectively. I am grateful to them for sharing their knowledge and wisdom which will guide me throughout my career.

In addition, I would like to thank student technician Sandheep Kumar for his instruction on laser polishing required for this work.

CONTRIBUTORS AND FUNDING SOURCES

Contributors

This work was supervised by Professor Madsen, with a thesis committee consisting of Professor Madsen (chair), Professor Hemmer (co-chair) and Professor Palermo of the Department of Electrical and Computer Engineering, and Professor Zheltikov of the Department of Physics and Astronomy.

Raw data of the surface profile measurements was provided by Professor Madsen. All other work for this thesis was produced by the student independently.

Funding Sources

All work presented in this thesis is funded by the Advanced Research Projects Agency-Energy (ARPA-E).

TABLE OF CONTENTS

Page

LIST OF FIGURES

Page

LIST OF TABLES

Page

1. INTRODUCTION

1.1. Overview

Optical waveguides (“light pipes”) much larger compared to the likes of optical fibers are used in a variety of applications that require light steering and transmission such as daylighting systems [1], [2], light emitting diode (LED) light projection [3] and concentrator photovoltaics (CPV) [4]. Light pipes may come in a variety of configurations and are either hollow core or solid core, in which the former depends on high reflectivity coating within the structure and the latter depends on internal reflection within the material. Figure 1.1 shows examples of possible configurations. Moreover, light pipes can be fabricated with curved structures for the steering of light, or other unique geometries which enable efficient light input and output coupling.

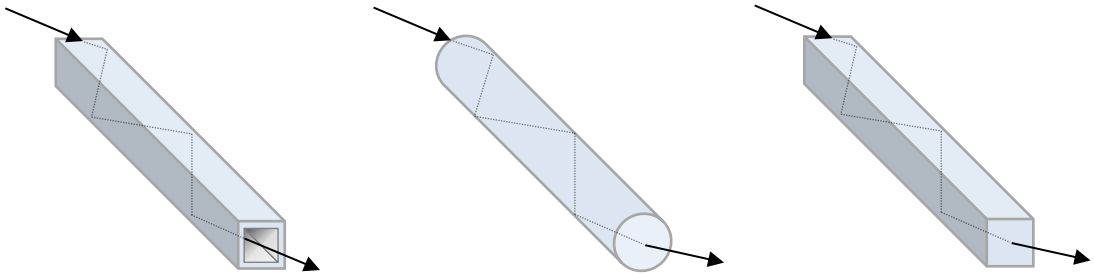

(a) (b) (c)

Figure 1.1 Examples of light pipe configurations; (a) rectangular hollow structure, (b) cylindrical solid core, (c) rectangular solid core

For CPVs, light is collected from a large area and focused to a small photovoltaic cell to realize cost-effective methods of solar energy collection, and often waveguiding structures are incorporated into such designs. This work entails analyzing the loss mechanisms of basic waveguide structures and providing a framework to model losses.

Silica glass as a material has been used for various applications including standard optical components such as lenses, fiber optics and telecommunications, waveguides and solar concentration. For example, a lens array coupled to an optical waveguide array made of fused silica has been recently proposed by our group [5]. Because fused silica has very low absorption in the spectral range 200nm to 3500nm and is practically regarded as transparent in this range [6], it is an ideal material for solar applications. Since approximately 96% of the energy from sunlight lies in the spectral range 270nm to 2600nm [7], fused silica light pipes can be used to collect and redirect solar energy with low attenuation.

To this end, we manufacture fused silica light pipes for guiding light collected on solar concentrators, measure their efficiency, and develop a theoretical model to estimate the losses based on surface structure. The light pipes manufactured have a 1mm x 1mm cross-sectional area and varying lengths. For solar concentrators, it is desirable to fabricate light pipes with minimal optical losses to maximize the light collected. Measuring and modeling losses in light pipes can be a good indicator of the quality of the fabrication process and in assessing possible loss mechanisms. The surfaces of our light pipes often require polishing to minimize the optical losses due to light incident on a non-perfectly smooth surface. To model the losses and assess the quality of the polishing process, a

geometric optics method was developed to estimate the transmission of power through the light pipe with rough sides, and at different incident angles into the light pipe, based on a few statistical measures quantifying roughness.

1.2. Loss Characterization

For light entering a solid core light pipe, the overall power transmission will be a function of various parameters including angle of incidence θ_i and the wavelength dependent complex refractive index of the material $n = \eta + i\kappa$. Here, η is the real component, and the imaginary component $i\kappa$ describes absorption loss and is related to the commonly described attenuation coefficient parameter α (cm^{-1}). Figure 1.2 illustrates a side view depiction of a light ray traveling through a solid core waveguide.

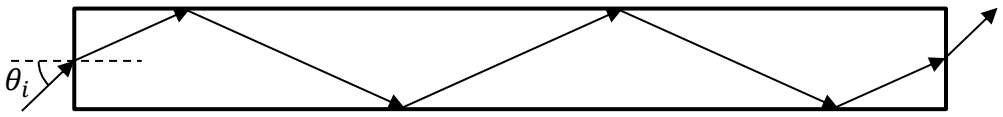

Figure 1.2 Light ray entering and exiting a solid core waveguide

Power loss from reflections depend on the refractive indices of two different mediums at a boundary, and the angle of incidence on that boundary. Assuming a perfect sidewall geometry for a fused silica waveguide, there will be total internal reflection even at grazing incidence into the light pipe where power will not escape from the sidewalls. However, a perfect or near-perfect geometry structure is difficult to achieve. Losses such

as absorption of light by a material also need to be considered for other types of materials, while fused silica has very low absorption.

1.2.1. General Loss Mechanisms

There are several mechanisms for losses within optical waveguides. For straight solid core waveguides, the primary losses are absorption within the material, bulk scattering, scattering at surface and local defects at the surface [8], [9]. Absorption is due to the annihilation of photons in the material where the photon energy is transferred to the subatomic particles, usually quantified by the attenuation coefficient for the material. Bulk scattering spreads the radiated power and arises from imperfections and defect sites within the material while surface scattering is a result of roughness at the sidewalls of the waveguide.

Fused silica glass has a relatively small attenuation coefficient therefore it is neglected in this work. Furthermore, we assume internal and surface defects are minimal; for the latter, sample images of the surface quality under a microscope can be seen in Section 2. We also model the losses of fused silica light pipes with rough surfaces using the geometric optics approach where reflection off the rough surface is a function of the orientation of local surface planes. We treat the problem of modeling losses as a purely geometric optics problem where the reflection and transmission of light at a boundary is determined entirely by Fresnel's equations. An analysis of possible loss mechanisms is provided based on this method.

1.2.2. Roughness Parameters

To characterize the roughness of surfaces, various statistical measures have been commonly adopted. Two quantities that are commonly characterized are the root-mean-square (RMS) height and slope deviations [10]. For a 2-D surface profile $z(x, y)$, the RMS roughness is expressed in Equation 1.1 and the RMS slopes in the x and y directions are expressed in Equation 1.2 and Equation 1.3 respectively

$$\sigma = \lim_{\substack{L_x \to \infty \\ L_y \to \infty}} \sqrt{\frac{1}{L_x L_y} \int_0^{L_y} \int_0^{L_x} (z(x,y) - \bar{z})^2 \, dxdy} \tag{1.1}$$

$$m_x = \lim_{L_x \to \infty} \sqrt{\frac{1}{L_x} \int_0^{L_x} \left(\frac{\partial z(x,y)}{\partial x} - \overline{\frac{\partial z}{\partial x}} \right)^2 dx} \tag{1.2}$$

$$m_y = \lim_{L_y \to \infty} \sqrt{\frac{1}{L_y} \int_0^{L_y} \left(\frac{\partial z(x,y)}{\partial y} - \overline{\frac{\partial z}{\partial y}} \right)^2 dy} \tag{1.3}$$

where a horizontal bar above a variable denotes the average of that variable over the entire surface. The magnitude of the RMS slope we compute as

$$|m| = \lim_{\substack{L_x \to \infty \\ L_y \to \infty}} \sqrt{\frac{1}{L_x L_y} \int_0^{L_y} \int_0^{L_x} \left(\frac{\partial z(x,y)}{\partial x} - \overline{\frac{\partial z}{\partial x}} \right)^2 + \left(\frac{\partial z(x,y)}{\partial y} - \overline{\frac{\partial z}{\partial y}} \right)^2 dxdy} \tag{1.4}$$

We model these parameters in our geometric optics method for generated surfaces with random distributions. The magnitude of the RMS slope is calculated by taking the standard deviation of the magnitude slope at the local points of a discrete surface profile in the model. Figure 1.3 shows a simple depiction of one-dimensional surfaces with

different RMS heights (σ) and slopes (m). RMS height relates to the height elevation of a local point and the "scalability" of the surface, whereas RMS slope describes the local orientation of each surface plane or differential surface area.

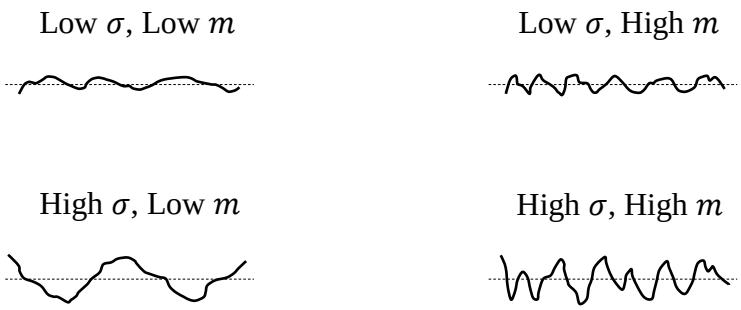

Figure 1.3 Illustration of RMS height σ and slope m

1.2.3. Scattering From Wave Theory

Fundamentally, the scattering of light can be viewed in the picture of an atom or molecule absorbing the energy of an electromagnetic wave and re-radiating energy in different directions. In the macroscopic sense and for the case of surface scattering, residual surface roughness can lead to a significant spread of electromagnetic radiation for light reflected from a rough surface. The ability to characterize rough surfaces plays an important role in many areas of optical science and serves as a benchmark in improving the fabrication technique and performance of optical components.

In a perfectly smooth surface, the power and direction of a plane wave reflected from a surface can be described entirely using the well-established law of reflection and Fresnel's equations. For a surface with residual roughness, the distribution of energy

reflected from the surface in general can be characterized by the summation of a specular and diffuse component [11] as shown in Figure 1.4.

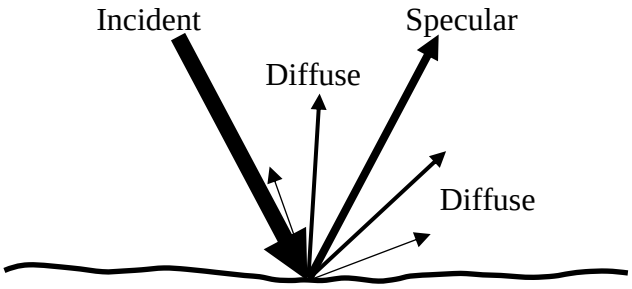

Figure 1.4 Rough surface schematic illustrating reflected specular and diffuse light

The most commonly accepted quantity describing the distribution of reflected light from a surface of arbitrary but isotropic roughness is the Bidirectional Reflectance Distribution Function (BRDF), devised by Nicodemus et al. [12], and is expressed as the differential scattered *radiance* divided by the differential incident surface *irradiance*. The BRDF has units of inverse steradians. Stover [10] expresses this in a simple form for a collimated beam of light incident on a rough surface as

$$\text{BRDF} \equiv \frac{\text{differential radiance}}{\text{differential irradiance}} \approx \frac{dP_s/d\Omega_s}{P_i \cos(\theta_s)} \tag{1.5}$$

Here, P represents power, Ω represents the solid angle, θ represents the angle an incident or reflected ray component makes with the normal to a small illuminated area A, and the subscripts i and s represent the incident and scattered portions respectively. The geometry representing the BRDF is illustrated in Figure 1.5.

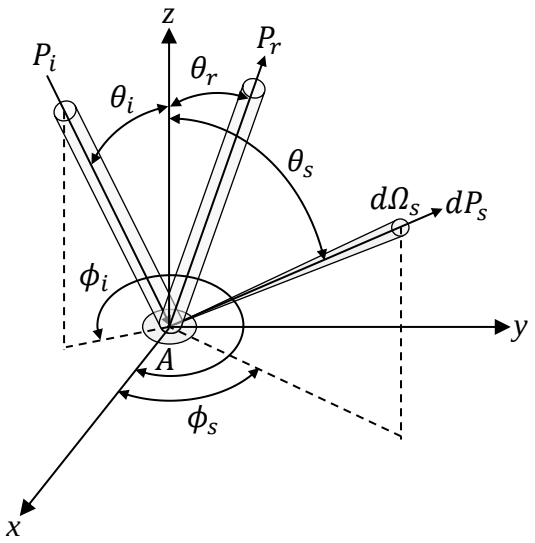

Figure 1.5 Bidirectional Reflectance Distribution Function (BRDF) visualization (Adapted from J. C. Stover, *Optical Scattering: Measurement and Analysis*, 2nd ed. Bellingham: SPIE, 1995. Copyright 1995 by Society of Photo-Optical Instrumentation Engineers)

Similar to the field of signal processing where a signal can be mathematically defined as a summation of sinusoidal components with various amplitudes and frequencies, the Power Spectral Density (PSD) function quantifies the power as a function of the spatial frequencies inherent in the rough surface, and is expressed [13] as

$$PSD(f_x, f_y) = \lim_{\substack{L_x \to \infty \\ L_y \to \infty}} \frac{1}{L_x L_y} \left| \int_0^{L_y} \int_0^{L_x} z(x,y) e^{-j2\pi(f_x x + f_y y)} \, dxdy \right|^2 \tag{1.6}$$

The autocovariance (ACV) function is another way to quantify the surface and the PSD and ACV form Fourier transform pairs. Often, for polished surfaces, the surface is isotropic, and the PSD and ACV are assumed to have Gaussian distributions; however, this is not always the case.

Analytical approximations based on electromagnetic wave theory exist to model the BRDF, such as the Beckmann-Kirchhoff theory and the Rayleigh-Rice theory (and more recently the Generalized Harvey-Shack theory) [14], however the historical models work for different regimes of surface roughness, depending on the ratio σ/λ where σ is the RMS height deviation of the surface and λ is the incident wavelength. For example, as a general statement, the Rayleigh-Rice theory is applicable for the smooth surface limit where $\sigma/\lambda << 1$ [13], [15] and the derived BRDF is directly proportional to the surface PSD. Such theories fall beyond the scope of this thesis; however, the reader is advised to review the literature referenced in this work to gain a more in-depth understanding of the development of such theories.

1.2.4. Geometric Optics Approximation

Using wave-based approaches to determine the scattering effects and its impact on the power distribution over many reflections through a waveguide is rather complicated. Thus, in this thesis, we are not concerned with the wave theory approaches to model the power distribution due to surface scattering through the light pipe. The alternative, the geometric optics approximation to wave theory, is much simpler to implement and is based on tracing a series of rays through the light pipe with a power contribution associated to each ray. We attempt to assess the accuracy of the geometric optics approach in predicting the transmission characteristic of our light pipes. The proposed geometric optics algorithm simulates two rough surface profiles with Gaussian PSDs and ACVs. The model is based on Fresnel's equations for transmission and reflection at a boundary where the overall power transmission out of the waveguide is a function of the dimensions of the light pipe

and roughness parameters such as the RMS height and slope that quantify some of the properties of the polished surface. Figure 1.6 is an illustration of a ray as it passes through the light pipe.

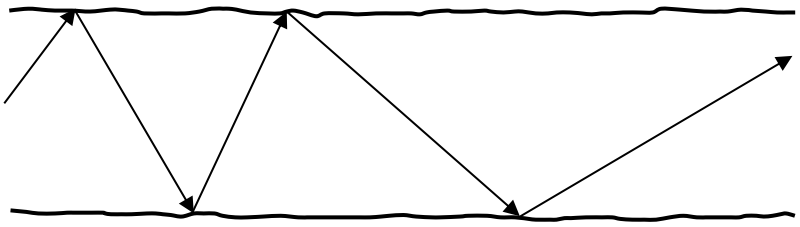

Figure 1.6 Illustration of ray path for rough sidewalls

Power loss from sidewalls with finite roughness is modeled via a reflectivity coefficient described by Fresnel's equations. Using this method, we estimate the roughness parameters based on the measured output power of the light pipes and compare this against our estimates based on surface profile imaging of a light pipe test sample. We expect a higher percentage of losses as incident angle into the light pipe increases and for light pipes with sidewalls that are in general more "rough". Using the geometric optics method, we also determine some general properties including how some additional loss mechanisms can affect the overall power loss trend.

2. WAVEGUIDE FABRICATION

2.1. Fabrication Overview

In order to manufacture light pipes with a 1mm x 1mm cross-section and varying lengths, first a 1mm thick ultra-smooth sheet of silica is purchased commercially. Femtosecond laser irradiation assisted by chemical etching (FLICE), using KOH as the etchant, is used to fabricate light pipes from the sheet [16]. This fabrication process lies outside the scope of this thesis; however, the result is a light pipe with two smooth and two very rough sidewalls, and rough end facets.

This thesis details the polishing step to smoothen the rough sidewalls, to maximize the transmission of the light pipes. Optical polishing using a CO_2 laser is a common technique in fused silica glass polishing including smoothening surfaces and reducing residual defects from grinding such as surface and subsurface damage [17]. Past studies on CO_2 laser polishing of fused silica have also demonstrated to yield a roughness deviation below 0.1nm for spatial wavelengths up to 100μm and 1nm for spatial wavelengths up to 1mm [18]. Thus, CO_2 laser polishing is promising in creating very smooth glass surfaces. A detailed overview of the polishing step is provided along with an analysis of the polishing quality based on microscopic images taken.

2.2. Physical Characteristics

Two of the opposing sides of light pipes with a 1mm x 1mm cross-section and varying lengths require polishing and the other two are smooth sides with negligible roughness. A general diagram of the light pipe is shown in Figure 2.1.

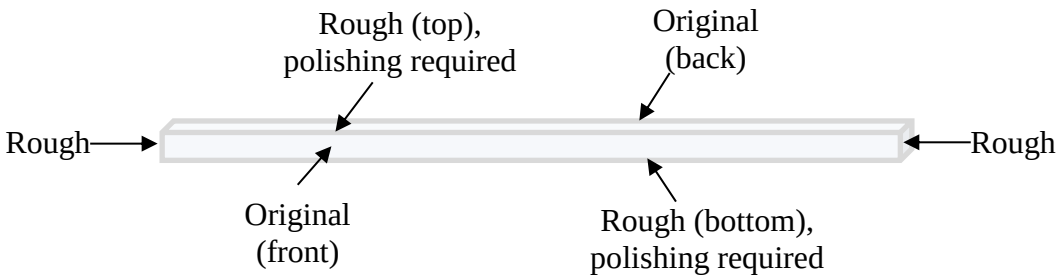

Figure 2.1 Fused silica light pipe design

After the CO_2 laser polishing step, we like to analyze the quality of the polishing process; thus, we analyze the homogeneity of the polished structure under a microscope and profilometer and observe for defects that may arise as a result of the polishing procedure. Figure 2.2 is an illustration of a sub-micron level height deviation of a light pipe after polishing the two rough sides.

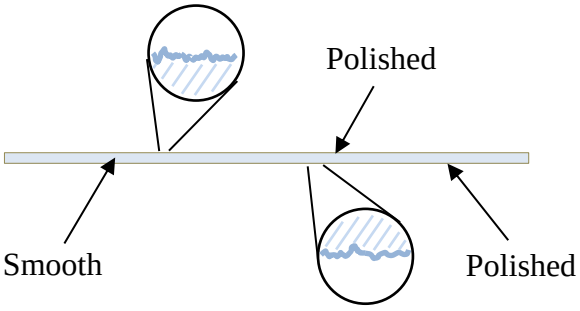

Figure 2.2 Light pipe with two polished sides with micro-roughness and two smooth sides

Currently it is still a challenge to polish the ends, thus we commonly attach smooth commercially purchased thin BK7 glass sheets ("cover slips") to the ends of the light pipes using ultraviolet (UV) cured optical adhesive index matched to the light pipe to reduce the diffraction effects due to rough faces, as shown in Figure 2.3.

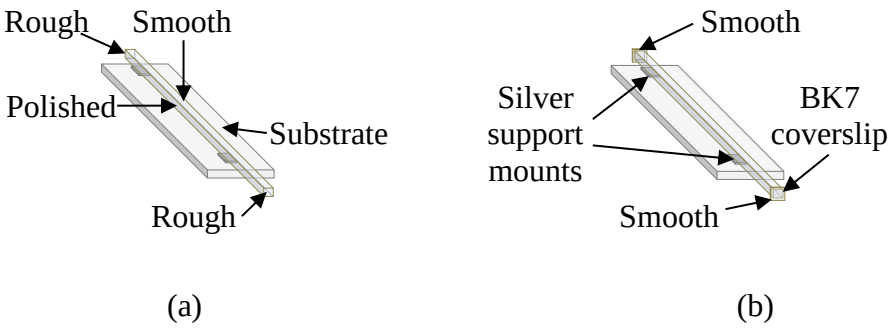

Figure 2.3 Light pipe mounted on substrate; (a) without BK7 cover slip, (b) with BK7 cover slip

The light pipe is suspended by two silicon dioxide coated silver support mounts on a glass substrate and joined using index matching adhesive. The polished sidewalls face the side while the originally smooth sidewalls are parallel to the support mounts and substrate. We test the sides perpendicular to the glass substrate by changing the incident angle on one end of the light pipe in the same plane as the glass substrate. For example, we have the light pipe mounted such that the smooth sides are parallel to the silver support mount and substrate platform to test the transmission characteristics of the polished sides.

2.3. Fabrication Setup

We polish the rough sides of light pipes using a high-powered CO_2 laser and a series of automation stages controlled by a graphical user interface. The power output of the CO_2 laser is automatically adjusted based on a feedback loop between a video recorder capturing the intensity of the beam on the rough surface and a control algorithm. Figure 2.4 shows a simplified view of the steering and focusing of the laser beam onto a light pipe placed on a platform.

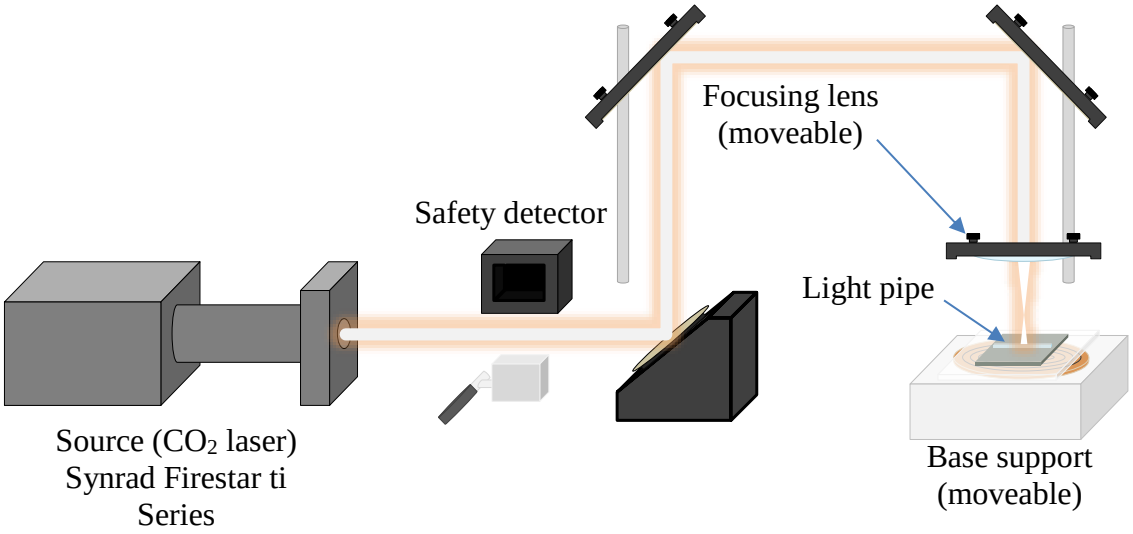

Figure 2.4 Fabrication setup illustration

The light pipe is placed on top of an aluminum nitride plate supported by a glass platform, thermally conductive plate and base support. We use automated translational stages to adjust the horizontal position of the base support platform and vertical position of the focusing lens to control the laser location and intensity respectively.

The total power of the source is measured using the Thorlabs PM100D power meter console. A heating unit is connected to the base support platform to control the temperature gradient between the light pipe and the focused point of the laser. Cameras are placed near the platform to record the polishing process.

Several safety control mechanisms are also in place to ensure the laser is focused on the correct spot, or to steer the laser off to a side detector. Figure 2.5 shows a mirror flipped by an automated stage to steer the laser towards a side detector acting as a heat sink. This is primarily used for laser power stabilization purposes and to abruptly stop the polishing process if necessary.

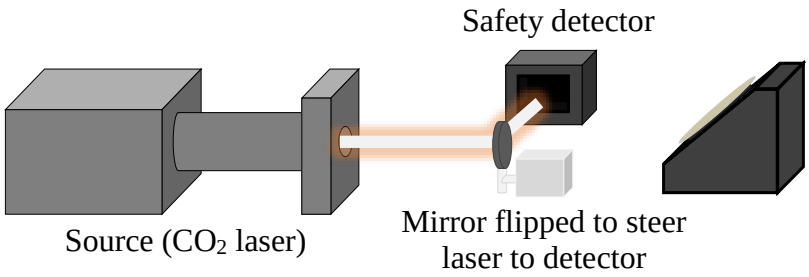

Figure 2.5 Safety mechanism to block laser source

2.4. Polishing Procedure

We follow the general steps below to polish light pipe samples.

1. Clean a light pipe sample using a cleaning fluid such as isopropanol.
2. Place the sample on an aluminum nitride plate, as in Figure 2.4, with the rough side facing up.

3. Turn on the power supply for the CO_2 laser. (Note: The laser itself is not powered initially; this is controlled using a graphical user interface.)
4. Ensure the laser's diode pointer is centered towards a side detector. (Note: A diode pointer installed on the laser source is used to determine the would-be location of the high-powered beam. This is a safety mechanism.)
5. Use the automation software to align the platform and lens. The lens is usually positioned approximately 65mm above the sample.
6. Steer the diode pointer towards the platform by controlling the orientation of the mirror stage.
7. Place a dispensable plate on the platform and use the software to mark a spot on the plate to determine the beam position. (Note: The laser power is controlled using software. The laser beam is turned on and then quickly turned off.)
8. Redirect the laser so that the diode pointer is off to the side detector. Turn on the laser and set the power to a desired value for polishing. The laser power will begin to stabilize while it is on. (Note: We currently use 25W for the polishing.)
9. Turn on the heating unit and adjust the temperature so that the platform is heated to approximately 350ºC.
10. Once the laser power is stable as seen using the Thorlabs PM100D power meter, begin polishing by setting the beam location on one end of the light pipe and using the software to control the speed and end position for the translational stage for the platform. (Note: Currently we use a polishing speed of 0.1mm/s.)
11. Turn off the laser and heating unit, and all other devices.

2.5. Polishing Quality

2.5.1. Current Polishing Results

We can achieve relatively defect-free polishing on the surface. Figure 2.6 shows the quality of our recent polished light pipes as viewed under a Lumenera Infinity microscope. Minimal defects are seen under the microscope on the smooth and polished sides. Completing a polish without inducing any observable defects is a crucial step to achieving high transmission, as past results indicate very poor transmission for light pipes with defects formed on smooth sides after polishing. While we consider this a milestone, so far the structural integrity and overall shape of the surface, including any potential ablation as a function of the CO_2 laser power, has not been investigated.

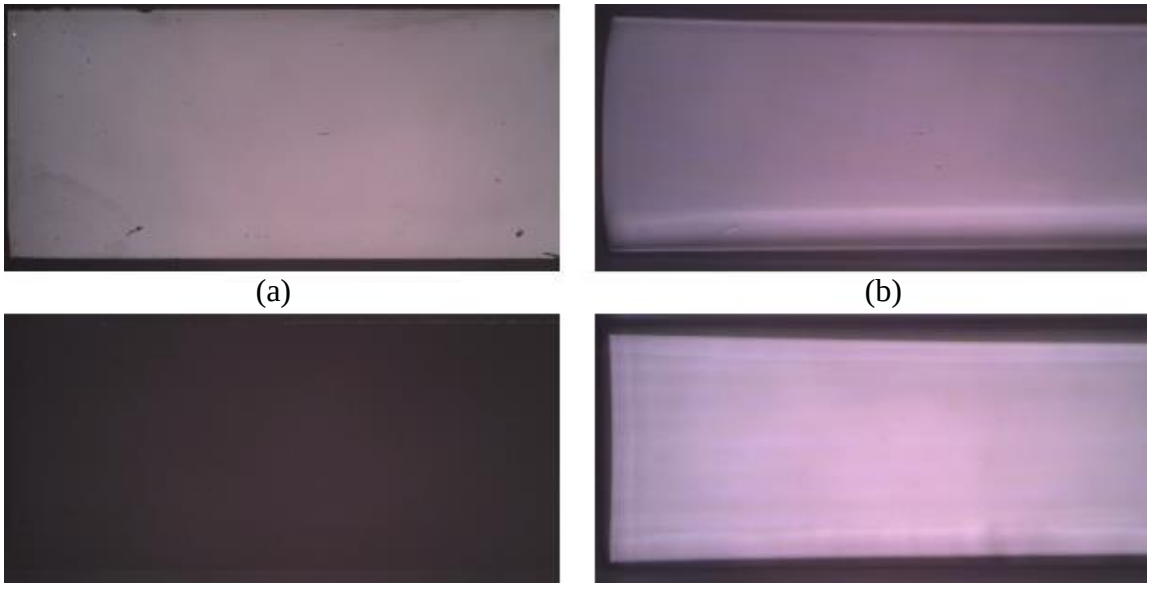

Figure 2.6 Current polishing quality; (a) original – before, (b) original – after, (c) unpolished, (d) polished

Previously, light pipes were placed on top of a glass plate, sandwiched between two aluminum nitride plates, and defects on our past light pipe samples were observed under a microscope. Figure 2.7 shows one past result under a Lumenera Infinity microscope. We are now able to minimize the formation of defects during polishing by minimizing the dust particles on the light pipes prior to polishing, as we observed that dust particles on the smooth surfaces result in an increased risk of forming defects on those locations. The key step we have discovered is, while continuously viewing under a microscope, to carefully wipe the surface until no dust particles are visible for all four sides.

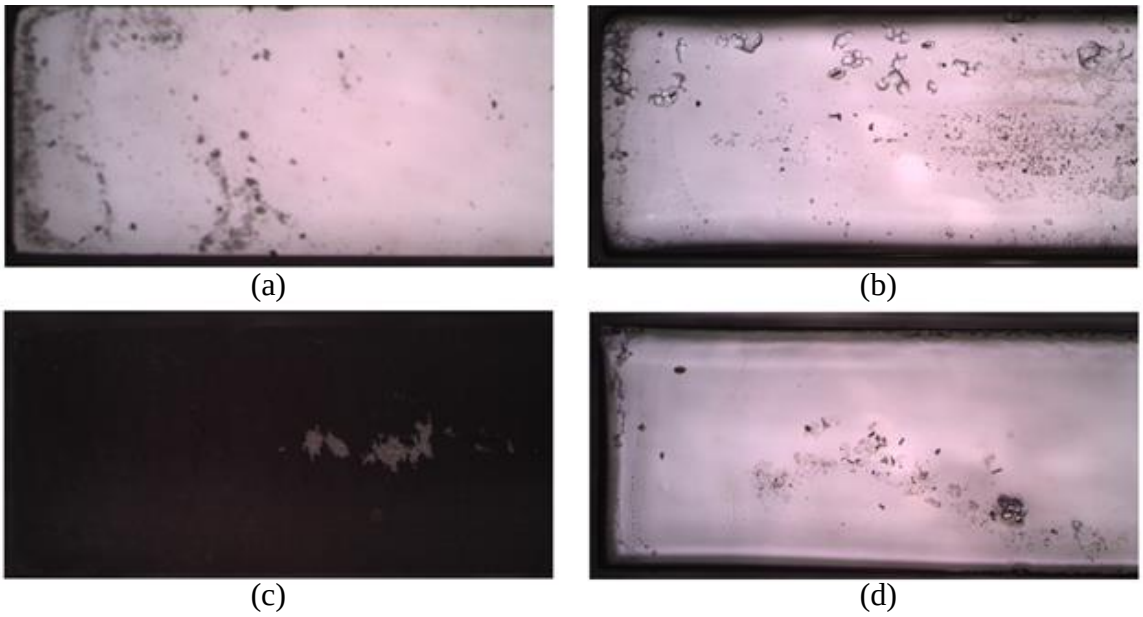

Figure 2.7 Past polishing quality; (a) original – before, (b) original – after, (c) unpolished, (d) polished

2.5.2. Additional Polishing Considerations

Although we can successfully minimize the formation of defects during polishing, other potential issues observed during the procedure remain. A camera is placed near the base support platform to record the polishing process . In some rare occasions, some areas on the light pipe may be subject to an abrupt, sharp increase in intensity while the CO_2 power remains constant. This is presented as an intense glow on the camera and an increase in the pixel count on the control software. Figure 2.8 shows a segment of the light pipe being polished illustrating this behavior.

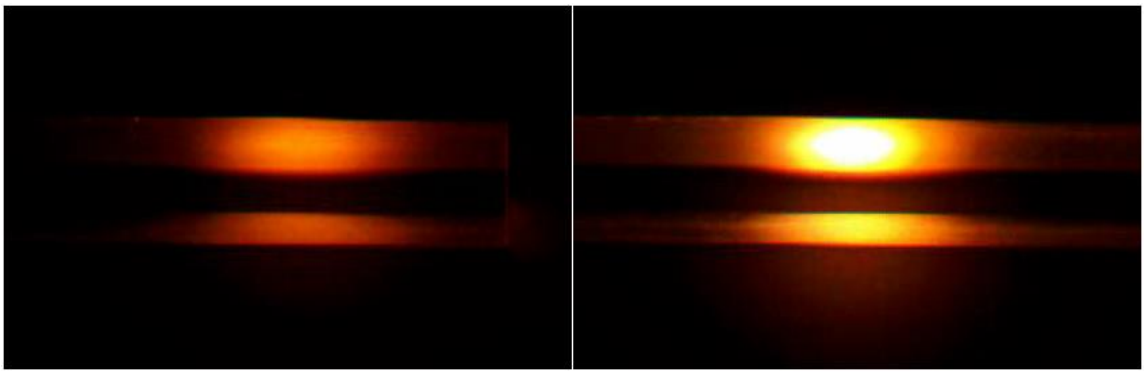

(a) (b)

Figure 2.8 Video snapshot of polishing process; (a) normal glow, (b) abrupt increase in intensity

The light pipe in Figure 2.8(a) is being polished normally via the automated movement of the base support platform. Occasionally an unexpected sharp increase in the intensity of the glow caused by the laser is seen as shown in Figure 2.8(b). This is problematic, as a prolonged exposure can result in a deformation in the area affected or,

worse, a fracture. We use a software to redirect the laser to the safety detector to temporarily halt the polishing process as soon as an abrupt increase in intensity is detected. This reduces the chance of a deformation occurring.

2.6. Profilometer Imaging

To assess the height distribution of the polished surfaces and estimate RMS roughness parameters, local images of the polished surfaces were taken using the Filmetrics Profilm3D profilometer. Some statistical results are presented in Section 5. The profilometer captures the surface height distribution of an area of approximately 200µm by 300µm using white light interferometry. Figure 2.9 shows a few examples of the images taken for a test sample of 40mm in length for the polished surface.

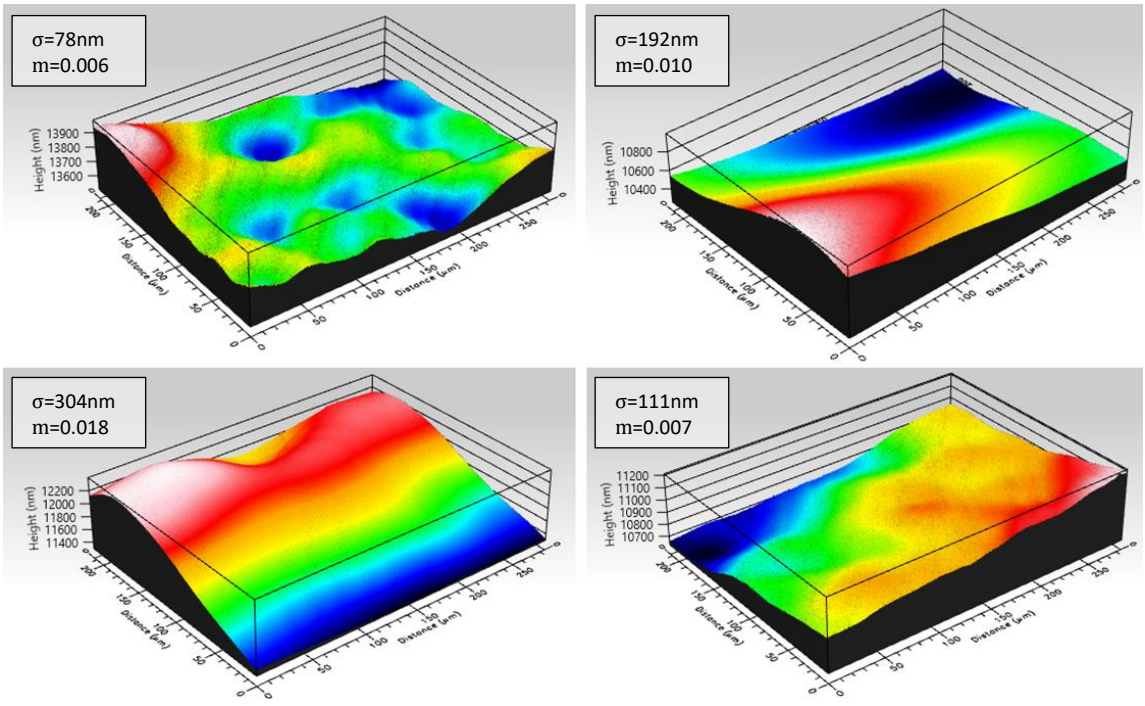

Figure 2.9 Profilometer image examples for polished surface

Figure 2.10 shows two examples of the smooth side of the light pipe as imaged by the profilometer. Based on the relatively low deviation of the smooth side compared to the polished sides, we treat the smooth sides as perfectly smooth, ideal sidewalls.

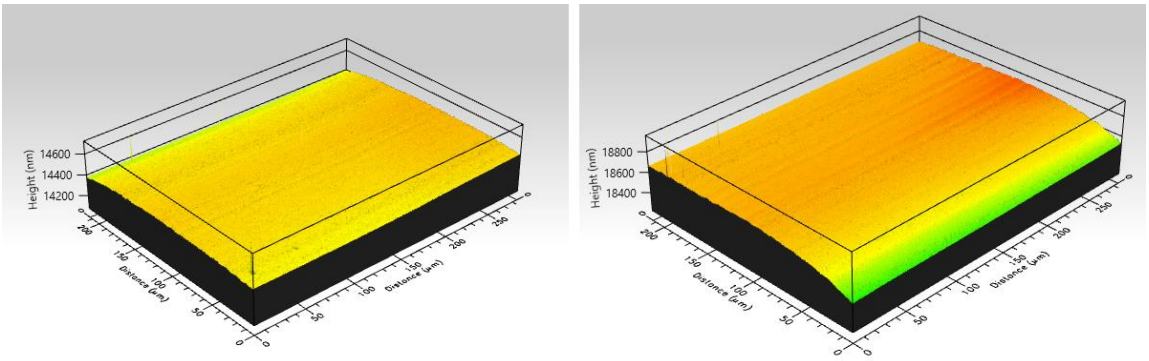

Figure 2.10 Profilometer image examples for smooth surface

3. WAVEGUIDE MODELING

3.1. Modeling Overview

The problem of determining the power output through an optical waveguide using the geometric optics method can be viewed as tracing a set of rays through a cuboid with a very large length in comparison to the width and height. Two sidewalls have finite spatial deviation after polishing and two are assumed to be perfectly smooth. The end facets are also perfectly smooth. The roughness is assumed to be isotropic with Gaussian PSDs and ACVs as described in Section 1 and is simulated as so.

The output power is primarily a function of the roughness parameters i.e. RMS slope and height, the refractive index η of the light pipe for a particular wavelength and the incident angle into the light pipe. Fresnel's equations for reflection and transmission are used to model the loss through the light pipe at any particular boundary.

The algorithm is developed in MATLAB. We test an ensemble of trials each having randomly generated rough surface profiles and average the results to obtain the expected transmission over a range of incident angles.

3.2. Surface Profile Generation

Two sides of the light pipe are modeled as rough surfaces due to imperfect fabrication and polishing. The surfaces are assumed to have random Gaussian distributed height variations. MATLAB is used to generate a N_x by N_y matrix for each rough surface containing the height deviations for that surface. Figure 3.1 shows a depiction of how we currently choose to model our surface.

First, the surface is generated using MATLAB's *randn* function to create a normally distributed set of random numbers, given by

$$Z = \sigma * \text{randn}(N_x, N_y) \tag{3.1}$$

where σ is the RMS height deviation of the surface. Each point in Z has a separation of $\Delta d = \frac{W}{N_x - 1} = \frac{L}{N_y - 1}$ where W and L is the width and length of the light pipe respectively. Each area within the grid is further divided into triangles as shown in Figure 3.2.

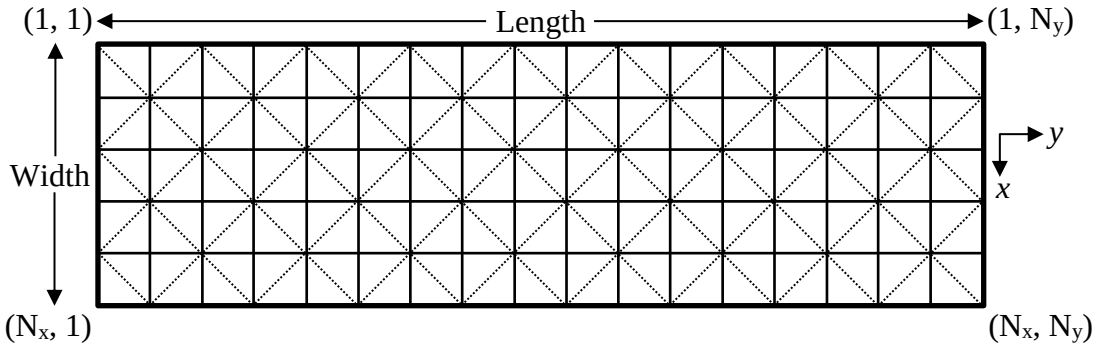

Figure 3.1 Grid representation of a rough surface

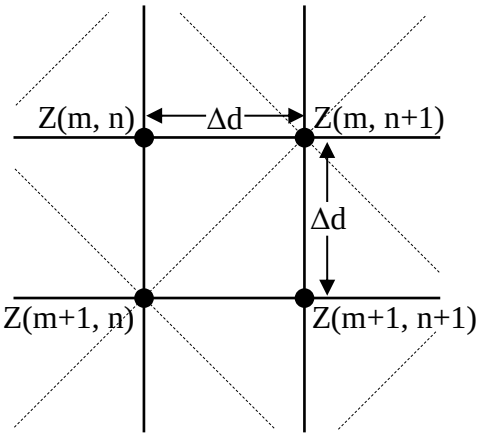

Figure 3.2 Rough surface sub-grid

We model our surface this way primarily (a) to ensure the rough surface is well defined geometrically such that, within a local set of points, the location of reflection from the surface can be determined easily, for example there are no step discontinuities within the piecewise surface, and (b) so that each local planar surface is defined by three points on that surface.

To achieve spatial correlation for the surface with both the PSD and ACV taking the form of a Gaussian distribution, Z is convoluted with a Gaussian filter [19], [20] with impulse response

$$G = \exp\left(-\left(\frac{2x^2}{\ell_x} + \frac{2y^2}{\ell_y}\right)\right) \tag{3.2}$$

by using MATLAB's FFT2 and IFFT2 algorithms, and considering the Nyquist criterion in the spatial domain, in which the following condition must be satisfied

$$\frac{N}{L} > \frac{2}{\ell} \tag{3.3}$$

where N/L is the number of grid points per unit length and ℓ is the correlation length. Figure 3.3(a) shows an example of a raw 500μm x 500μm surface, with grid separation Δd of 5μm, generated by MATLAB using the *randn* function compared to the case where the surface is convoluted with a Gaussian filter in Figure 3.3(b)-(d). For a surface with the aforementioned correlated properties, the RMS height σ, RMS slope m and correlation length ℓ have the following relationship $m_x = \sqrt{2}\sigma/\ell_x$ and $m_y = \sqrt{2}\sigma/\ell_y$ as $\Delta d \to 0$, and the subscripts x and y denote the direction. For the case where the surface is isotropic, $\ell_x = \ell_y$, $m_x = m_y$ and the magnitude of the slope $m = \sqrt{2}m_x = \sqrt{2}m_y$.

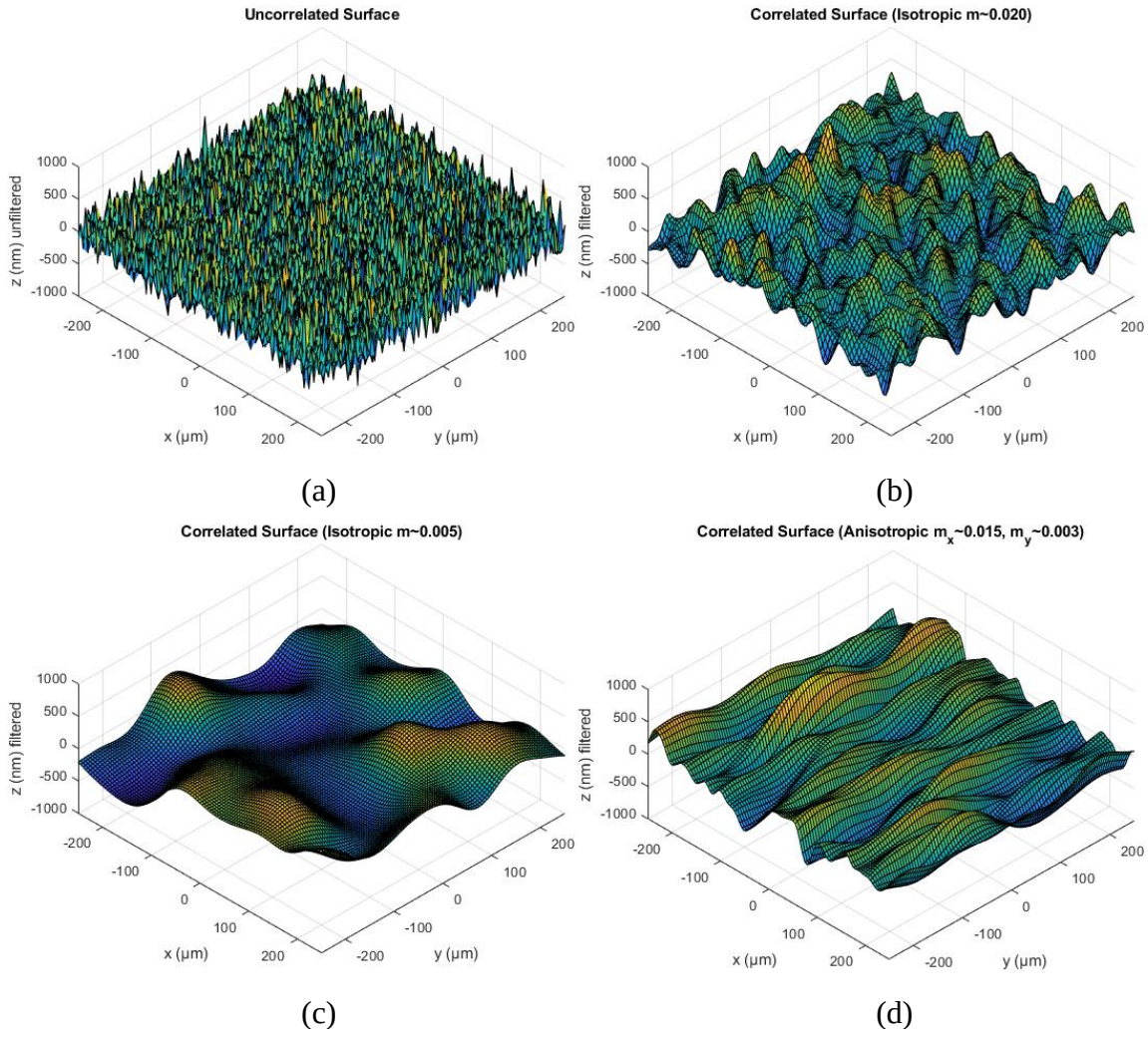

Figure 3.3 Surface profile generation with normally distributed heights using *randn* function (σ=200nm); (a) uncorrelated, (b) isotropic m~0.020, (c) isotropic m~0.005, (d) anisotropic m_x~0.015 m_y~0.003

The RMS slope m in Figure 3.3(b) is higher than that in Figure 3.3(c), i.e. the correlation length ℓ in Figure 3.3(b) is lower; thus, it is easy to simulate surface profiles with varying levels of "smoothness" by changing ℓ. Figure 3.3(d) shows an anisotropic

surface, i.e. $\ell_x \neq \ell_y$. In this work, we treat polished surfaces as being isotropic with the intention of investigating and accounting for anisotropy in the near future.

3.3. Source Simulation

The source is modeled as a distribution of spatially separated wavevectors resembling a Gaussian beam. The wavevectors originate from a point behind the source with angular spread based on the calculated divergence half angle of the beam. Figure 3.4 depicts a distribution of rays entering the light pipe.

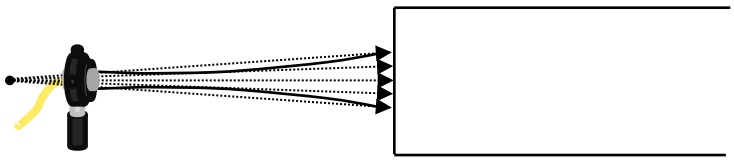

Figure 3.4 Illustration of beam ray tracing for input source

The electric field and intensity of a Gaussian beam are expressed by the following proportionalities respectively [21].

$$E(r,z) \propto \exp\left[-\left(\frac{r}{w(z)}\right)^2 + j\left(kz - \arctan\left(\frac{z}{Z_R}\right) + \frac{kr^2}{2R(z)}\right)\right] \tag{3.4}$$

$$I(r,z) \propto \exp\left[-2\left(\frac{r}{w(z)}\right)^2\right] \tag{3.5}$$

The important parameters are the beam radius $w(z)$ and radius of curvature $R(z)$ at a position z along the optical axis from the beam waist, expressed in the following equations respectively

$$w(z) = w_0\sqrt{1 + \left(\frac{z}{z_R}\right)^2} \tag{3.6}$$

$$R(z) = z\left[1 + \left(\frac{z_R}{z}\right)^2\right] \tag{3.7}$$

where w_0 is the radius at the waist of the beam and the Rayleigh range $z_R = \frac{\pi w_0^2}{\lambda}$. First, w_0 for the source is measured. The parameters $w(z)$ and $R(z)$ are then calculated. The calculated point of origin of the rays, labelled as S' in Figure 3.5, is dependent on $R(z)$, with the divergence angle dependent on both $w(z)$ and $R(\mathrm{z})$. Figure 3.5 shows one ray with divergence half angle θ entering the light pipe. Note that each ray is modeled from the same radius of curvature as an approximation. For example, the direction of a diverging ray representing the $1/e^2$ intensity is computed from $R(z)$ at position *z for the central ray*.

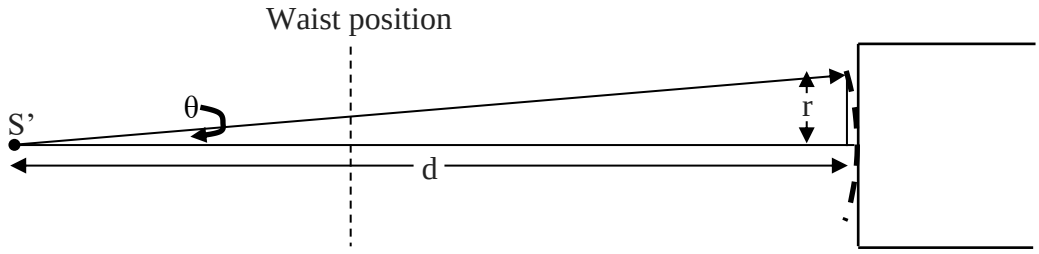

Figure 3.5 Ray representing Gaussian beam as a function of the waist radius and radius of curvature at the input facet

For the simulation, we can choose to model any set of discrete rays representing a Gaussian beam with one ray representing the center of the beam and a set of rays with less

relative intensity at a radial distance r from the center as seen from the cross-section. Figure 3.6, showing a cross-section of a simulated beam, illustrates this concept where the dots represent rays originating from a point and the intensity and divergence relates to the radius from the central ray that coincides with a Gaussian beam.

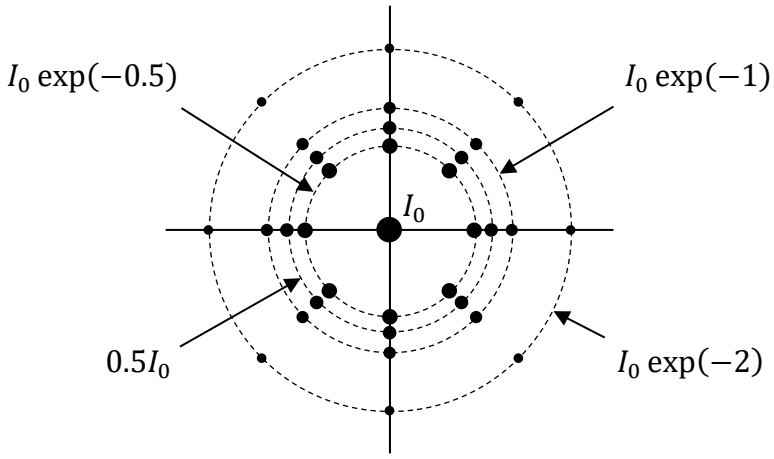

Figure 3.6 Example cross-section of discrete rays originating from a point source with Gaussian intensity distribution

First r, or $I(r, z)$ *relative* to the central ray, is chosen and the remaining parameter can be computed using Equation 3.5. The divergence half angle θ for each ray is computed using Equation 3.8 where *d* is the calculated radius of curvature for the ray along the optical axis.

$$\theta = \tan^{-1}\left(\frac{r}{d}\right) \tag{3.8}$$

The beam radius $w(z)$ representing $1/e^2$ intensity at the input can also simply be set to any chosen value and the intensity distribution can be computed for any arbitrary

radius. The position of the source, based on the radius of curvature, can also be manually set to adjust the divergence angle into the light pipe. Each ray contributes to the average output power based on their respective intensities and is summed at the output. The overall transmission is a ratio of the total power output compared to the input.

3.4. Geometric Formulism

3.4.1. Incident Ray

Suppose the ray vector $\hat{\mathbf{v}}$ is defined in a spherical coordinate system, as shown in Figure 3.7, and y is the direction along the length of the light pipe. The ray vector $\hat{\mathbf{v}}$ in terms of θ and φ can then be expressed as

$$\hat{\mathbf{v}} = \sin(\theta)\sin(\varphi)\,\hat{\mathbf{x}} + \cos(\theta)\,\hat{\mathbf{y}} + \sin(\theta)\cos(\varphi)\,\hat{\mathbf{z}} \tag{3.9}$$

The angle θ then primarily controls the incident angle into the light pipe, and φ can be adjusted to control the direction as viewed from a cross-section of the beam.

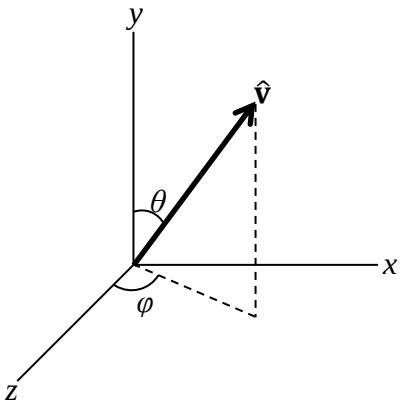

Figure 3.7 Ray tracing coordinate system

3.4.2. Reflection And Transmission

To compute the new direction of a ray as it reflects from, or transmits through, the boundary between two different mediums, we first consider the incident ray $\hat{\mathbf{v}}_\mathbf{i}$, the normal vector $\hat{\mathbf{n}}$ to a microscopic planar surface, and the angle θ_i that $\hat{\mathbf{v}}_\mathbf{i}$ makes with $\hat{\mathbf{n}}$. The Law of Reflection states that $\theta_i = \theta_r$ where θ_i is the incident angle and θ_r is the reflected angle. Snell's Law describes the refraction of light at the boundary between mediums with refractive indices η_1 and η_2 and is expressed as

$$\eta_1 \sin(\theta_i) = \eta_2 \sin(\theta_t) \tag{3.10}$$

Figure 3.8 shows the refracted and reflected rays at a boundary.

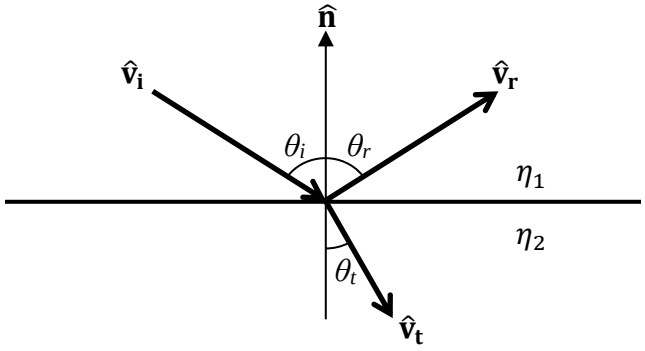

Figure 3.8 Reflection and refraction at a boundary

By splitting the vectors for the incident, reflected, and refracted rays, denoted as $\hat{\mathbf{v}}_\mathbf{i}$, $\hat{\mathbf{v}}_\mathbf{r}$, $\hat{\mathbf{v}}_\mathbf{t}$ respectively, into normal and parallel components with respect to the boundary, the reflected and refracted rays can be computed using the following equations [22].

$$\hat{\mathbf{v}}_\mathbf{r} = \hat{\mathbf{v}}_\mathbf{i} - 2(\hat{\mathbf{v}}_\mathbf{i} \cdot \hat{\mathbf{n}})\hat{\mathbf{n}} \tag{3.11}$$

$$\hat{\mathbf{v}}_\mathbf{t} = \frac{\eta_1}{\eta_2}\hat{\mathbf{v}}_\mathbf{i} + \left(\frac{\eta_1}{\eta_2}(-\hat{\mathbf{v}}_\mathbf{i} \cdot \hat{\mathbf{n}}) - \sqrt{1 - \left(\frac{\eta_1}{\eta_2}\right)^2 (1 - (-\hat{\mathbf{v}}_\mathbf{i} \cdot \hat{\mathbf{n}})^2)}\right)\hat{\mathbf{n}} \tag{3.12}$$

Note that $\hat{\mathbf{v}}_\mathbf{i}$, $\hat{\mathbf{v}}_\mathbf{r}$, $\hat{\mathbf{v}}_\mathbf{t}$, and $\hat{\mathbf{n}}$ in the above equations are normalized vectors, and the direction of $\hat{\mathbf{n}}$ is always towards the first medium with refractive index η_1.

The angle of incidence θ_i is simply computed as

$$\theta_i = \cos^{-1}(-\hat{\mathbf{v}}_\mathbf{i} \cdot \hat{\mathbf{n}}) \tag{3.13}$$

from the dot product rule $\mathbf{v} \cdot \mathbf{n} = \|\mathbf{v}\|\|\mathbf{n}\|\cos(\theta)$ where θ is the angle between $\mathbf{v}$ and $\mathbf{n}$.

Upon a reflection at a boundary, the reflectivity and hence power loss is calculated. It is well established that the reflected power is governed by Fresnel's equations for reflectivity [23] represented as

$$R_s = \left(\frac{\eta_1 \cos(\theta_i) - \eta_2 \cos(\theta_t)}{\eta_1 \cos(\theta_i) + \eta_2 \cos(\theta_t)}\right)^2 \tag{3.14}$$

$$R_p = \left(\frac{\eta_1 \cos(\theta_t) - \eta_2 \cos(\theta_i)}{\eta_1 \cos(\theta_t) + \eta_2 \cos(\theta_i)}\right)^2 \tag{3.15}$$

where R_s is the s-polarized reflectivity and R_p is the p-polarized reflectivity. The term $\cos(\theta_t)$ can also be expressed as $\sqrt{1 - \left(\frac{\eta_1}{\eta_2}\sin(\theta_i)\right)^2}$ using Snell's Law and the trigonometric identity $\cos^2(\theta) + \sin^2(\theta) = 1$. The s- and p-polarized transmission is then computed as $T_s = 1 - R_s$ and $T_p = 1 - R_p$ respectively. For unpolarized light, we take the average reflectivity as $R = (R_s + R_p)/2$ and the transmission as $T = 1 - R$.

As light, while confined within the light pipe, makes a reflection from a light pipe to air interface, i.e. as light goes from a medium with high refractive index to low refractive index, we need to consider the critical angle defined as

$$\theta_c = \sin^{-1}\left(\frac{\eta_{air}}{\eta_{pipe}}\right) \tag{3.16}$$

If the incident angle is below the critical angle, the reflectivity is calculated from Fresnel's equations. If the incident angle is equal to or above the critical angle, the reflectivity is set to unity in the algorithm due to total internal reflection.

3.4.3. Reflection Tracing For Rough Surface

To compute the reflection from a planar surface, the vector normal to the surface must be calculated. Consider a reflection on a planar surface where the plane is defined by points $\mathbf{p_1}$, $\mathbf{p_2}$, and $\mathbf{p_3}$, as shown in Figure 3.9.

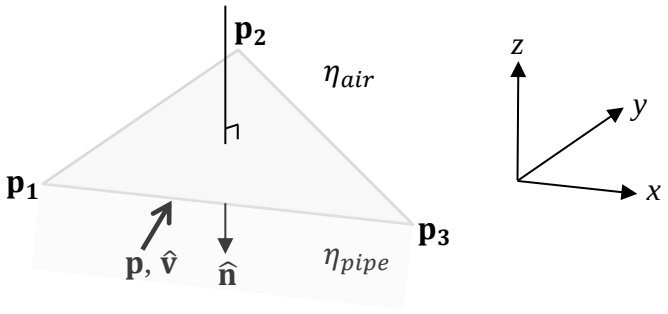

Figure 3.9 Simulated local planar representation showing ray intersection

The vector normal to the plane $\hat{\mathbf{n}}$ is then computed as the following

$$\hat{\mathbf{n}} \equiv \frac{\mathbf{n}}{\|\mathbf{n}\|} = \frac{(\mathbf{p_2} - \mathbf{p_1}) \times (\mathbf{p_3} - \mathbf{p_1})}{\|\mathbf{n}\|} \tag{3.17}$$

where $\hat{\mathbf{n}}$ is a unit vector and $\|\mathbf{n}\|$ is shown to indicate that $\mathbf{n}$ is converted to a unit vector in the algorithm. $\hat{\mathbf{n}}$ is always towards the light pipe medium.

In the algorithm, it is possible for a ray to reflect at the boundary between two or more planar surfaces. For example, suppose a ray confined within the light pipe hits a point shared by two or more planes, denoted as $\mathbf{p_0}$ in Figure 3.10.

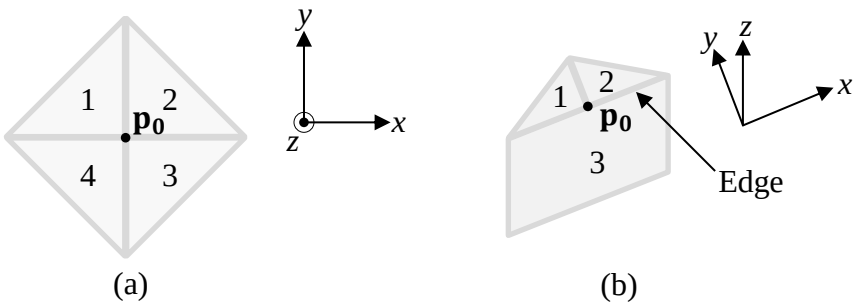

Figure 3.10 Ray intersection on grid point; (a) on a grid point along a rough surface, (b) on an edge point

The final normal vector $\hat{\mathbf{n}}$ is then taken as the mean of each normal unit vector for all adjacent planes. This is expressed in the equation below, where $\|\mathbf{n}\|$ indicates that the final vector is converted to a unit vector.

$$\hat{\mathbf{n}} \equiv \frac{\mathbf{n}}{\|\mathbf{n}\|} = \frac{\sum_{i=1}^{N} w_i \hat{\mathbf{n}}_\mathbf{i}}{\|\mathbf{n}\|} \tag{3.18}$$

$\hat{\mathbf{n}}_\mathbf{i}$ is the unit vector normal to the *i*-th plane the ray intersects. Appropriate weightage w_i is given to each plane to ensure fair contribution based on the proportional

area of each plane when viewed as a revolution around the central point $\mathbf{p_0}$. For example, in Figure 3.10(a), for planes 1 to 4, $w_1 = w_2 = w_3 = w_4$, and in Figure 3.10(b), for planes 1 to 3, $w_1 = w_2 = w$ and $w_3 = 2w$ as plane 3 can be viewed as a combination of two planes with unit vectors $\hat{\mathbf{n}}_3$.

3.4.4. Position Tracing

The ratio of the closest distance from one point $\mathbf{p}$, to a point on a plane $\mathbf{p_{plane}}$, to the magnitude of the directional vector $\hat{\mathbf{v}}$ perpendicular to the plane is expressed as

$$t = \frac{(\mathbf{p_{plane}} - \mathbf{p}) \cdot \hat{\mathbf{n}}}{\hat{\mathbf{v}} \cdot \hat{\mathbf{n}}} \tag{3.19}$$

Equation 3.19 is used to calculate the number of "unit steps" that the ray takes to reach a specific plane, and thus allows us to determine which plane the ray will hit from a series of local planes. The new position of the ray $\mathbf{p_{new}}$ is then expressed in Equation 3.20 as

$$\mathbf{p_{new}} = \mathbf{p} + \hat{\mathbf{v}} * t_{min} \tag{3.20}$$

where t_{min} is the number of unit steps corresponding to the plane that the ray will reach first, ignoring the case where the current position of the ray $\mathbf{p}$ is already on a plane. Values such as incident angle, reflectivity, etc., are then calculated.

3.5. Ray Tracing Procedure

The procedure for estimating the total transmission through a light pipe is briefly summarized with the following steps.

1. Generate new rough surface profiles for two sides of the light pipe with a specified RMS height and slope for each.

2. Set the refractive index corresponding to a particular wavelength.
3. Set the incident angle.
4. Assign a power value to a ray or set of rays and total the values.
5. Trace the ray or set of rays through the light pipe to the output using Fresnel's equations and geometric vector formulas and around the light pipe until the relative power of each ray falls below a threshold, e.g. 0.5%. Sum the relative power contribution for each ray at the output. Divide this value by the original value in Step 3 to obtain the transmission for a particular incident angle.
6. Repeat Steps 3 to 5 to determine the transmission for a range of incident angles.
7. Repeat Steps 2 to 6 to determine the transmission for a range of wavelengths and incident angles.
8. Repeat Steps 1 to 7 over many iterations ("runs") with the same RMS height and slope and average the results to determine the expected transmission for each wavelength and incident angle for a given set of statistical parameters.

Figure 3.11 illustrates the simulation for a given ray entering the light pipe. Each boundary interaction is determined by Fresnel's equations and the ray is traced through the light pipe including for several iterations until there is negligible power remaining that would contribute to the overall output.

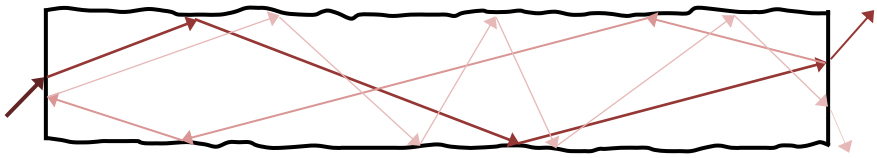

Figure 3.11 Ray tracing of incident ray for power output modeling

3.6. Simulation Properties

Here, we define an iteration ("run") as generating a random light pipe structure with a specified RMS height σ and slope m for two sidewalls and tracing a set of rays through for power estimation. For the following simulations, the results shown are an average from 100 runs using the same σ and m for each run. The rays traced is the same as depicted in Figure 3.6.

Table 3.1 shows the refractive indices for fused silica and BK7 over the wavelength range of 500nm to 700nm used for the simulation. The values are obtained in the database in [24] and [25]. The refractive index of air is 1.

Table 3.1 Refractive index values for fused silica and BK7

Wavelength (nm)	Fused Silica	BK7
500	1.4623	1.5214
600	1.4580	1.5163
700	1.4553	1.5131

3.6.1. General Characteristics

Figure 3.12 shows the estimated transmission of a 50mm light pipe as a function of incident angle and wavelength for two sides with isotropic surfaces and RMS heights (σ) and slopes (m) of 200nm and 0.015 respectively. The simulation shows little to no wavelength dependent behavior due to a small difference in the refractive index change for fused silica between 500nm and 700nm.

The standard deviation between a set of runs depends on the number of rays traced, with more rays lowering the standard deviation. Adopting Figure 3.6 (33 rays total), Table 3.2 shows the standard deviation across the 100 runs for various incident angles. The average is independent of the number of rays. For low divergence angles, the average transmission remains the same as that of the case where a single ray is traced; it is only at very high divergence angles where the transmission trend may begin to decrease, as will be discussed in Section 3.6.3.

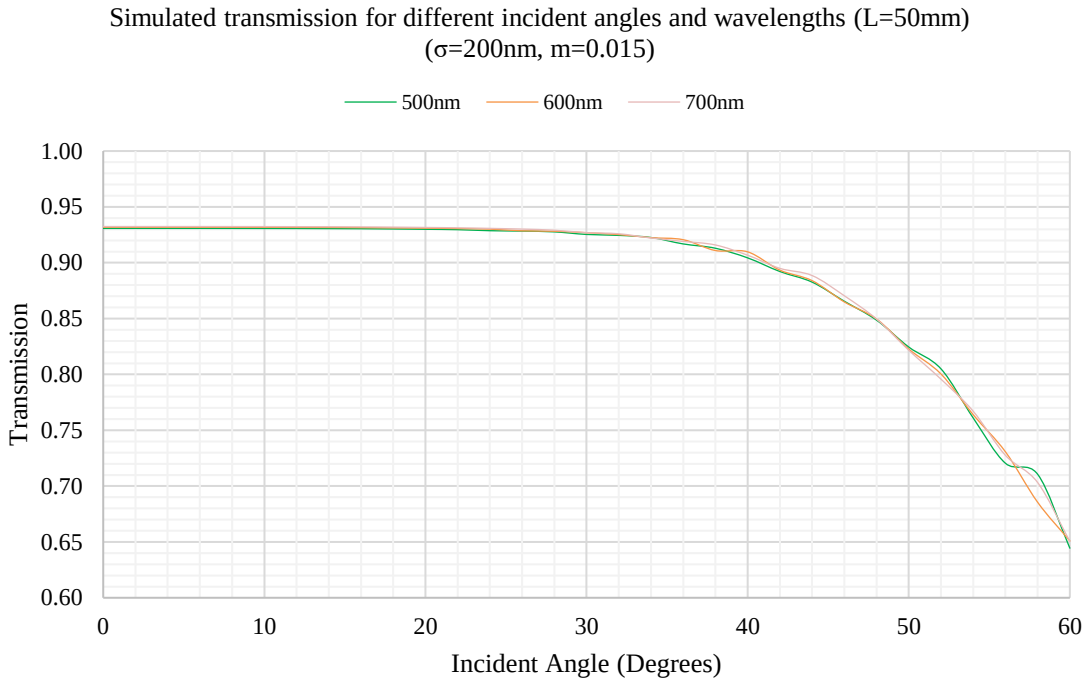

Figure 3.12 Simulated transmission as a function of incident angle and wavelength

Table 3.2 Power transmission standard deviation for 100 runs (σ=200nm, m=0.015, L=50mm)

Incident Angle (°)	Std 500nm	Std 600nm	Std 700nm
10	<0.01%	<0.01%	<0.01%
20	0.02%	0.02%	0.02%
30	0.42%	0.38%	0.54%
40	1.69%	1.25%	1.71%
50	4.12%	4.27%	4.12%
60	7.57%	6.40%	7.39%

3.6.2. RMS Height Versus RMS Slope

To also demonstrate the transmission characteristic as a function of the RMS height σ and slope m, Figure 3.13 shows transmission for various values of σ and m. From the figure, it is evident that the transmission characteristic depends on the RMS slope while the RMS height plays no role in determining the transmission. This can be visualized from a geometrical perspective; the RMS slope is related to the orientation of each local tangent plane of a rough surface while the magnitude of the reflected power, based on the geometric optics approach, is dependent on the incident angle and hence orientation of the local planes. A smaller RMS slope more closely resembles a perfectly smooth surface while a higher RMS slope increases the probability for any given ray to violate the condition for total internal reflection upon intercept at a tangent surface plane and hence lower the average reflected power from the rough side wall. The RMS height meanwhile only relates to the "scalability" of the surface profile.

Using this approach, we can characterize the performance of light pipes based on the RMS slope after polishing. The main challenge in maximizing the transmission is therefore to minimize the RMS slope by improving the fabrication process.

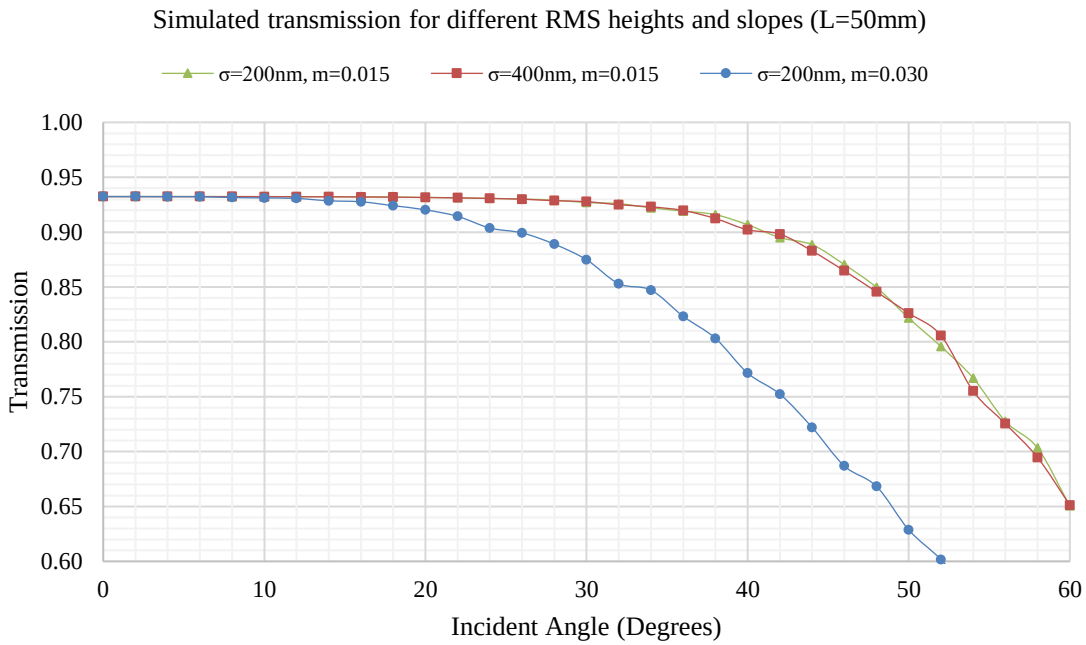

Figure 3.13 Simulated transmission as a function of roughness parameters

3.6.3. Beam Size And Divergence

Figure 3.14 shows the transmission as a function of beam radius r and divergence half angle θ. Here, r and radius of curvature at the input is changed to vary the value of θ. The RMS slope here is 0.015. A change in r or θ shows no significant change in the transmission at varying incident angles for lower values of θ and only starts to decrease for very high divergence angles. Since the geometric optics method is an approximation to more rigorous analytical approaches, this method may not accurately simulate the distribution of light scattered from the rough sidewalls. However, given the simulation, our method suggests that the geometric optics method may be sufficient for approximating

the power output of optical waveguides for low input beam divergence and surface scattering.

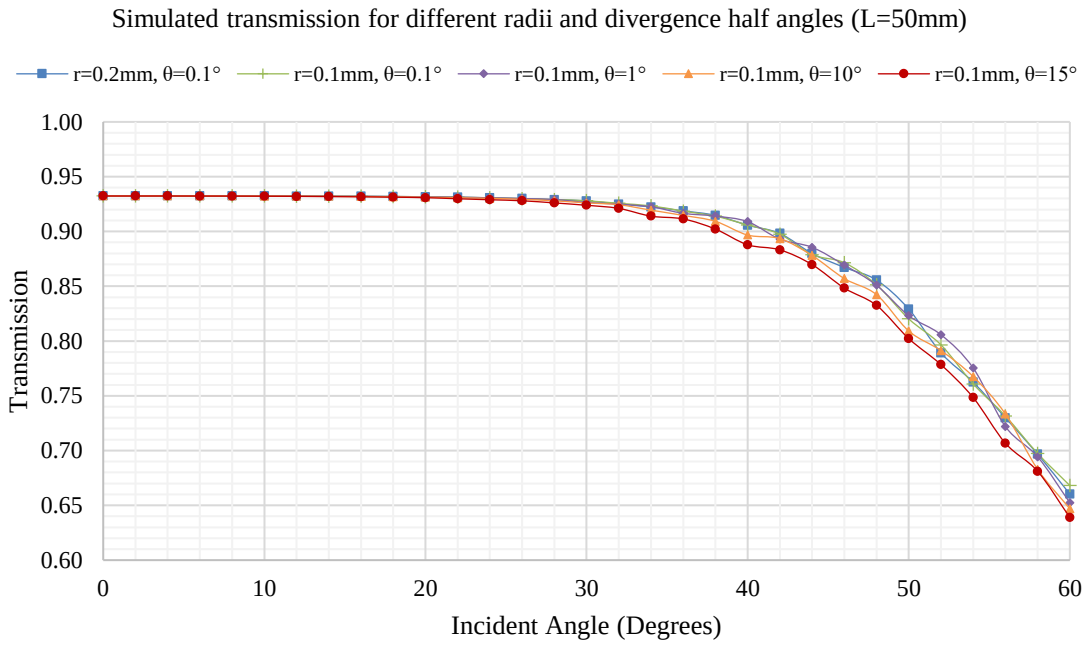

Figure 3.14 Simulated transmission for different input beam radii and divergence half angles

3.7. Assumptions And Considerations

3.7.1. Rough Surface Boundary

Currently, the transmission through the light pipe is determined purely by rays reflecting within the light pipe. However, employing the geometric optics approach, it is possible for a significant portion of the power to escape and re-enter the light pipe at a local area of a rough surface. Such a scenario is depicted in Figure 3.15.

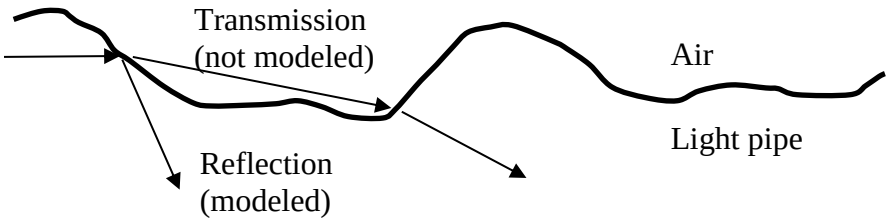

Figure 3.15 Illustration of ray escaping and re-entering light pipe

If a significant portion of the power escapes and re-enters the light pipe, the algorithm may be underestimating the output power. This can be more severe for very rough surfaces. Currently this is not modeled due to computational constraints. However, it is possible to approximate this, for example tracing the route with the highest transmission, as part of future development.

3.7.2. Polarization

The reflection of a surface is dependent on the polarization of the electric field, i.e. the orientation of the field with respect to the plane of incidence. Currently, in the model, all reflections and transmissions are assumed to have the effect corresponding to that of an unpolarized source. The reflection is calculated by averaging the s- and p-polarized reflectivity components. Although the optical source employed in this work is slightly polarized, due to the random orientation of the planes in the rough surface model all calculations are made assuming equal contribution of s- and p- polarization. However, as future development, one can incorporate polarization dependency into the ray tracing model.

4. OPTICAL SETUP

4.1. Measurement Overview

We wish to characterize the transmission of light through the polished light pipes of varying lengths, for different incident angles and wavelengths. We use a broadband source with a wavelength tunable band-pass filter mounted onto a translational stage, and a rotational stage to adjust the incident angle into the light pipe. The measurement setup for light passing through a light pipe is shown in Figure 4.1.

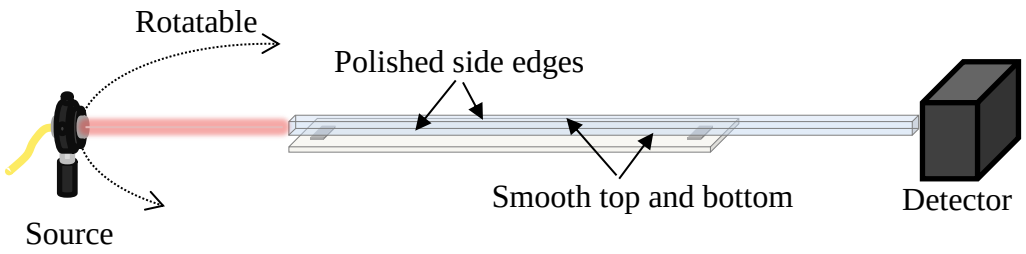

Figure 4.1 Schematic showing light pipe under test

Owing to the power fluctuation of our source laser, a separate reference photodetector, along with a beam splitter, was used to normalize our measurements. The transmission through the light pipe is then determined by the change in the ratio of the power measured between the S142C detector in the device under test stage and a reference detector, for the case where the light pipe is in place compared to the case where the light pipe is absent.

4.2. Experiment Schematic

Figure 4.2 shows a general block diagram of the setup for measuring optical transmission characteristics. Table 4.1 is a list of the equipment used in the setup. The color filter (VIS Filter) is attached to a sideways translational stage and the source into the light pipe (Source) is attached to a rotational stage.

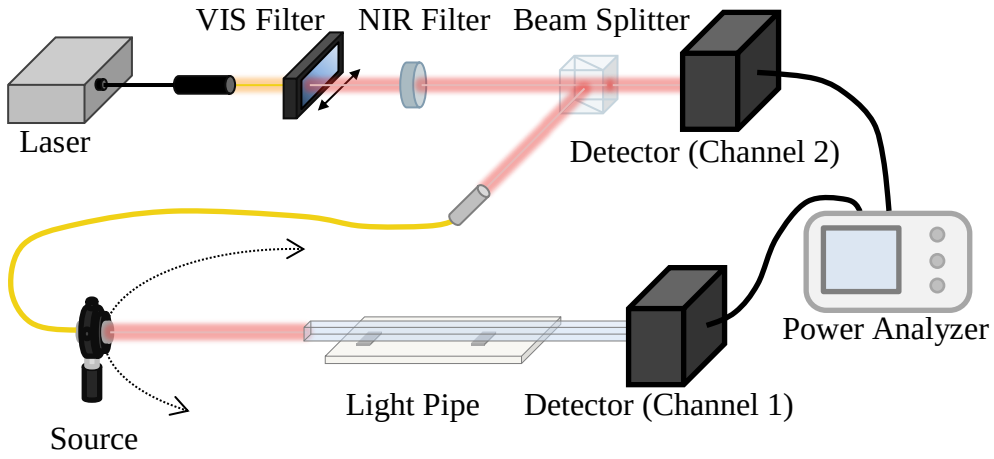

Figure 4.2 Block diagram of experimental setup

Table 4.1 Optical setup equipment list

Item	Model/Specifications
Laser	NKT Photonics SuperK COMPACT (broadband)
Visible Filter	Ocean Optics Band-pass Linear Variable Filter
NIR Filter	Thorlabs FM01, Thorlabs NENIR60B
Detector	Thorlabs S142C Integrating Sphere
Power Analyzer	Thorlabs PM320E Power Meter

The Photonics NKT SuperK COMPACT emits a broadband spectrum ranging from 400nm to 2400nm. An Ocean Optics visible band-pass filter mounted onto a translational stage is used to select the center wavelength, and an FM01 hot mirror and NENIR60B filter are both used to remove the unwanted near infrared wavelengths.

The power of the input beam after the filter is split via a beam splitter to a Thorlabs S142C integrating sphere and an optical fiber with appropriate collimators connected. At the output end of the fiber, the fiber and collimator are mounted onto an automated rotational stage to allow for the measurement of the power loss as a function of the incident angle into the light pipe

The output end of the light pipe is placed inside another Thorlabs S142C integrating sphere detector, and a Thorlabs PM320E power meter measures the power detected by both integrating spheres. The end facet of the light pipe passes through the aperture of the integrating sphere. The aperture is made smaller to minimize any potential measurements due to light leakage from the sides of the light pipe. The power meter is connected to a computer for data logging and processing.

4.3. Source Characteristics

4.3.1. Spectral Intensity

An Ocean Optics linear variable band-pass filter is used to tune the wavelength of the incident beam. The filter is mounted onto a Thorlabs MTS50-Z8 translational stage and controlled with the Thorlabs KDC101 motor controller. The visible spectrum at Channel 1 for various wavelength tuning adjustments are shown in Figure 4.3, measured using the Ocean Optics STS-VIS spectrometer.

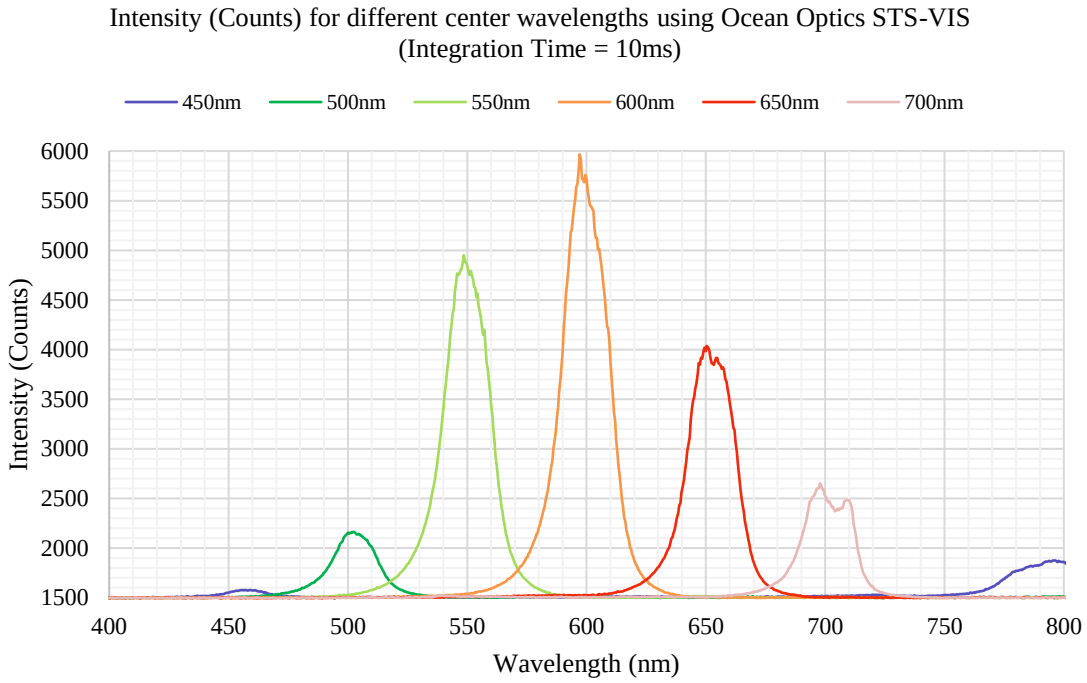

Figure 4.3 Visible spectrum for different center wavelengths due to visible band-pass filter tuning

4.3.2. Beam Divergence

The beam radius at the input to the light pipe and divergence half angle was estimated based on a few rough measurements at different distances from the source. Figure 4.4 shows the estimation of the beam radius at different distances along the optical axis. Based on the input facet being approximately 70mm away from the source, we estimate the beam radius at the input facet to be 0.22mm, with a divergence half angle approaching 0.17 degrees in the far region.

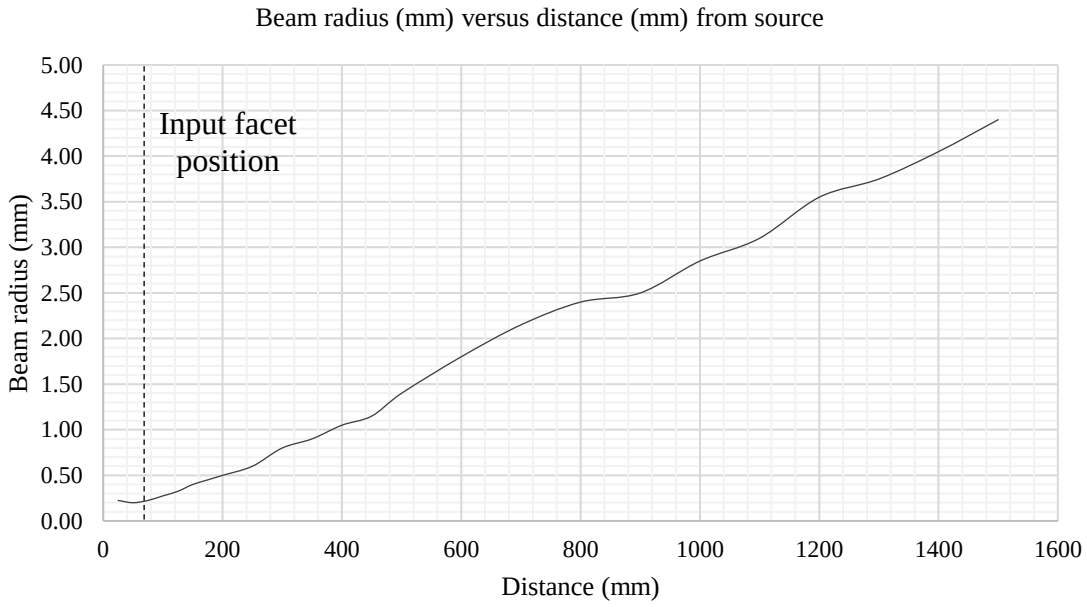

Figure 4.4 Beam radius versus distance from source at device under test stage

4.3.3. Considerations

Due to the periodic power fluctuation of the source, two detectors are required to accurately measure the power loss through the light pipe. The power output through the light pipe is determined by the power measured in Channels 1 and 2 of the Thorlabs PM320E. First, the ratio between Channels 1 and 2 is measured and calculated via Equation 4.1 without the light pipe in place.

$$\text{Reference Ratio} = \frac{\text{Channel 1 power (without light pipe)}}{\text{Channel 2 power}} \tag{4.1}$$

The ratio with the light pipe is measured and calculated using Equation 4.2.

$$\text{Current Ratio} = \frac{\text{Channel 1 power (with light pipe)}}{\text{Channel 2 power}} \tag{4.2}$$

The total output transmission of the light pipe sample is given by Equation 4.3.

$$\text{Transmission} = \frac{\text{Current Ratio}}{\text{Reference Ratio}} \tag{4.3}$$

Owing to the instability of the source, the power detected on both Channels 1 and 2 fluctuates, however the ratio remains constant and relatively stable given no change to any coupling conditions in the system. Thus, Equation 4.3 serves as an accurate measure of the proportion of power entering and exiting the light pipe.

4.4. Measurement Procedure

Below are the general steps to measure the light pipe transmission.

1. Adjust the wavelength by moving the translational stage. Also set the wavelength of Channels 1 and 2 on the power meter to this value.
2. Record the ratio between Channels 1 and 2 for a specified amount of time and average the data to obtain the average ratio. Repeat this for all wavelengths of interest. (Note: We achieve this using a Python script.)
3. Place the light pipe on a mounted fixture and align the light pipe with the incident beam such that (a) the light pipe is parallel to the incident beam, (b) the center of the beam hits the center of the input facet of the light pipe for all incident angles of interest, and (c) the side walls of the light pipe are either parallel or perpendicular to the plane in which the incident beam rotates.
4. Set the wavelength as outlined in Step 1 to a value of interest and measure the ratio of Channels 1 and 2 as a function of the incident angle to the light pipe. Repeat this step for all wavelengths of interest.

5. Repeat step 1 to measure any changes in the average ratios after the light pipe transmission is measured. Assume a linear change to the average ratio measured in Step 1 and Step 4 and use this to calculate the transmission for each incident angle and wavelength by using Equation 4.3. (Note: We observe this change to be usually less than 1%.)

The Thorlabs PM320E and automation stages are controlled on a computer using a Python script. The Thorlabs PM320E power meter is continuously queried during the measurement phase. The rotational stage is slowly adjusted and the power for Channels 1 and 2 for each angle is measured for a specified time. Another script is used to control the translational stage of the Ocean Optics filter and hence the center wavelength of the incident beam. All data is exported to a .csv file.

4.5. Experimental Sources Of Error

Currently the detector used in the experiment is the Thorlabs S142C integrating sphere. The detector has an angular dependence for its power detection at higher incident angles into the detector. This will result in an inaccurate measured transmission particularly for incident angles of 40 degrees and over into the light pipes. Appendix A shows the measured data on the angular dependence of the detector. We estimate the discrepancy between the measured results and true value at incident angles below 40 degrees to be insignificant (see Appendix A).

5. RESULTS AND EVALUATION

5.1. Surface Profile Statistical Estimation

5.1.1. Height And Slope Variation Measurement

Many images of a 40mm test sample were taken with relatively equal spacing for each image across the length of the light pipe, as depicted in Figure 5.1. From this data, we compute the RMS height and slope for each image and then average the results to obtain a single RMS height and slope estimate. Since we employ the same fabrication process with the same CO_2 laser power for other light pipes, we assume the average RMS height and slope is roughly the same for each sample. It should be noted that, for this specific sample, approximately 14% of the total area was imaged. Table 5.1 shows statistical data of the RMS height and slope variations for the images taken. The RMS slope values shown pertain to the magnitude where the surface deviation is assumed to be isotropic in nature. Based on our images taken, the average RMS height and slope is approximately 222nm and 0.015 respectively, with slightly lower median values.

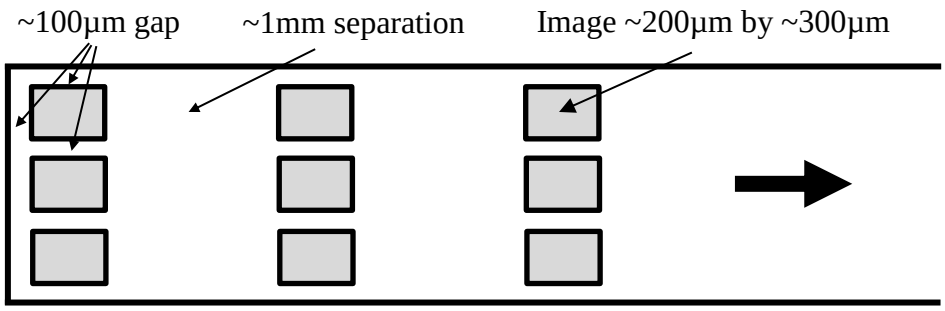

Figure 5.1 Polished surface sampling image separation

Table 5.1 Statistical quantities on RMS height and slope for 40mm test sample

Statistical Measure	RMS Height (nm)	RMS Slope
Mean	221.9	0.0147
Max	1508.3	0.0828
Upper Quartile	285.3	0.0183
Median	170.9	0.0117
Lower Quartile	90.6	0.0069
Min	36.3	0.0027

Figure 5.2 and Figure 5.3 also show the variation in the average RMS height and RMS slope respectively across the length of the test sample for both polished sides. For each displacement value shown, the RMS height and slope are averaged over the images taken for the position with respect to the length of the light pipe. We acknowledge an imperfect fabrication process may result in variations in the RMS height and slope across the sample, low frequency deviations ("waviness") and potential outliers. Ideally, the variation for all local images taken across the light pipe should be kept to a minimum for better surface uniformity and more accurate modeling of the surface profile. Thus, one future aim is to minimize the variation for the aforementioned statistical quantities by better control of the pre-polishing step or better automated control of the CO_2 laser intensity. Currently potential occurrences of surface ablation as functions of local temperature and CO_2 laser exposure time have not been investigated.

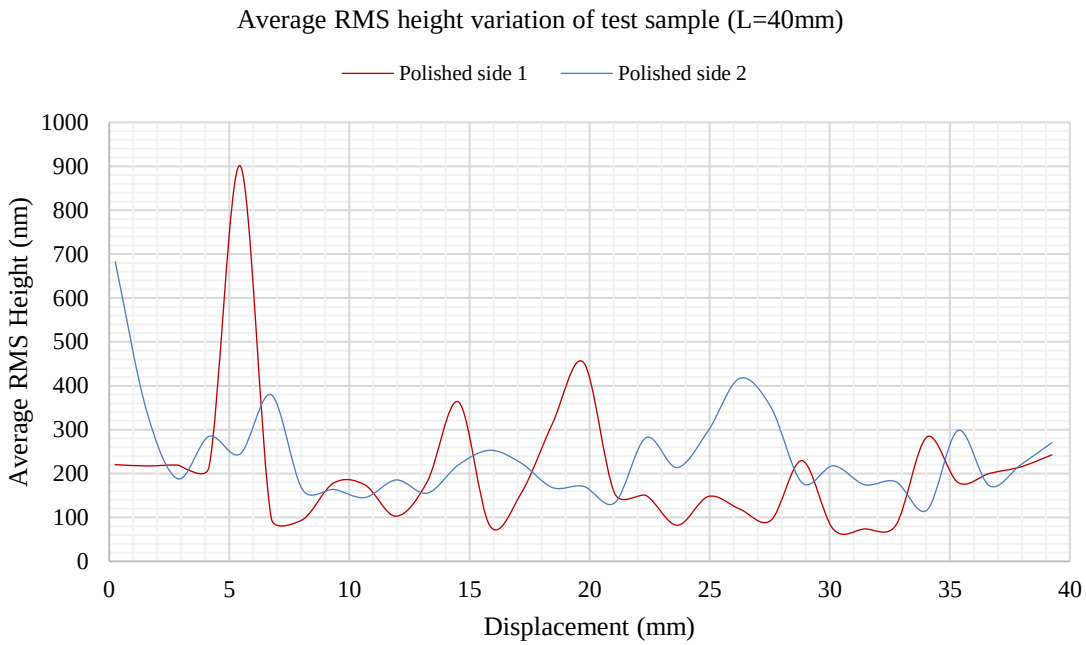

Figure 5.2 Average RMS height variation across length of 40mm test sample

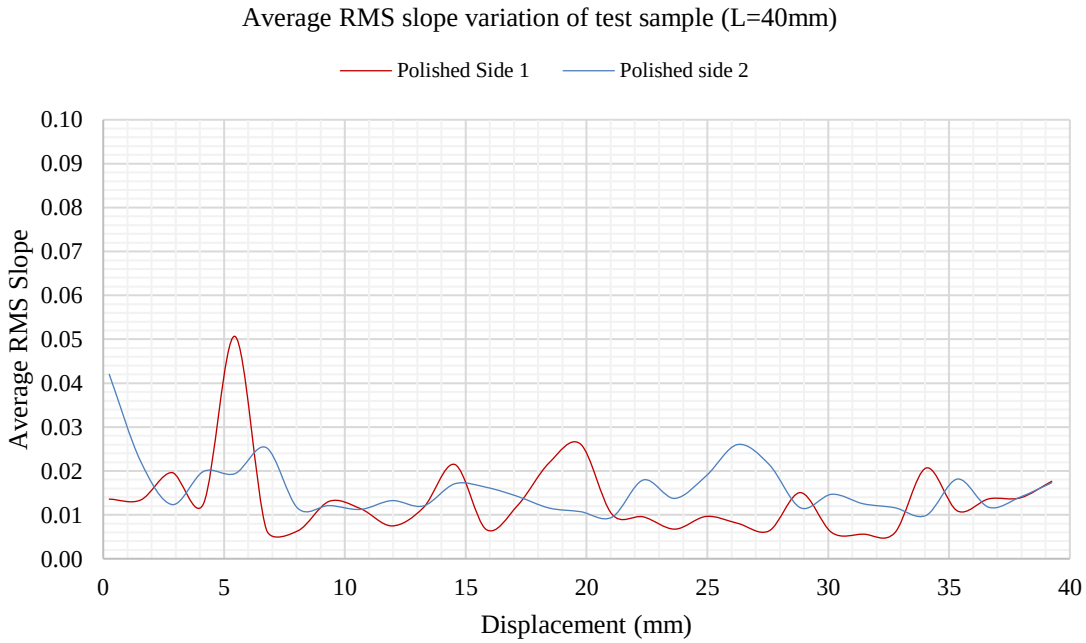

Figure 5.3 Average RMS slope variation across length of 40mm test sample

5.1.2. Generated Surface Profile Comparison

The images taken using the profilometer show varying low spatial frequency height deviations for any given localized area. Also, the variation in the RMS height and slope is significant compared to the simulated surface profiles. In contrast if we assumed a correlated Gaussian surface profile, we see in general more uniform variation with higher spatial frequencies. A comparison is shown in Figure 5.4. Images such as the example on the bottom left are common in measurement, in contrast to the higher frequency isotropic nature of the simulated surfaces.

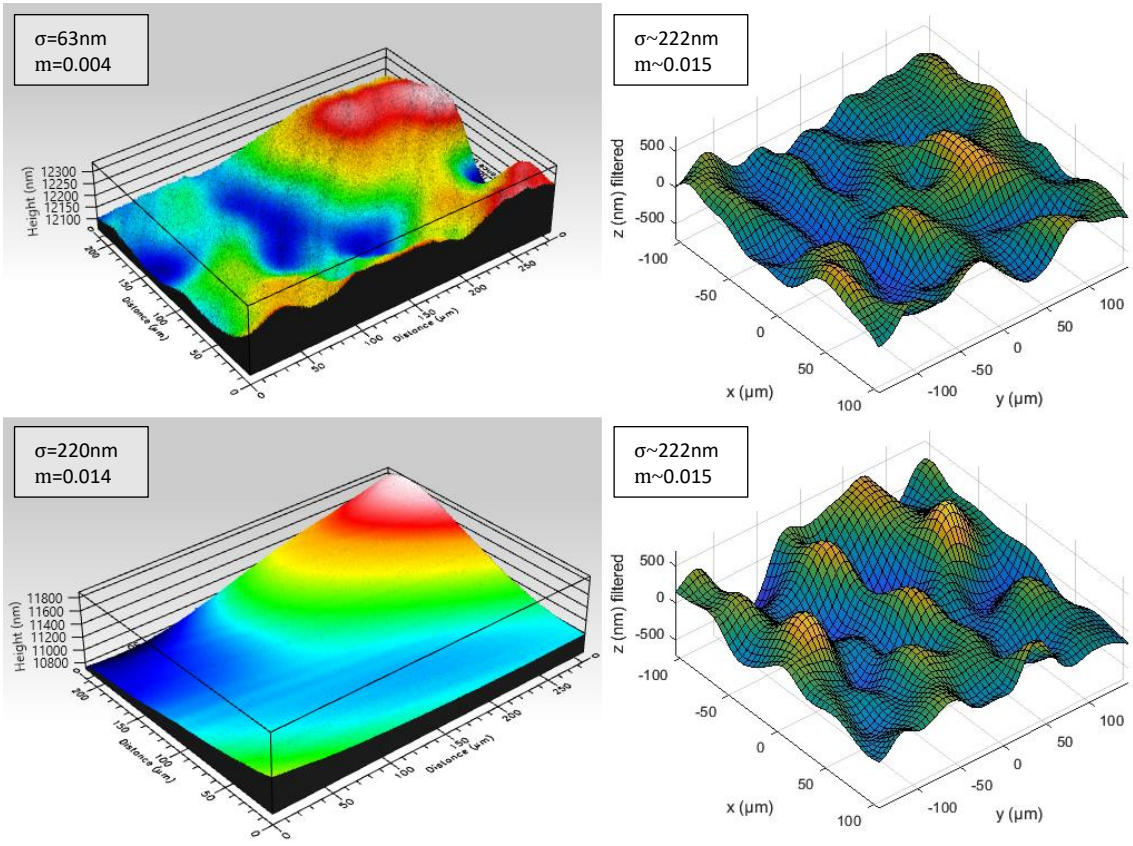

Figure 5.4 Examples of measured versus simulated surfaces for an average RMS height σ~222nm and slope m~0.015

For the images taken, the distribution of RMS height and slopes is also compared to the randomly generated case using the same sample size, as shown in Figure 5.5.

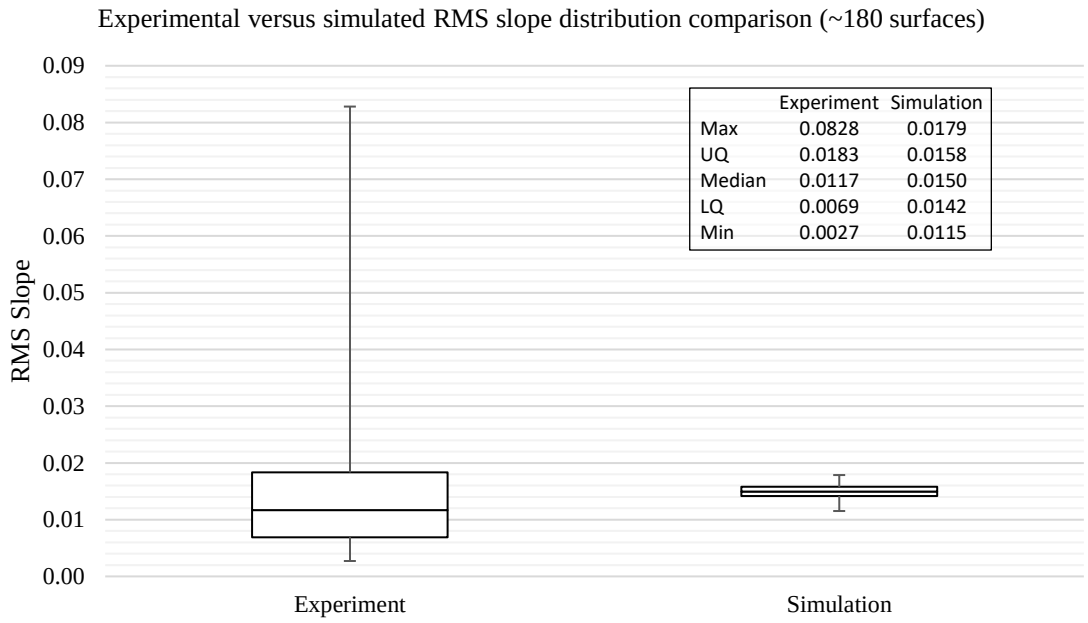

Figure 5.5 RMS slope distribution comparison between experiment and simulation for local surface profiles

The measured RMS slopes for small local areas of the polished surface have a much larger deviation compared to the generated surfaces. Moreover, for the experimental case, the deviation contains a few outliers with high RMS slope values. In contrast, the simulation shows, for a local surface profile, very little deviation about the mean RMS slope of 0.015 compared to the measured values, and the distribution is symmetrical. Thus, we model the surface with the knowledge that there will be an imperfect fit between the generated surface and the true surface for any given sample.

5.2. Light Pipe Measurement And Simulation Comparison

We recently tested three polished light pipes, with lengths 30mm, 50mm and 70mm. BK7 cover slips were attached to the 30mm and 70mm samples to minimize diffraction occurring at the input and output facets. Cover slips were not attached to the 50mm sample due to the directional output beam for the 50mm sample observed at normal incidence. Appendix B shows data on the measured transmission for the samples for different wavelengths and angles of incidence, and for different directions.

The measurements are compared against the simulation results of 100 runs using different RMS slope values. Using 0.015 as the experimentally predicted RMS slope, we compare our prediction to the simulated trend. It should be noted that all samples show that at a wavelength of 500nm the transmission is lower for most incident angles. Currently we suspect poor quality support mounts with some small wavelength dependence may contribute to this observation (see Appendix C).

In addition, we observe a unique angular pattern at the output of our light pipes in the form of a ring (see Appendix D). While describing such a pattern is outside the scope of this thesis, such a pattern is within the realms of future investigation.

5.2.1. 30mm

The transmission for the 30mm sample was tested in 4 different orientations, labeled as (1) to (4) shown in Figure 5.6. Figure 5.7 shows the transmission averaged from all 4 orientations for the wavelengths 500nm, 600nm and 700nm in comparison with the simulated transmission for different RMS slopes. At 4 degrees, we see an anomaly for one direction (see Appendix B) and may be due to a combination of beam positioning and

surface structure resulting in a large divergence at the output causing the detector to overestimate the power. The angular dependence of the detector also results in inaccuracies such as those beyond 45 degrees (see Appendix A and Appendix B).

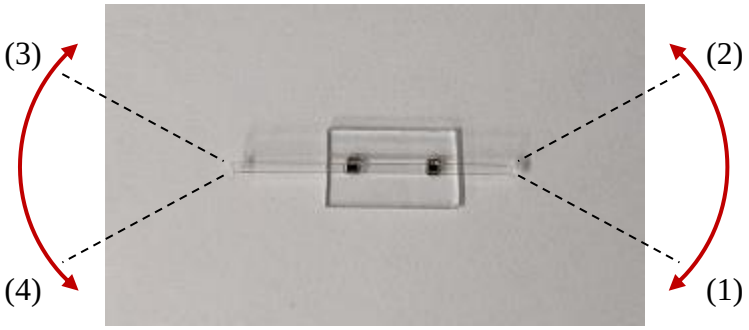

Figure 5.6 30mm light pipe showing 4 directions measured

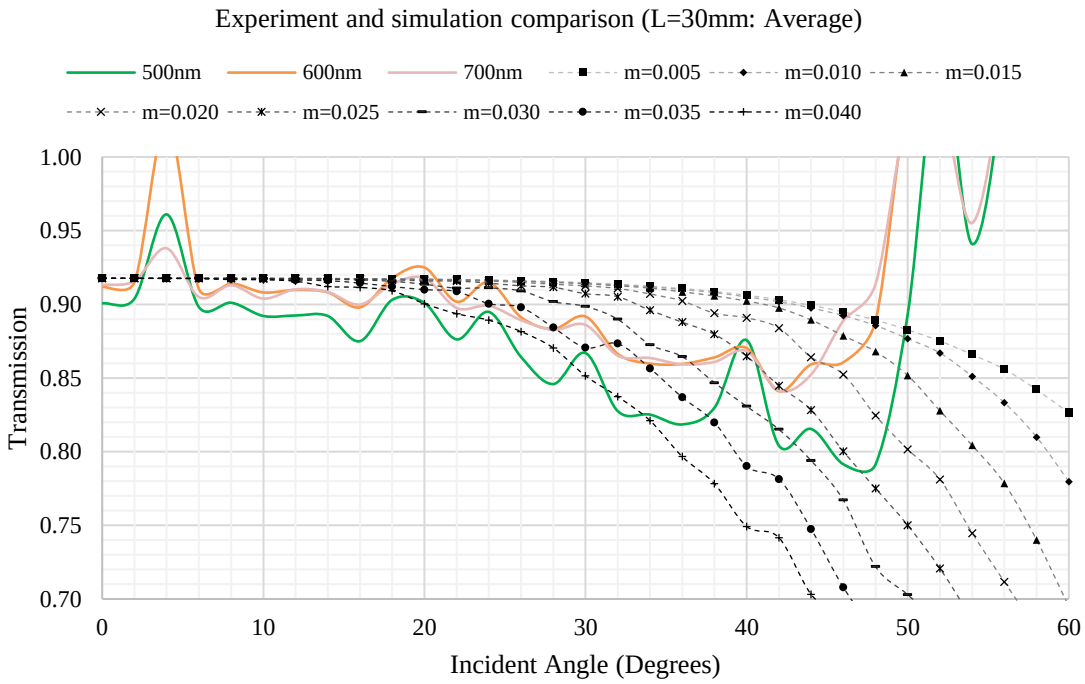

Figure 5.7 Measured transmission for 1mm x 1mm x 30mm light pipe sample (500nm-700nm) compared to different RMS slope (*m*) simulations

Without taking other potential loss factors into account, at a first glance the simulation predicts the RMS slope of the sample to be in the range 0.03 to 0.04 for the wavelengths 600nm to 700nm and higher for 500nm. However, based on our current fabrication process, we predict an RMS slope of approximately 0.015. Moreover, we observe a relatively linear decrease in transmission and higher than expected losses at lower incident angles, whereas the simulation predicts a relatively high transmission of 90% for an RMS slope of 0.015 for incident angles up to 40 degrees. At higher angles of incidence, the simulation appears to underestimate the transmission for an RMS slope of 0.03 or higher.

5.2.2. 50mm

The transmission for the 50mm sample was measured in 2 different orientations due to the mounting position, labeled as (1) and (2) shown in Figure 5.8. The RMS slope for the 50mm sample according to the simulation at a first glance falls in the range 0.03 to 0.035 for incident angles up to approximately 35 degrees, however this is above our estimate of 0.015 or below. Like the 30mm sample, the 50mm sample shows a relatively linear decrease in transmission with incident angle, and higher than expected losses at lower incident angles. The simulation also predicts a lower than measured transmission for most incident angles approaching 40 degrees and over.

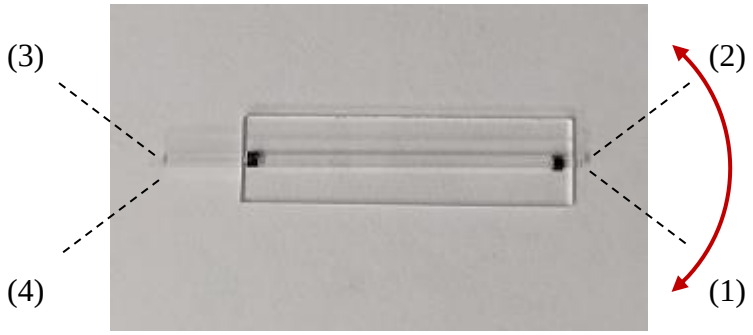

Figure 5.8 50mm light pipe showing 2 directions measured

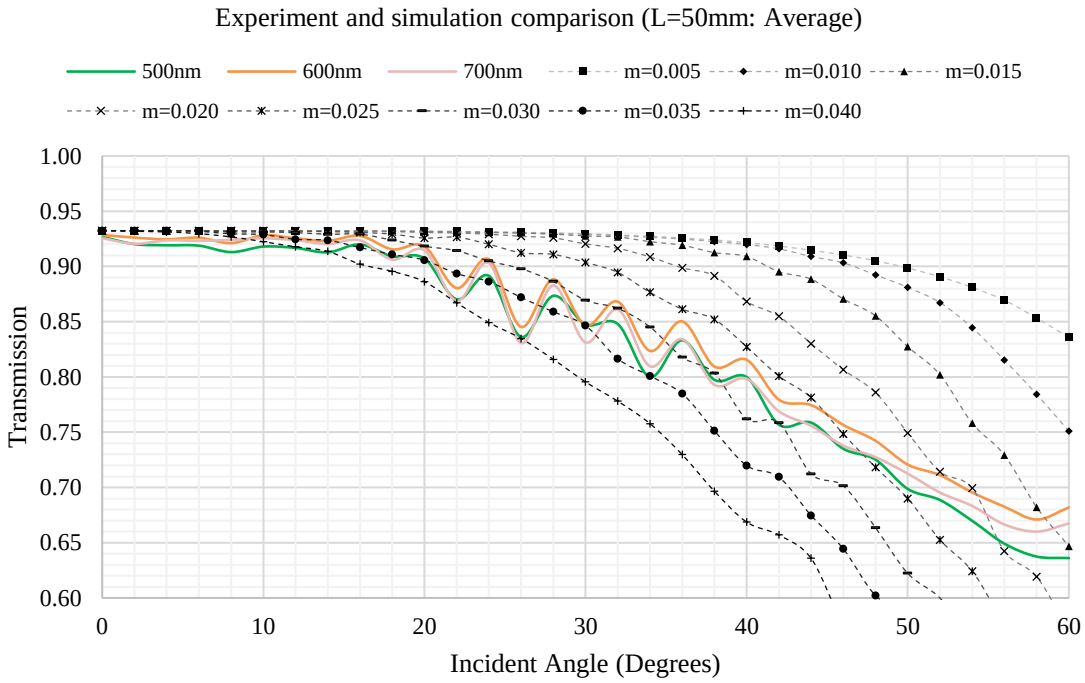

Figure 5.9 Measured transmission for 1mm x 1mm x 50mm light pipe sample (500nm-700nm) compared to different RMS slope (*m*) simulations

5.2.3. 70mm

The transmission for the 70mm sample was measured in 4 different orientations labeled as (1) to (4) shown in Figure 5.10. Figure 5.11 shows the average measured transmission compared to the simulated transmission for different RMS slope values. The simulation depicts an RMS slope in the range 0.03 to 0.035 for incident angles up to approximately 35 degrees and, like the previous samples, this is above our estimate of 0.015 or below. The samples show relatively linear and lower than expected transmission at lower incident angles. It should be noted that the measured transmission for (1) and (2) are slightly higher than the measured transmission for (3) and (4), however all four sides are averaged (see Appendix B). This issue is addressed later in this section.

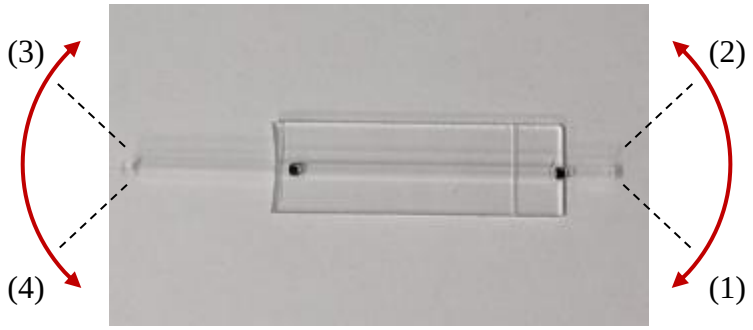

Figure 5.10 70mm light pipe showing 4 directions measured

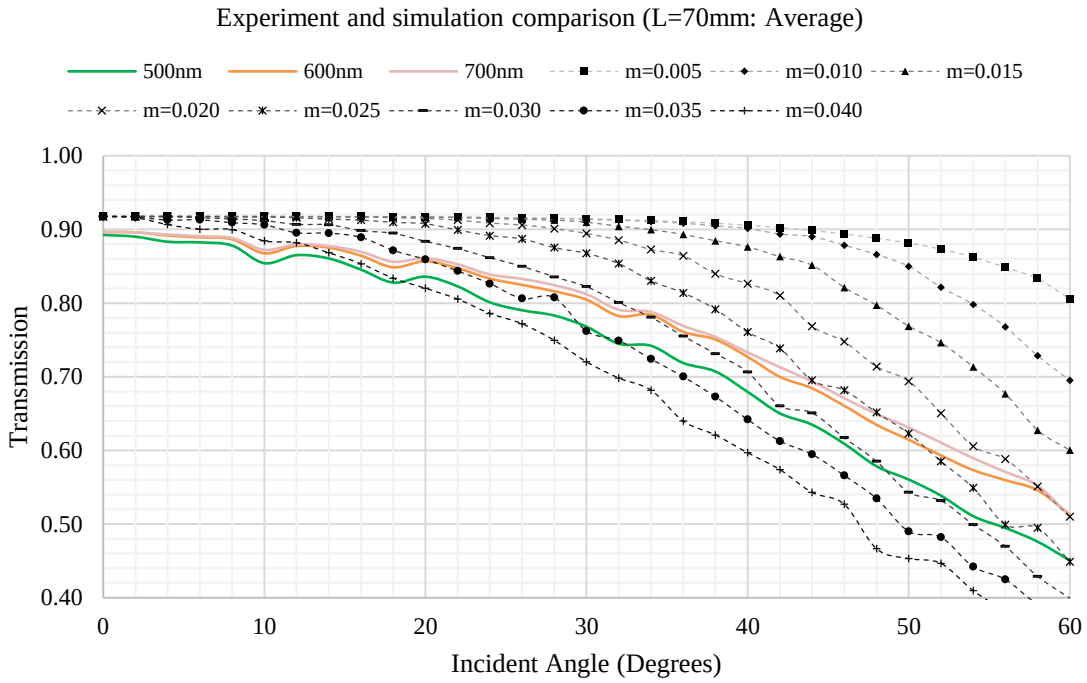

Figure 5.11 Measured transmission for 1mm x 1mm x 70mm light pipe sample (500nm-700nm) compared to different RMS slope (*m*) simulations

5.3. Potential Loss Contributions

5.3.1. Sidewall Intersection Loss

Although surface defects after laser polishing are minimal for our samples, some finite losses that do not depend on Fresnel's equations at the polished sidewalls may result in a lower transmission. For example, one explanation is that subsurface damage can occur during the pre-polishing in which case the damage may not be apparent under a microscope. Since this can be random in nature, we assume some constant loss at the glass-air boundary irrespective of wavelength and angle of incidence in the simulation. Figure

5.12 shows the transmission for a finite power loss (SL) of 0.5% and 1% every time a ray hits the boundary of a polished surface compared to the case with no side loss.

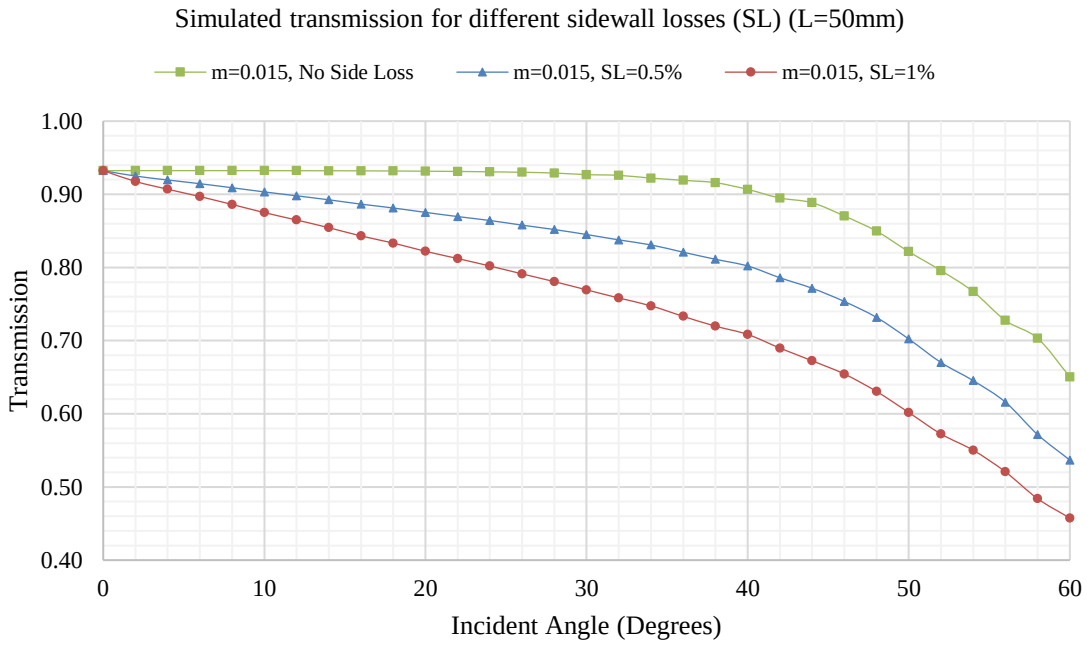

Figure 5.12 Effect of constant sidewall loss on transmission

As shown, the transmission shows a relatively linear decrease at the lower incident angles if a constant loss at the boundary is assumed. Although such effects have not been comprehensively studied in this work, subsurface detects may occur during fabrication, for example by etching. Here, we resort to a qualitative discussion of how such unwanted formations may impact our measurement results. Figure 5.13 shows an incident ray and the reflected and scattered components from the damaged subsurface layer. As light approaches the polished surface boundary, subsurface defects can cause light to scatter

resulting in more scattering directions that violate the total internal reflection condition. This will result in a higher loss at the boundary and a wider spread of reflected power.

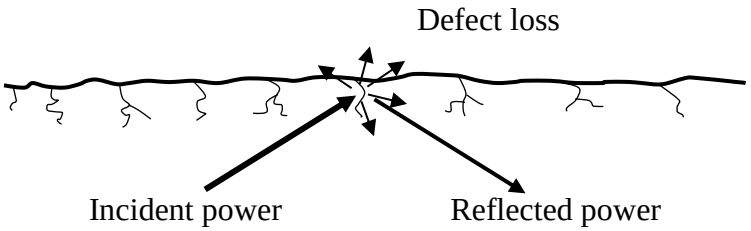

Figure 5.13 Illustration of impact of subsurface defect layer on transmission

Such effects may also result in more light hitting the support mounts to give rise to additional losses, which may in turn cause a larger discrepancy between the transmission measured at different wavelengths. See Appendix C for the measured reflectivity of the support mounts at different wavelengths.

While subsurface defects may explain the loss trend observed in the measurements, we do not consider this the only explanation. Rather, in general some imperfection on the sidewalls may result in a linear loss trend.

5.3.2. Absorption Loss

Refer to Section 1 for a brief discussion of the mechanism of absorption in materials. The intensity I is related to the attenuation coefficient α (cm^{-1}) and the distance l for light traveled in a material via the proportionality

$$I \propto \exp(-\alpha l) \tag{5.1}$$

For fused silica, the attenuation coefficient is usually negligible. However, as a demonstration, we model the proportional loss by computing the path traveled, for a certain value of α. This is shown in Figure 5.14.

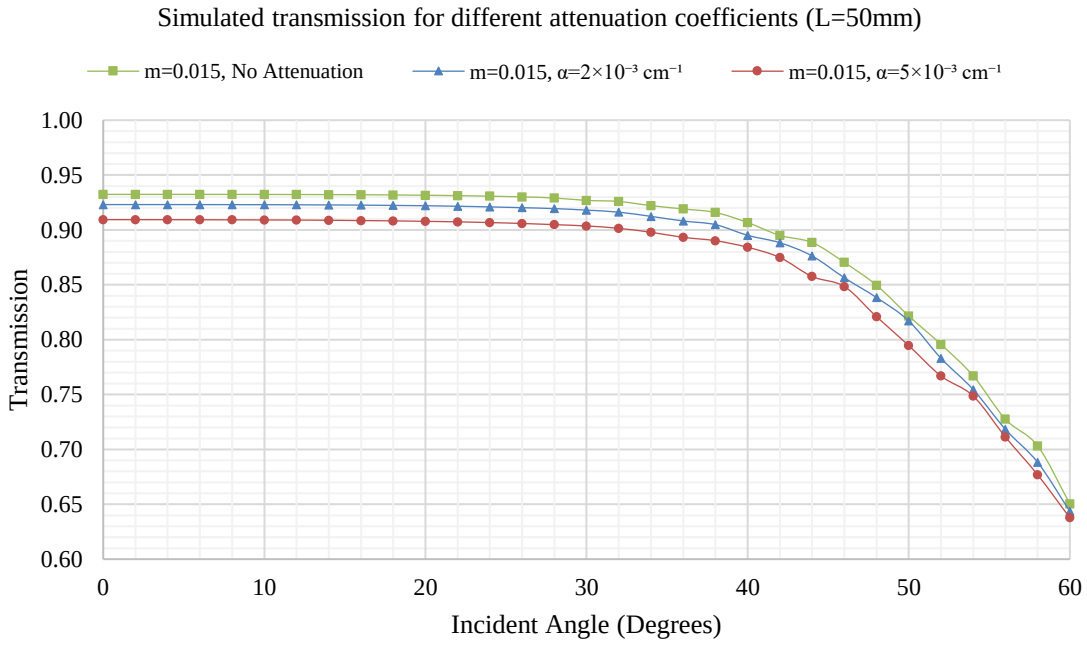

Figure 5.14 Effect of attenuation coefficient on transmission

As observed, imposing a non-negligible value of α in the simulation only shifts the entire transmission curve due to the nonlinear exponential factor relating intensity to the path traveled. Thus, this is not expected to result in a relatively linear decrease and higher than expected losses at lower incident angles.

5.3.3. Irregular Surface Structure

If the CO_2 laser polishing intensity fluctuates, some areas may be subject to a finite degree of ablation. The pre-polishing fabrication step, not detailed in this work, may also introduce irregularities in the surface structure such that the polishing process cannot compensate for. As a simple case, we model the effect of superimposing, on top of a randomly generated rough surface profile, a non-parallel polished structure and a single cosine reduction for the polished sides as illustrated in Figure 5.15.

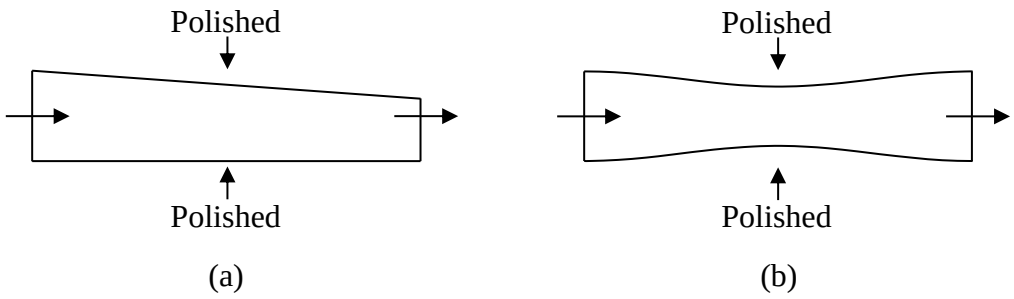

Figure 5.15 Simulated irregular surface examples; (a) non-parallel surface, (b) low frequency cosine deviation

For the non-parallel case, the output side of the light pipe was reduced by 100μm in width. For the cosine case, a cosine with a 25μm amplitude was applied on the polished sidewalls to reduce the width. Figure 5.16 shows the effect of such reductions in the simulation.

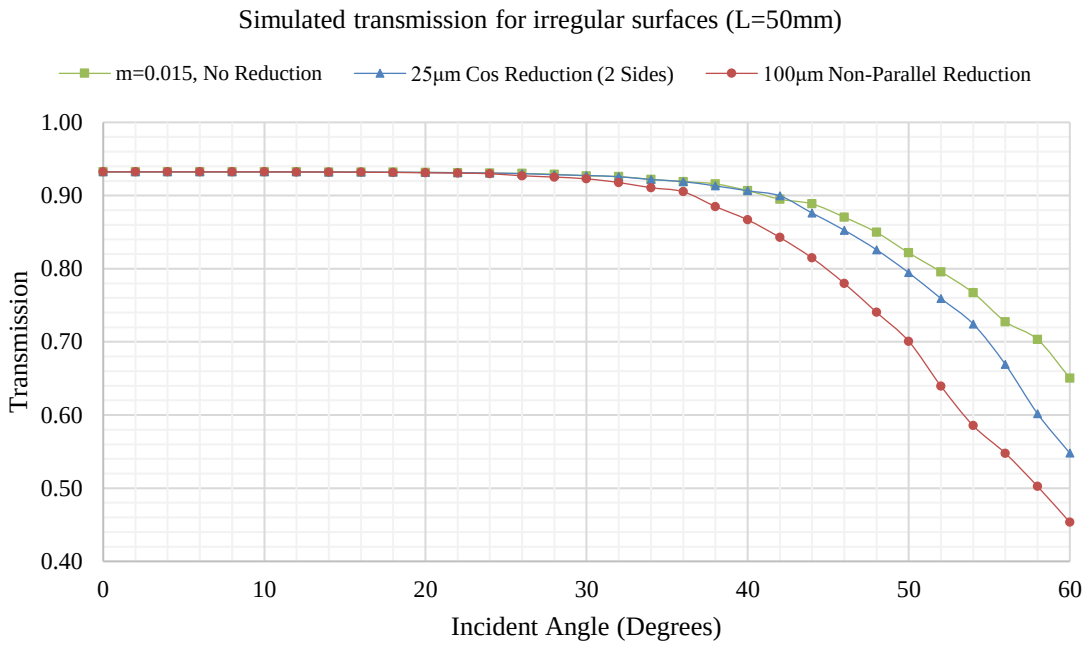

Figure 5.16 Effect of irregular polished sidewalls on transmission

Clearly, a width reduction results in higher losses primarily at the higher incident angles. This is expected due to an increase in the effective slope of the sidewall and a width reduction leading to more internal reflections on average. The power loss from the sidewalls however is a function of the incident angle with respect to each local plane of the rough surface and thus is the likely reason for minimal losses at lower angles of incidence into the light pipe. Without an incident angle-independent constant loss mechanism, the geometric optics method shows non-linear behavior in the overall transmission trend.

To extend this concept, small aberrations in the shape of the surface from the simulated isotropic case, such as low spatial frequency deviations, likely cannot account

for high losses at lower incident angles into the light pipe and a linear reduction in transmission. Although this will impact the RMS slope, the power loss will be governed by angle dependent internal reflection.

5.3.4. Coverslips

The BK7 glass coverslips also contribute to a small loss through the light pipe. This is already modeled in the simulation for the light pipes. Fresnel's equation for transmission is used to model the behavior of a BK7 coverslip with negligible thickness that acts as an interface between air and fused silica glass. Figure 5.17 shows the impact of the BK7 coverslips attached to both input and output facets on the transmission.

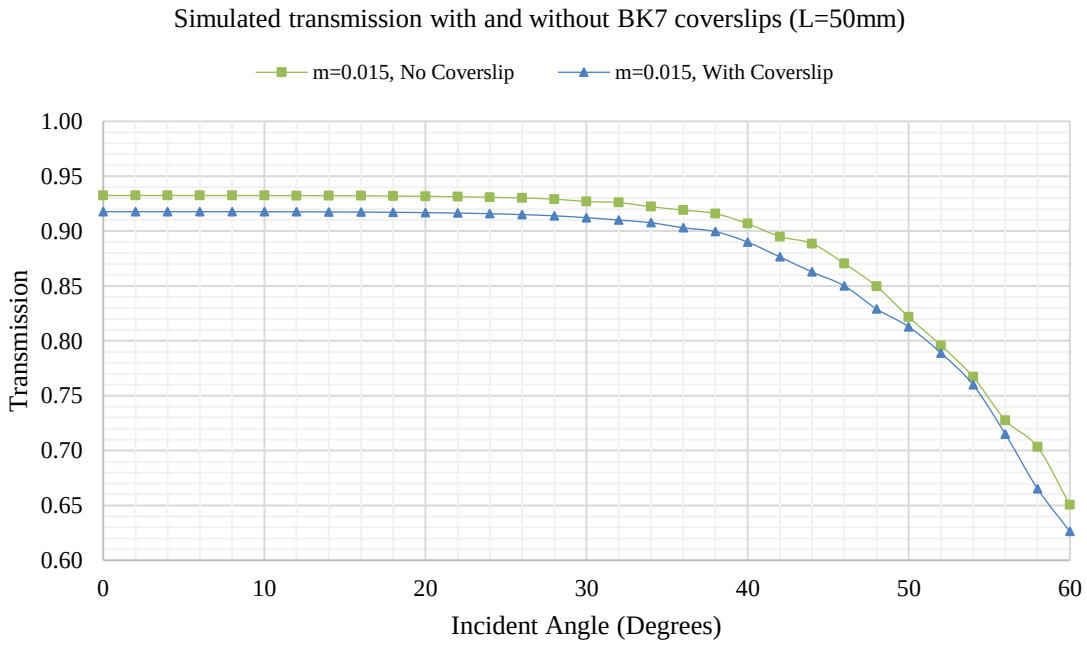

Figure 5.17 Effect of coverslips on transmission

Due to a small difference in the refractive index between BK7 and fused silica in the visible region, a small constant loss for every incident angle is expected. However, this will not result in a linear loss trend such as that shown in the experimental data.

5.3.5. Support Mounts

Currently support mounts, consisting of a silicon dioxide layer on top of a silver platform, are modeled as a constant loss for light reflecting from the areas covered by the mounts (see Appendix C). The mounts are modeled at their respective regions for each light pipe. To compare different values of losses, Figure 5.18 shows the effect of a reflectivity value of 0.5 and 0 as a worst case scenario on the 50mm sample.

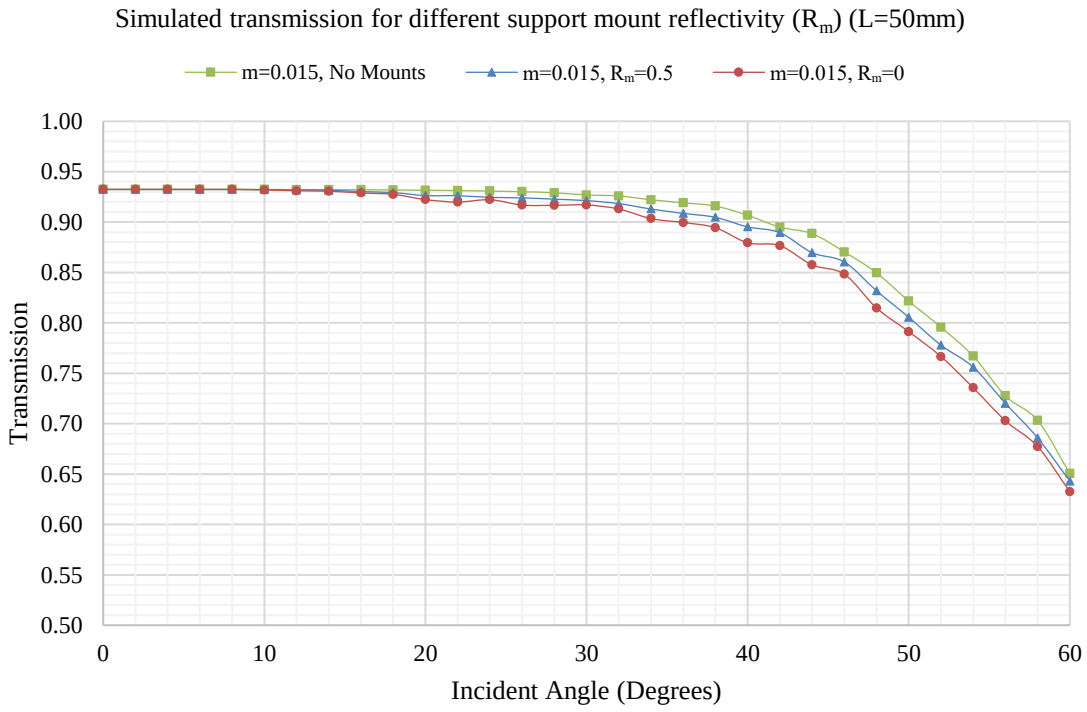

Figure 5.18 Effect of support mount with constant loss on transmission

This constant loss model can be said to have similar effect as the constant sidewall loss model where the area affected is restricted. However, from a marginal reduction in transmission for the worse case reflectivity values simulated, one should not expect this to dominate the low transmission at low incident angles into the light pipe and result in the linearity in the loss.

One pressing question that can be asked is whether divergence angle in conjunction with a constant loss platform within a local area can result in a decrease in transmission. Figure 5.19 shows the effect of divergence angle of the input beam with the support mounts modeled on the transmission.

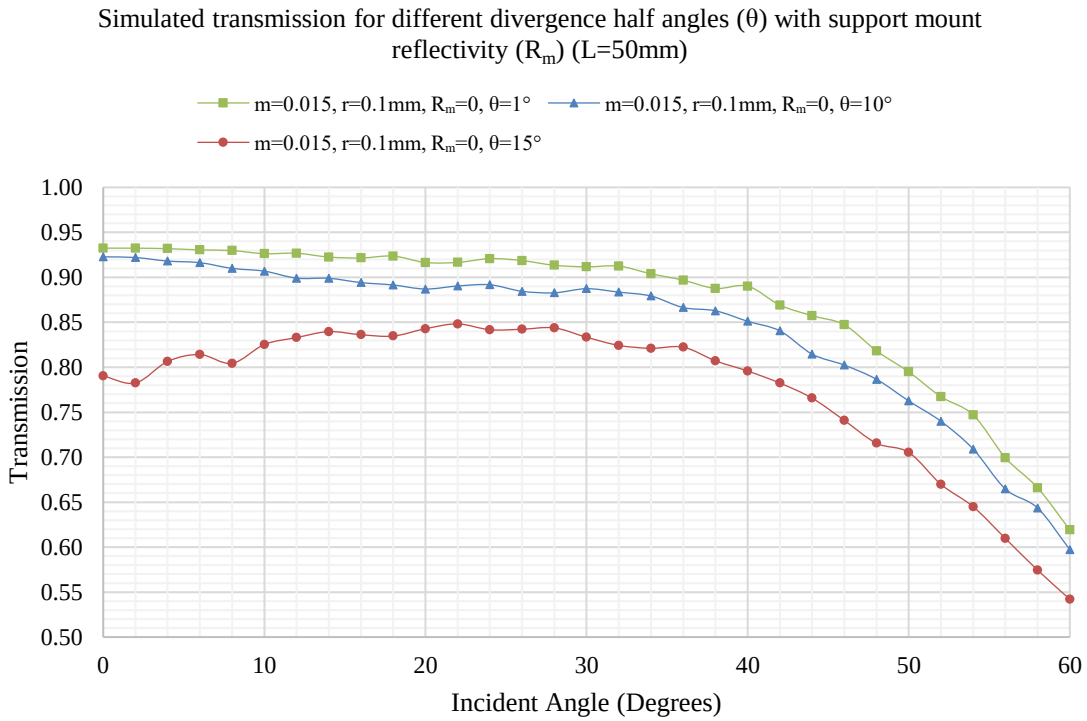

Figure 5.19 Effect of divergence on transmission with support mount modeled

Unlike Figure 3.14, we see a substantial change in transmission if a constant loss is also modeled for lower values of θ. A higher than expected scattering effect for power distribution may result in a higher loss such as that seen for $\theta = 10^{o}$ at low incident angles, although not as linear as a constant sidewall loss. Rigorous wave theory methods may be better at incorporating the scattering effect from a rough surface; however, the geometric optics approach may be generally sufficient to model power loss through waveguides when a constant loss is not taken into account.

Support mount placement can also affect the overall transmission. For example, Figure 5.20 shows the transmission of a 50mm light pipe with support mounts located at 2.2mm and 36.6mm from one end of the light pipe, each covering 1.4mm. The support mounts are assumed to have the same reflectivity. At very low divergence angles, the transmission of the sample may not change significantly, however scattering effects, for example from subsurface defects on the polished sidewalls, or a large divergence may lead to a noticeable difference in transmission for different input directions. In general, any asymmetry such as different reflectivity values for each support mount will tend to result in differences in transmission for each input direction. This may also explain higher losses for one direction for the 70mm sample (see Appendix B) if there are large internal scattering effects. For the 30mm sample this is not as obvious, possibly due to the specific geometry of the sample and a smaller length.

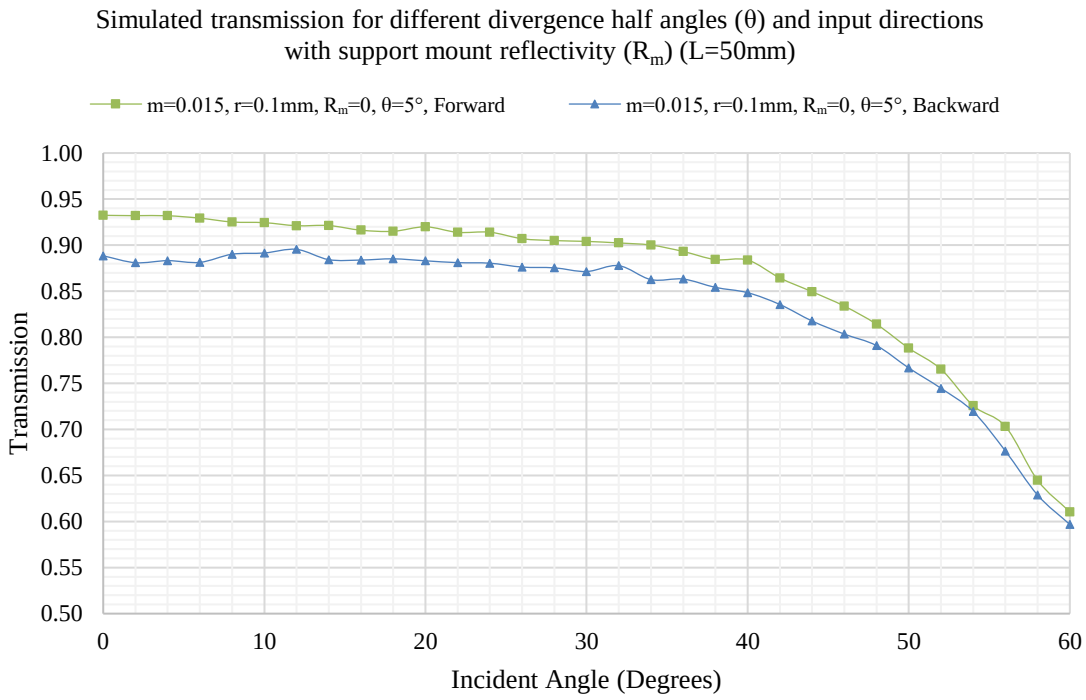

Figure 5.20 Effect of input directionality with support mount modeled (non-symmetrical mount position)

5.3.6. Polarization

Reflectivity from a surface is dependent on the polarization of the source, i.e. the orientation of the electric field with respect to the direction of the ray. An electric field that is perpendicular to the plane of incidence is said to be s-polarized while parallel to the plane of incidence is said to be p-polarized. The plane of incidence is normal to the interface plane between two mediums. The reflectivity for the s- and -polarization components are described in Section 3.4.2. Figure 5.21 shows the reflectivity for each polarization for light going from the fused silica medium to air, with a refractive index η of approximately 1.46 for fused silica and 1 for air.

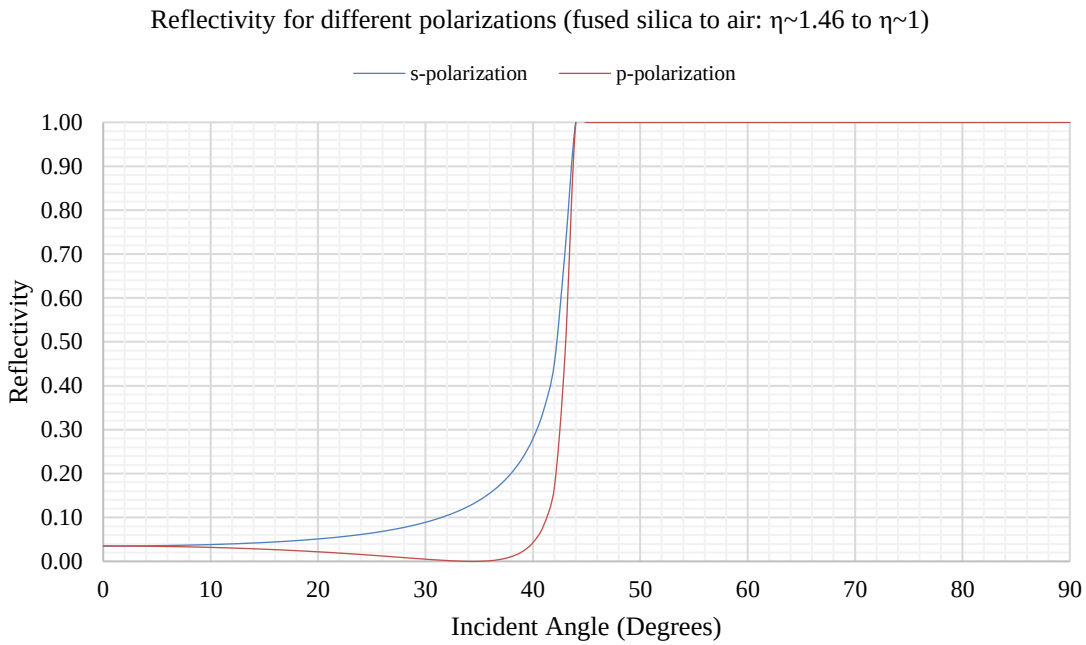

Figure 5.21 Reflectivity dependence on polarization (fused silica to air)

As the planes in the rough surfaces are randomly orientated, the reflectivity values from both polarizations are averaged, i.e. we neglect polarization dependency and assume the effect of an unpolarized source. The output power may differ depending on the polarization, and one may find on average a lower transmission for sources that are relatively p-polarized with respect to most planes of the rough surface.

To determine whether this likely has a profound impact on the results, Figure 5.22 shows the transmission averaged over 100 runs for the case where the reflectivity on the rough surface, and transmission at the output, is minimized due to polarization.

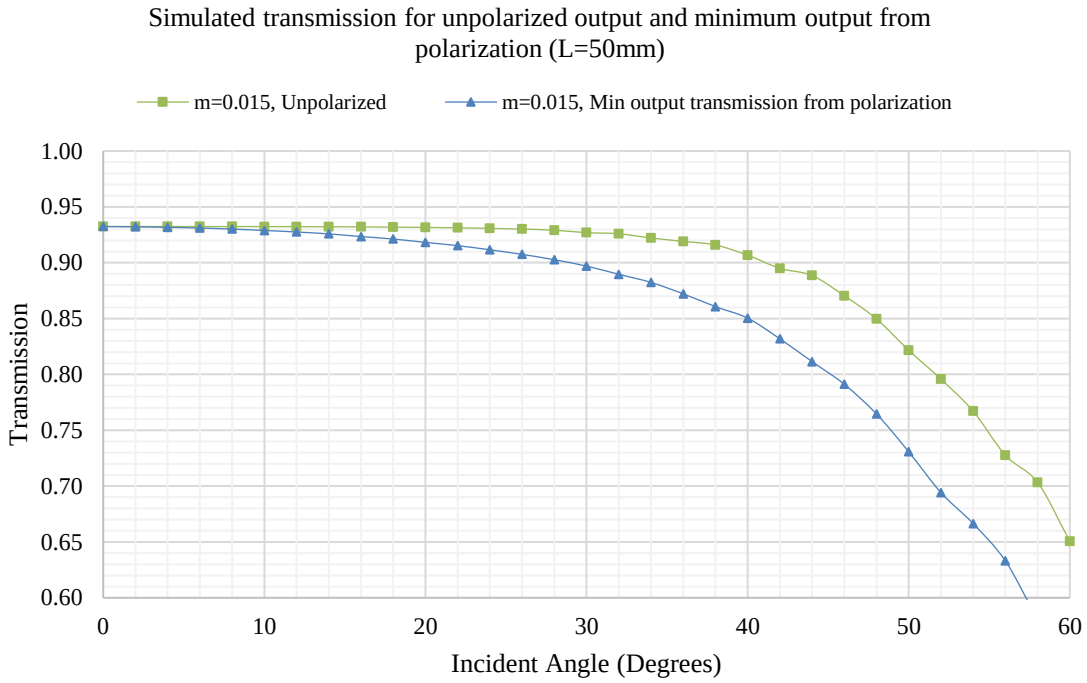

Figure 5.22 Effect of polarization on transmission modeling worst case scenario

Although the simulation indicates that the polarization can result in a higher decrease in the transmission at the lower angles, it should be noted that Figure 5.22 depicts the worst-case situation where the overall power output is minimized. In a realistic scenario, the reflectivity will likely be due to a combination of s- and p-polarizations, due to the randomness of the rough surfaces. Since we experience higher losses for the measurement, we do not expect any polarization dependency to significantly impact our results.

5.4. Experimental Fit With Loss Compensation

For the following simulations, a low support mount reflectivity (R_m) of 0.35 for a mount-fused silica interface is assumed for all samples, i.e. similar to one mount measured for a mount-air interface (see Appendix C). A finite sidewall loss is also assumed. Figure 5.23, Figure 5.24 and Figure 5.25 show the comparison between the experiment and simulation for the 30mm, 50mm and 70mm light pipes respectively.

A sidewall loss of approximately 0.25% to 0.5% is estimated for the 30mm sample, 0.3% to 0.5% for the 50mm sample and 0.4% to 0.6% for the 70mm sample. It should be noted that, for the 70mm sample, the transmission is slightly higher in one direction than the other. While the wavelengths 600nm and 700nm show slightly higher transmission compared to 500nm, this may be due to the support mounts (see Appendix C). A divergence half angle of 0.17 degrees into the light pipe, as estimated experimentally, is also assumed while we also acknowledge that the simulation may not perfectly capture any potential scattering phenomena from internal reflection due to rough surfaces or potential subsurface defects. This may result in increased losses due to the support mounts and dissimilar transmission for two input directions due to asymmetry, as illustrated in Figure 5.19 and Figure 5.20.

Based on these results, we estimate a 0.4% to 0.5% sidewall loss as being common for our fabricated light pipes with a broader range being from 0.25% to 0.6%.

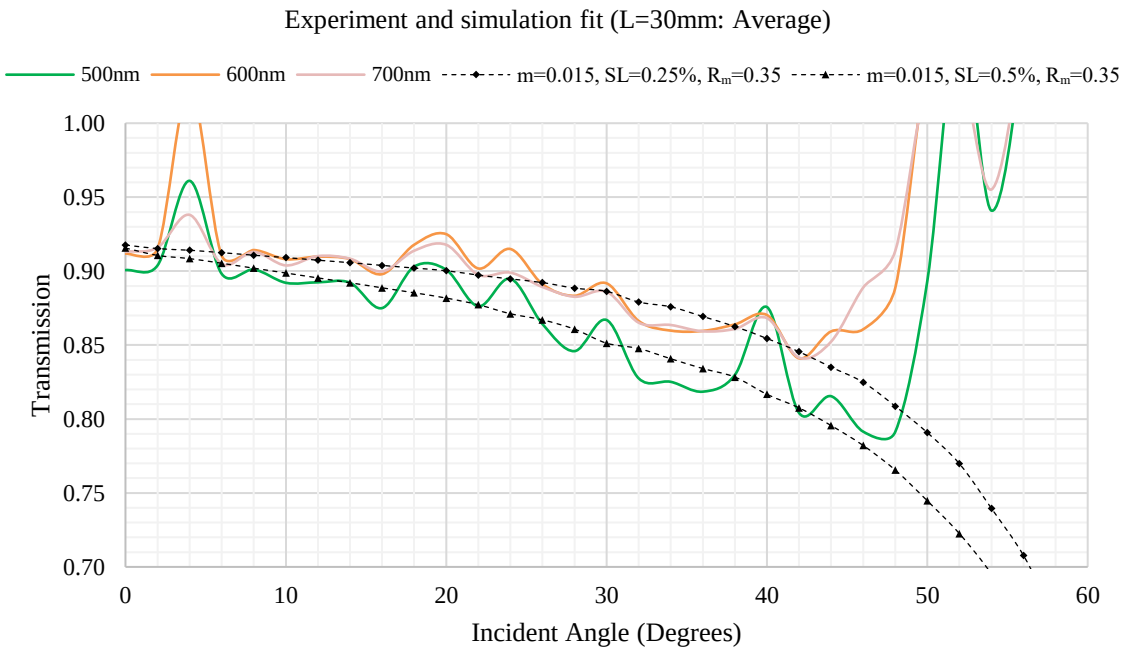

Figure 5.23 Simulation fit with sidewall loss and support mount reflectivity (30mm)

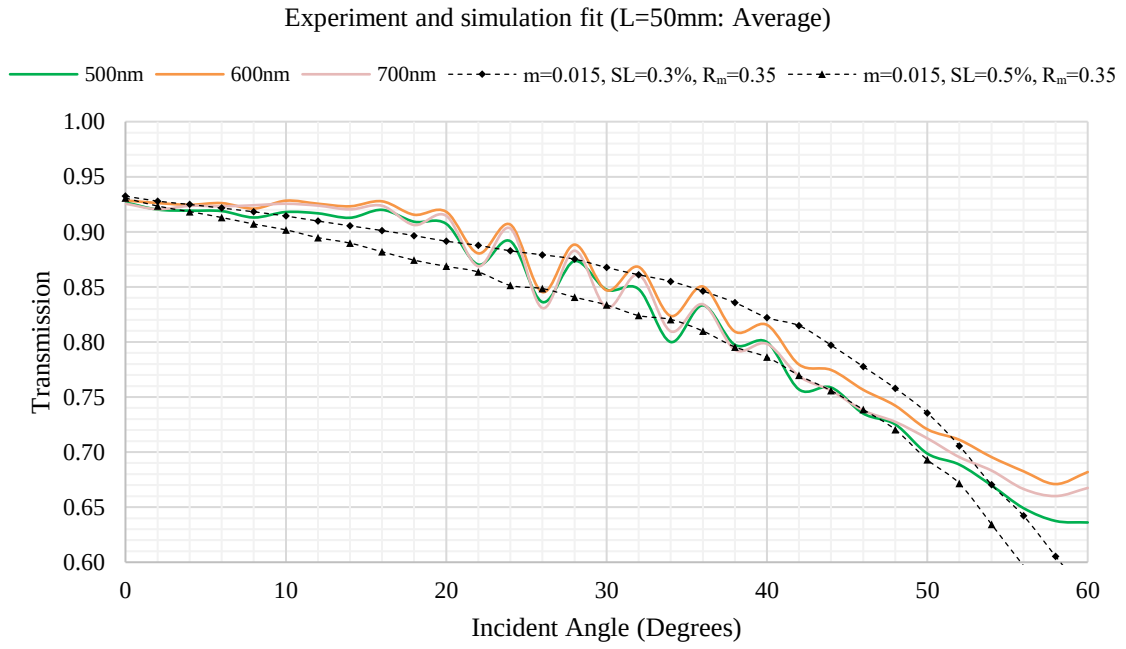

Figure 5.24 Simulation fit with sidewall loss and support mount reflectivity (50mm)

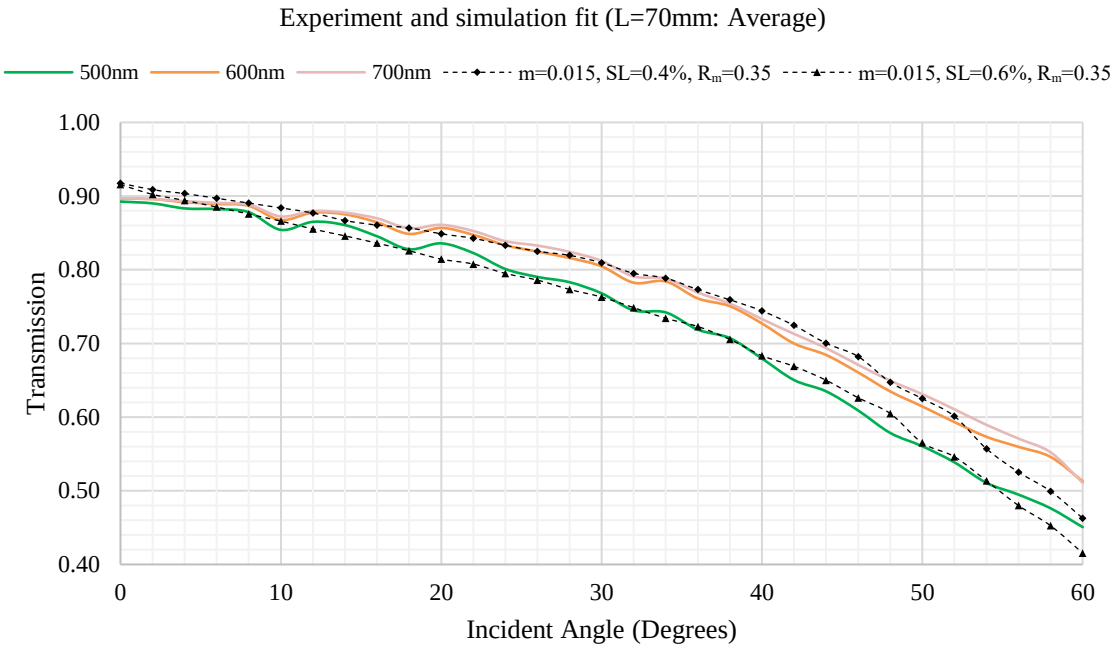

Figure 5.25 Simulation fit with sidewall loss and support mount reflectivity (70mm)

6. CONCLUSIONS

We described a procedure for polishing fused silica light pipes and measuring their transmission, and analyzed the geometric optics method as a means of modeling the optical losses based on finite sidewall roughness of the light pipes. We achieve relatively defect-free surfaces for the sidewalls of the light pipe after polishing using a CO_2 laser, and estimated the RMS slope for the polished surfaces to be 0.015 or lower as a benchmark. The geometric optics method shows lower transmission as RMS slope increases, while the RMS height has no effect on the transmission. Based on this method, while the transmission shows a rather linear reduction trend as incident angle increases while the simulation does not, we demonstrate other possible mechanisms for loss. Particularly finite and relatively constant losses, possibly from small subsurface defects or other imperfections arising from the fabrication process, can give rise to high losses and a relatively linear decrease in transmission at lower incident angles. From this, we estimate a polished sidewall loss of approximately 0.4% to 0.5% as being common for our samples based on simulation fit incorporating a constant sidewall loss term. Large scattering effects, for example from a damaged subsurface layer particularly in conjunction with finite constant losses from the support mounts holding the light pipe, may also lower the measured transmission.

REFERENCES

[1] M. Nair, K. Ramamurthy, and A. Ganesan, “Classification of indoor daylight enhancement systems,” *Light. Res. Technol.*, vol. 46, no. 3, pp. 245–267, Jun. 2013.

[2] A. Rosemann and H. Kaase, “Lightpipe applications for daylighting systems,” *Sol. Energy*, vol. 78, no. 6, pp. 772–780, Jun. 2005.

[3] H. Murat, A. Gielen, and H. De Smet, “Gradually tapered light pipes for illumination of LED projectors,” *J. Soc. Inf. Disp.*, vol. 15, no. 7, pp. 519–526, Jul. 2007.

[4] O. Selimoglu and R. Turan, “Exploration of the horizontally staggered light guides for high concentration CPV applications,” *Opt. Express*, vol. 20, no. 17, pp. 19137–19147, Aug. 2012.

[5] C. K. Madsen, Y. Dogan, M. Morrison, C. Hu, and R. Atkins, “Glass light pipes for solar concentration,” presented at the Proc.SPIE, 2018, vol. 10520.

[6] R. Kitamura, L. Pilon, and M. Jonasz, “Optical constants of silica glass from extreme ultraviolet to far infrared at near room temperature,” *Appl. Opt.*, vol. 46, no. 33, pp. 8118–8133, Nov. 2007.

[7] A. T. Mecherikunnel, J. A. Gatlin, and J. C. Richmond, “Data on total and spectral solar irradiance,” *Appl. Opt.*, vol. 22, no. 9, pp. 1354–1359, May 1983.

[8] J. T. Remillard, M. P. Everson, and W. H. Weber, “Loss mechanisms in optical light pipes,” *Appl. Opt.*, vol. 31, no. 34, pp. 7232–7241, Dec. 1992.

[9] R. Hunsperger, “Chapter 6 Losses in Optical Waveguides,” in *Integrated Optics: Theory and Technology*, 6th ed., New York: Springer, 2009.

[10] J. C. Stover, *Optical Scattering: Measurement and Analysis*, 2nd ed. Bellingham: SPIE, 1995.

[11] J. E. Harvey, N. Choi, S. Schroeder, and A. Duparré, "Total integrated scatter from surfaces with arbitrary roughness, correlation widths, and incident angles," *Opt. Eng.*, vol. 51, no. 1, pp. 1–12, Feb. 2012.

[12] F. E. Nicodemus, J. C. Richmond, J. J. Hsia, I. W. Ginsberg, and T. Limperis, "Geometrical considerations and nomenclature for reflectance," U.S. Department of Commerce, Washington, D.C., Oct. 1977.

[13] S. Schröder, A. Duparré, L. Coriand, A. Tünnermann, D. H. Penalver, and J. E. Harvey, "Modeling of light scattering in different regimes of surface roughness," *Opt. Express*, vol. 19, no. 10, pp. 9820–9835, May 2011.

[14] J. E. Harvey and R. N. Pfisterer, "Comparison of the GHS Smooth and the Rayleigh-Rice surface scatter theories," presented at the Proc.SPIE, 2016, vol. 9961.

[15] J. E. Harvey, N. Choi, A. Krywonos, and J. G. Marcen, "Calculating BRDFs from surface PSDs for moderately rough optical surfaces," presented at the Proc.SPIE, 2009, vol. 7426.

[16] C. K. Madsen, Y. Dogan, C. Hu, M. Morrison, and R. Atkins, "Femtosecond-laser-based prototyping of light pipe circuits," presented at the Proc.SPIE, 2019, vol. 10906.

[17] P. Cormont, P. Combis, L. Gallais, C. Hecquet, L. Lamaignère, and J. L. Rullier, "Removal of scratches on fused silica optics by using a CO2 laser," *Opt. Express*, vol. 21, no. 23, pp. 28272–28289, Nov. 2013.

[18] C. Weingarten, A. Schmickler, E. Willenborg, K. Wissenbach, and R. Poprawe, “Laser polishing and laser shape correction of optical glass,” *J. Laser Appl.*, vol. 29, no. 1, p. 011702, Feb. 2017.

[19] D. Bergström, J. Powell, and A. F. H. Kaplan, “The absorption of light by rough metal surfaces—A three-dimensional ray-tracing analysis,” *J. Appl. Phys.*, vol. 103, no. 10, p. 103515, May 2008.

[20] M. Mrnka, “Random gaussian rough surfaces for full-wave electromagnetic simulations,” in *2017 Conference on Microwave Techniques (COMITE)*, 2017, pp. 1–4.

[21] R. Paschotta, *Field Guide to Lasers*. Bellingham: SPIE, 2008.

[22] B. de Greve, “Reflections and Refractions in Ray Tracing.” 13-Nov-2006.

[23] E. Hecht, *Optics*, 5th ed. Essex: Pearson, 2017.

[24] M. Polyanskiy, “Optical constants of Fused silica (fused quartz),” *Refractive index database*. [Online]. Available: https://refractiveindex.info/?shelf=glass&book=fused_silica&page=Malitson. [Accessed: 18-May-2019].

[25] M. Polyanskiy, “Optical constants of BK7,” *Refractive index database*. [Online]. Available: https://refractiveindex.info/?shelf=glass&book=BK7&page=SCHOTT. [Accessed: 18-May-2019].

APPENDIX A

THORLABS S142C DETECTOR UNCERTAINTY

Figure A.1 shows a schematic of the Thorlabs S142C detector. Figure A.2 and Figure A.3 show the angular dependence of the ratio of the detected power from left to right compared to normal incidence. Figure A.4 shows the angular dependence for the bottom to top scenario.

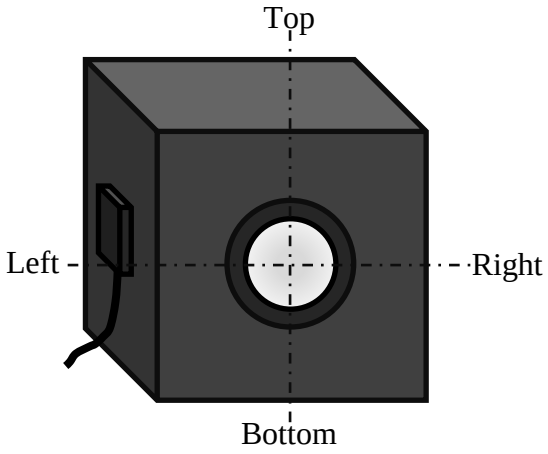

Figure A.1 Schematic of Thorlabs S142C detector

The observed angular distribution for the light pipe samples is in the form of a corona expanding about the output facet with a divergence half angle approximately equal to the incident angle at the input (see Appendix D). Since there is a sharp change in the detector's estimation for angles above 40 degrees, we believe the measurement results are reliable up to 40 degrees.

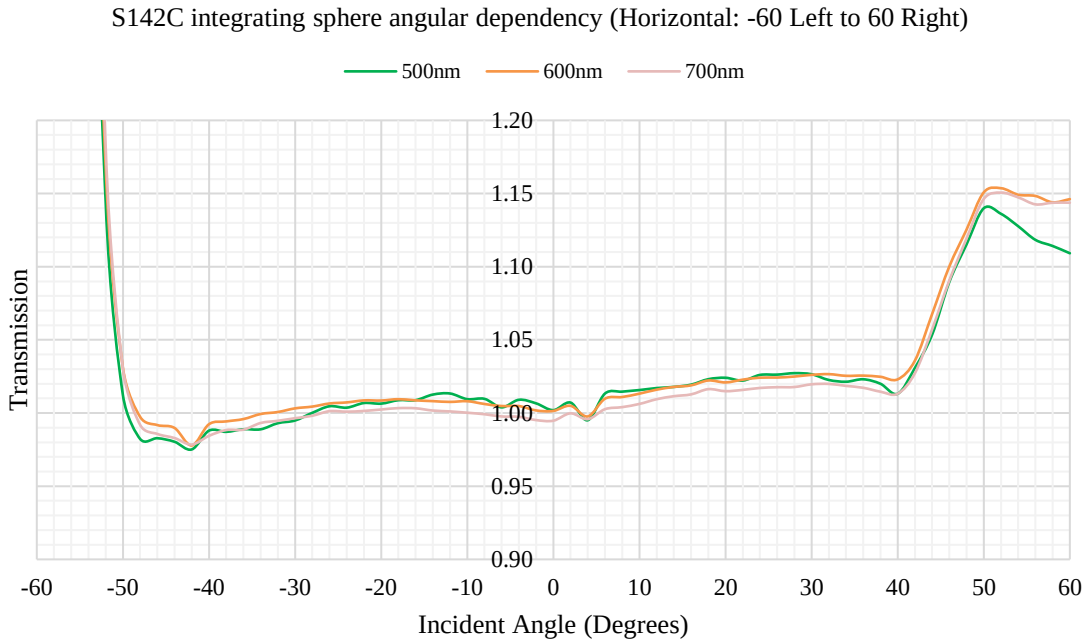

Figure A.2 Angular dependence of Thorlabs S142C from left to right compared to normal incidence – zoomed in

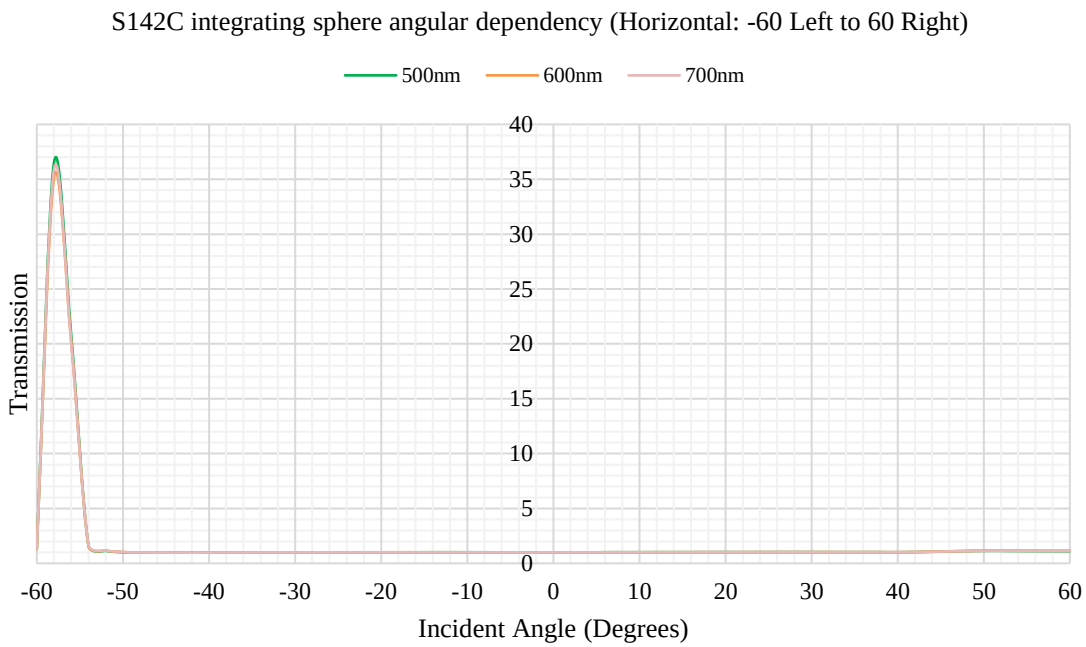

Figure A.3 Angular dependence of Thorlabs S142C from left to right compared to normal incidence – overall transmission

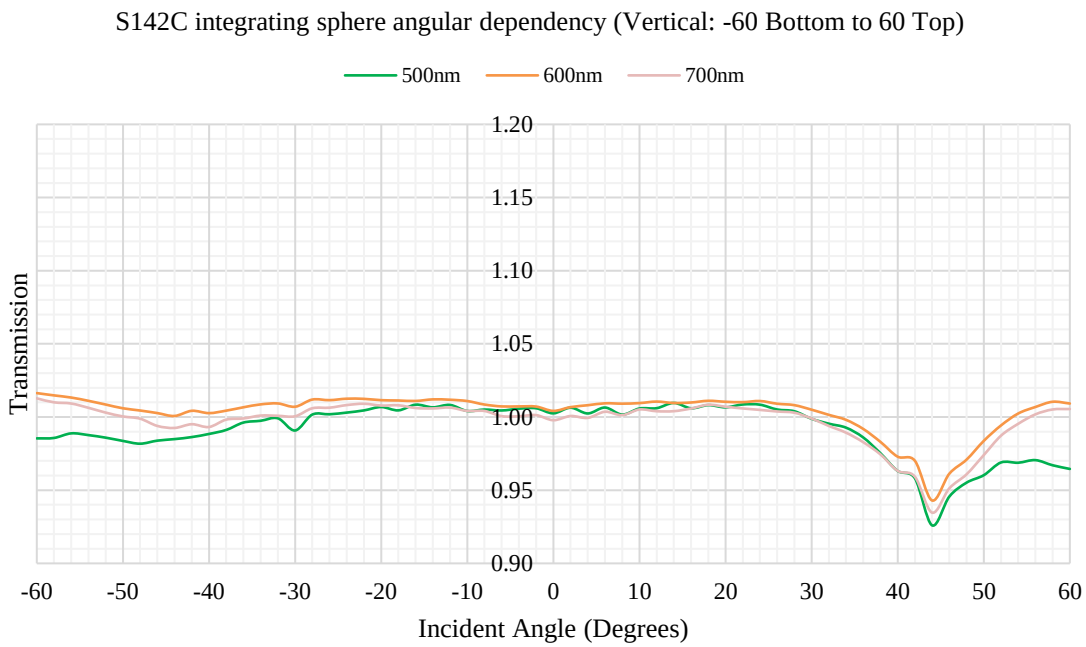

Figure A.4 Angular dependence of Thorlabs S142C from bottom to top compared to normal incidence

Table A.1 shows an average percentage estimation discrepancy of 1.4% maximum up to 40 degrees. This small change is neglected in the measurement results.

Table A.1 Average percentage adjustment of transmission for different incident angles

Angle(º)	500nm	600nm	700nm	Angle(º)	500nm	600nm	700nm
0	0.00%	0.00%	0.00%	32	0.03%	0.67%	0.61%
2	0.43%	0.23%	0.30%	34	-0.21%	0.50%	0.42%
4	0.08%	0.16%	0.20%	36	-0.37%	0.22%	0.06%
6	0.48%	0.50%	0.48%	38	-0.88%	-0.12%	-0.24%
8	0.55%	0.59%	0.59%	40	-1.40%	-0.51%	-0.78%
10	0.65%	0.76%	0.77%	42	-1.46%	-0.58%	-0.63%
12	0.89%	0.86%	0.90%	44	-1.60%	-0.25%	-0.45%
14	0.94%	0.91%	0.95%	46	-0.18%	1.11%	0.91%
16	0.84%	0.93%	1.07%	48	0.64%	2.16%	2.15%
18	0.89%	1.07%	1.28%	50	2.18%	3.99%	4.18%
20	0.87%	1.00%	1.18%	52	5.64%	7.82%	8.47%
22	0.83%	1.07%	1.18%	54	17.09%	19.50%	21.24%
24	0.80%	1.09%	1.15%	56	494.4%	482.3%	482.1%
26	0.72%	1.00%	1.10%	58	887.4%	855.5%	879.6%
28	0.60%	0.95%	1.00%	60	8.83%	11.40%	12.13%
30	0.05%	0.75%	0.76%				

APPENDIX B

LIGHT PIPE MEASUREMENT TRANSMISSION DATA

The following figures and tables show the measured transmission for fused silica light pipes of lengths 30mm, 50mm and 70mm. The light pipe samples are mounted on top of two silver support mounts with polished sides facing the side and smooth sides facing top and bottom. Each sample is measured in different orientations, labeled (1), (2), (3) and (4) using the Thorlabs S142C integrating sphere, at incident angles ranging from 0 degrees to 60 degrees testing the polished sides. Refer to Figure 5.6, Figure 5.8 and Figure 5.10 for a visual illustration of the orientations tested.

It should be noted that more anomalies are seen on the measurement results for the 30mm sample compared to the 50mm and 70mm samples. For example, the 30mm sample shows a transmission of greater than unity for incident angles greater than 45 degrees, for some measurement directions. At the output facet of the samples, we observe intensity patterns such as that shown in Figure D.1 at different input incident angles (see Appendix D). While a circular pattern is observed for the 30mm sample, it is less prominent, and much of the output intensity resides on the plane where the incident angle is adjusted, similar to the simulated output in Figure D.2. This, in conjunction with detector overestimation at certain angles (see Appendix A), likely results in a measured transmission of greater than unity for the 30mm sample. Longer samples may give rise to a more circular output distribution, likely due to more reflections, while, for shorter samples, the output distribution follows more closely that predicted by geometric optics.

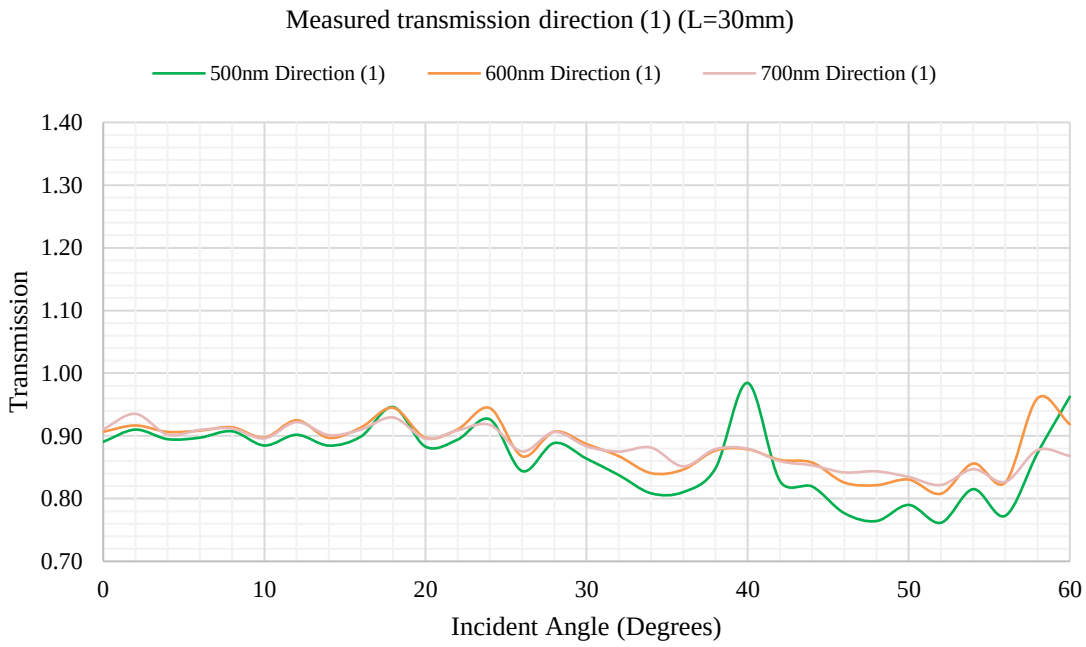

Figure B.1 30mm sample transmission direction (1) – graphical data

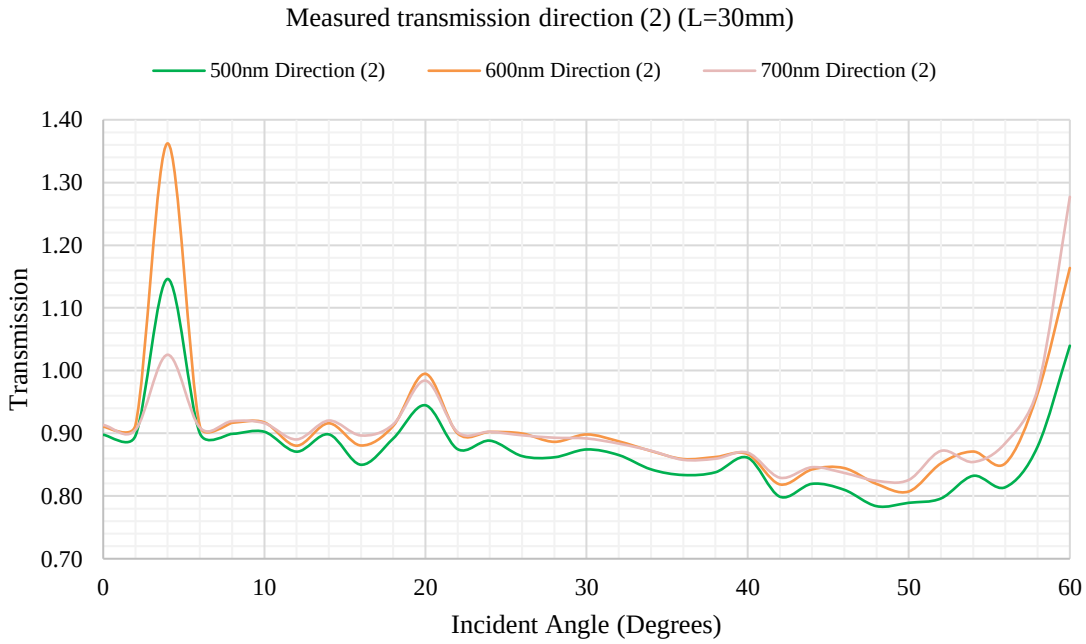

Figure B.2 30mm sample transmission direction (2) – graphical data

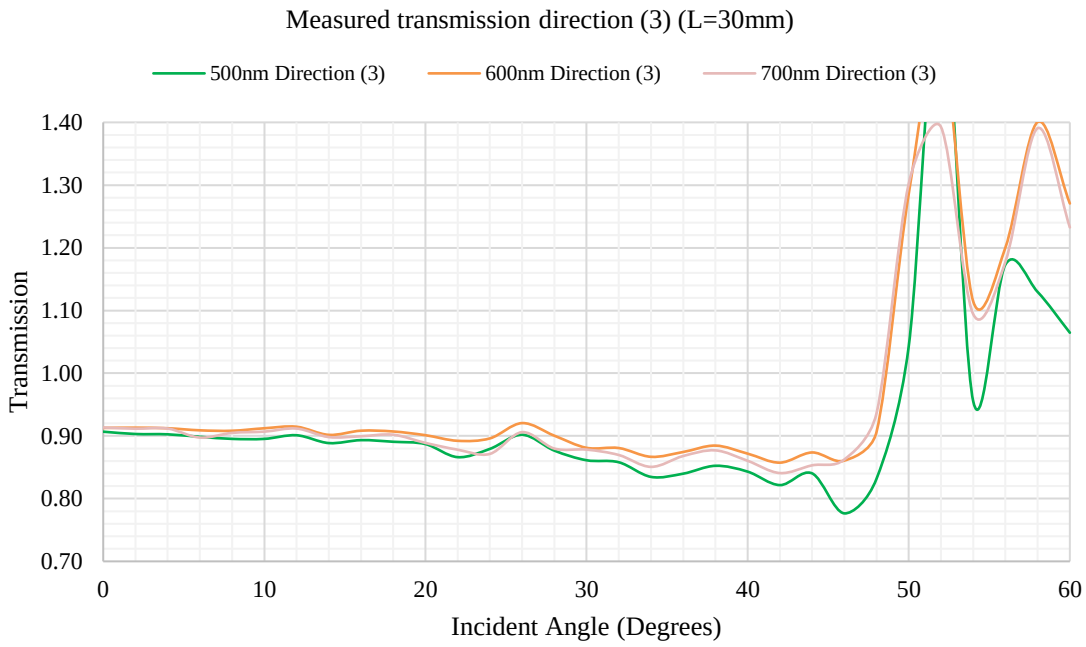

Figure B.3 30mm sample transmission direction (3) – graphical data

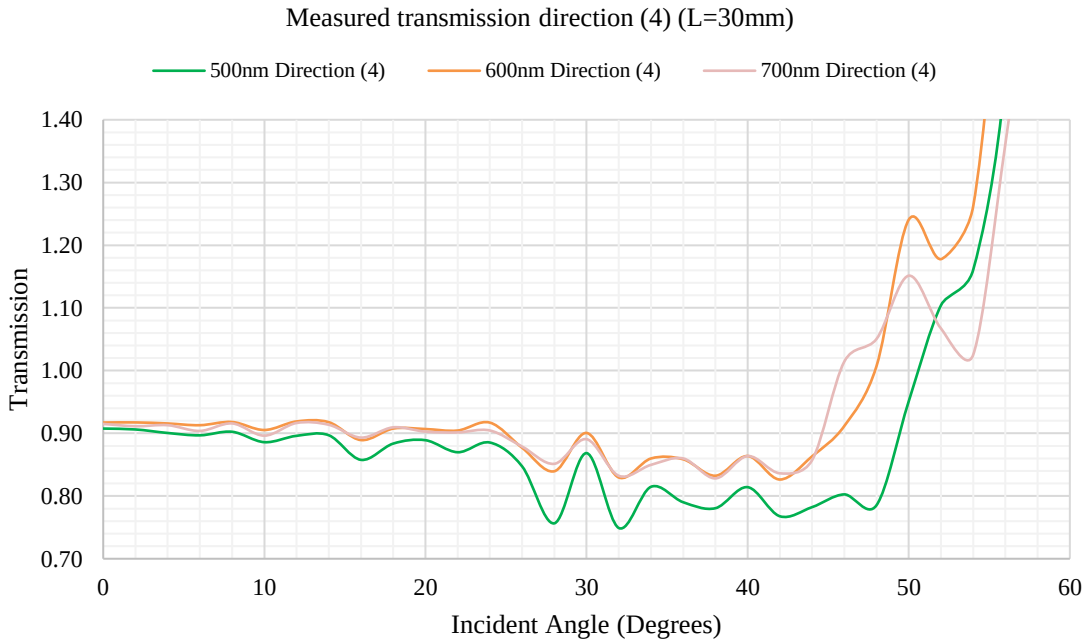

Figure B.4 30mm sample transmission direction (4) – graphical data

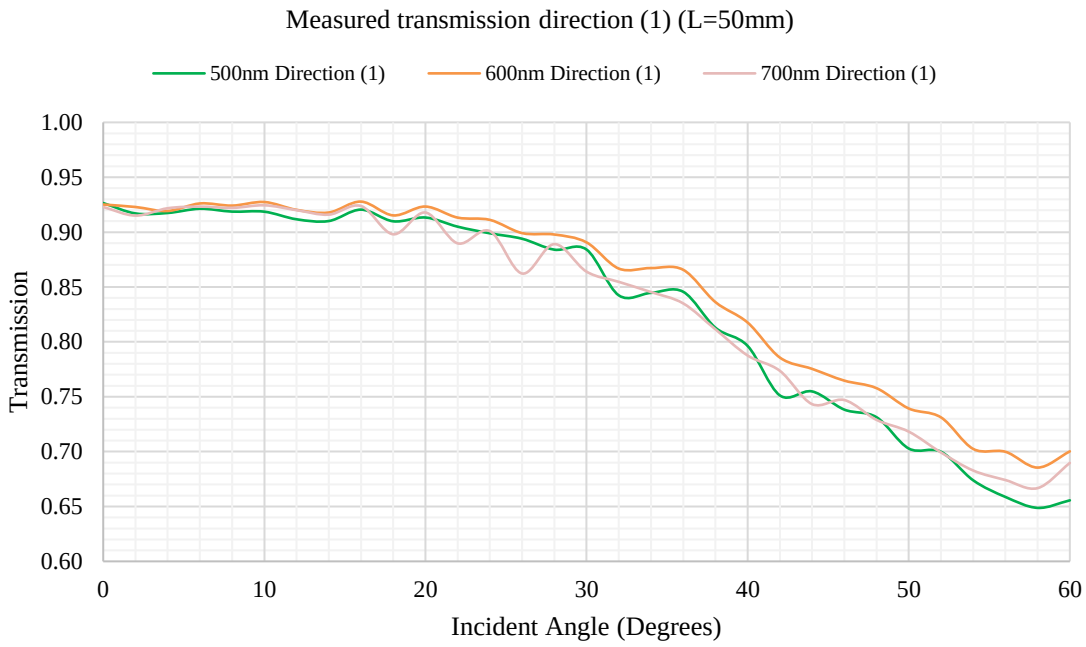

Figure B.5 50mm sample transmission direction (1) – graphical data

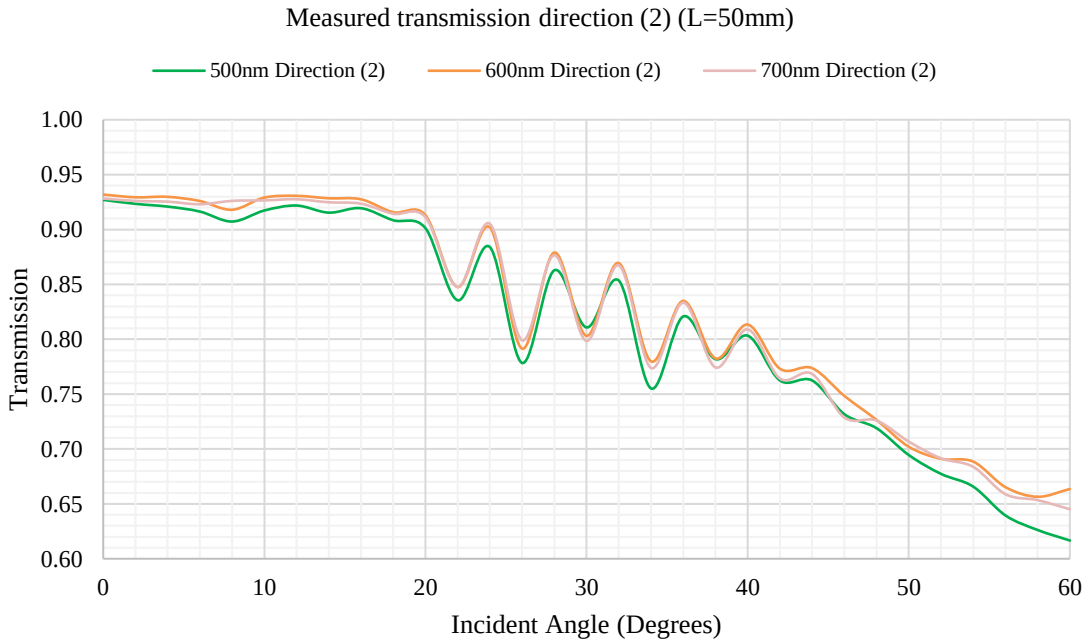

Figure B.6 50mm sample transmission direction (2) – graphical data

Figure B.7 70mm sample transmission direction (1) – graphical data

Figure B.8 70mm sample transmission direction (2) – graphical data

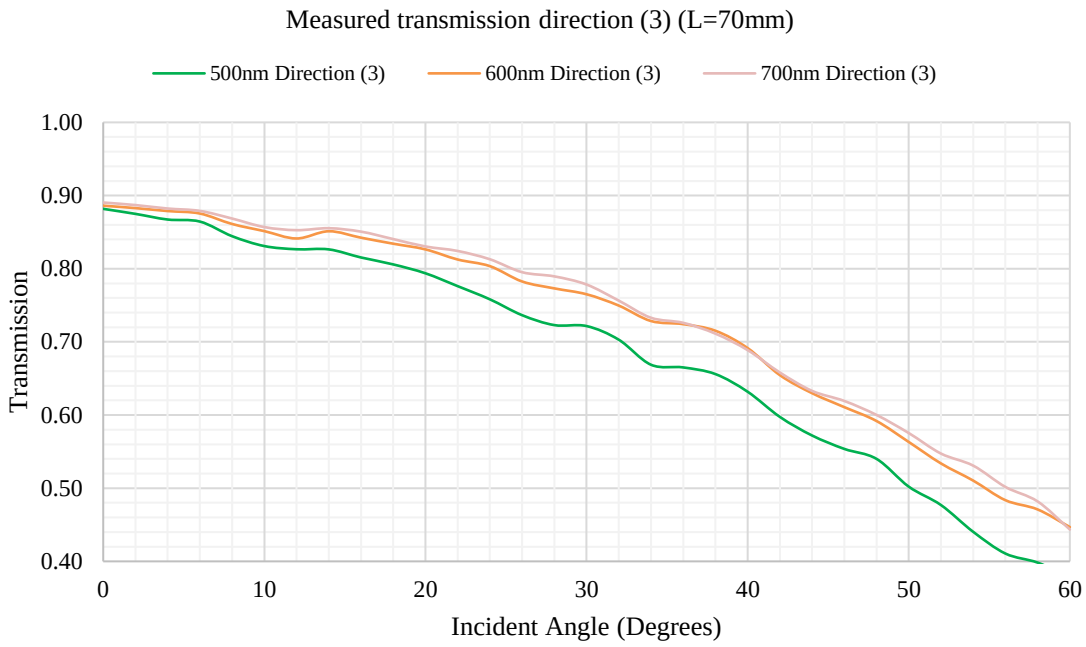

Figure B.9 70mm sample transmission direction (3) – graphical data

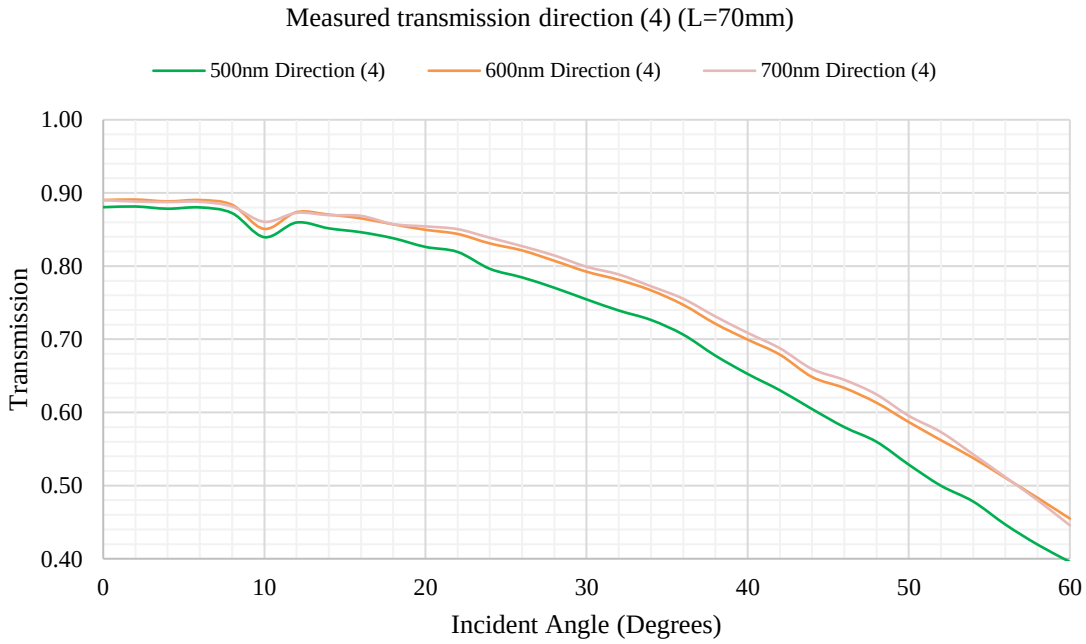

Figure B.10 70mm sample transmission direction (4) – graphical data

Table B.1 30mm sample transmission direction (1) – tabular data

Angle(º)	500nm	600nm	700nm	Angle(º)	500nm	600nm	700nm
0	0.891	0.907	0.911	32	0.838	0.868	0.875
2	0.910	0.917	0.935	34	0.809	0.841	0.882
4	0.895	0.906	0.902	36	0.810	0.846	0.851
6	0.897	0.908	0.910	38	0.848	0.877	0.879
8	0.907	0.914	0.912	40	0.984	0.879	0.880
10	0.885	0.897	0.896	42	0.828	0.862	0.860
12	0.902	0.925	0.922	44	0.819	0.858	0.853
14	0.885	0.897	0.901	46	0.777	0.826	0.842
16	0.899	0.914	0.910	48	0.764	0.821	0.844
18	0.946	0.945	0.929	50	0.790	0.830	0.835
20	0.883	0.897	0.896	52	0.762	0.808	0.822
22	0.894	0.911	0.909	54	0.815	0.856	0.847
24	0.926	0.944	0.918	56	0.773	0.826	0.827
26	0.844	0.868	0.875	58	0.873	0.960	0.878
28	0.889	0.907	0.906	60	0.963	0.918	0.868
30	0.864	0.887	0.884				

Table B.2 30mm sample transmission direction (2) – tabular data

Angle(º)	500nm	600nm	700nm	Angle(º)	500nm	600nm	700nm
0	0.898	0.911	0.913	32	0.865	0.887	0.884
2	0.896	0.913	0.905	34	0.843	0.872	0.872
4	1.146	1.362	1.025	36	0.834	0.859	0.858
6	0.900	0.911	0.909	38	0.838	0.862	0.860
8	0.899	0.917	0.919	40	0.861	0.867	0.869
10	0.903	0.917	0.916	42	0.799	0.819	0.829
12	0.871	0.880	0.890	44	0.820	0.842	0.846
14	0.898	0.916	0.920	46	0.810	0.845	0.837
16	0.850	0.881	0.897	48	0.784	0.819	0.824
18	0.892	0.912	0.914	50	0.789	0.807	0.826
20	0.945	0.995	0.984	52	0.796	0.852	0.872
22	0.875	0.900	0.902	54	0.832	0.871	0.854
24	0.888	0.902	0.902	56	0.814	0.852	0.885
26	0.864	0.900	0.897	58	0.879	0.964	0.971
28	0.862	0.886	0.893	60	1.040	1.164	1.277
30	0.874	0.898	0.892				

Table B.3 30mm sample transmission direction (3) – tabular data

Angle(º)	500nm	600nm	700nm	Angle(º)	500nm	600nm	700nm
0	0.907	0.913	0.913	32	0.858	0.881	0.870
2	0.903	0.913	0.912	34	0.835	0.867	0.851
4	0.903	0.912	0.912	36	0.840	0.874	0.868
6	0.899	0.909	0.897	38	0.852	0.885	0.877
8	0.895	0.908	0.905	40	0.843	0.872	0.860
10	0.895	0.912	0.907	42	0.822	0.857	0.841
12	0.901	0.915	0.912	44	0.840	0.874	0.853
14	0.889	0.902	0.898	46	0.777	0.861	0.862
16	0.893	0.908	0.900	48	0.832	0.906	0.936
18	0.891	0.907	0.902	50	1.043	1.286	1.302
20	0.887	0.901	0.889	52	1.630	1.531	1.393
22	0.866	0.892	0.878	54	0.955	1.115	1.094
24	0.879	0.896	0.871	56	1.173	1.200	1.178
26	0.902	0.920	0.906	58	1.130	1.401	1.391
28	0.877	0.900	0.880	60	1.065	1.271	1.233
30	0.861	0.881	0.878				

Table B.4 30mm sample transmission direction (4) – tabular data

Angle(º)	500nm	600nm	700nm	Angle(º)	500nm	600nm	700nm
0	0.908	0.917	0.915	32	0.749	0.830	0.832
2	0.906	0.917	0.911	34	0.815	0.860	0.850
4	0.901	0.916	0.913	36	0.790	0.859	0.860
6	0.897	0.913	0.904	38	0.781	0.832	0.828
8	0.902	0.918	0.916	40	0.814	0.864	0.864
10	0.886	0.905	0.896	42	0.768	0.826	0.836
12	0.896	0.919	0.917	44	0.782	0.863	0.857
14	0.897	0.918	0.914	46	0.803	0.912	1.014
16	0.858	0.889	0.893	48	0.785	1.007	1.050
18	0.884	0.908	0.910	50	0.951	1.241	1.151
20	0.889	0.907	0.903	52	1.104	1.178	1.067
22	0.870	0.904	0.901	54	1.161	1.262	1.025
24	0.885	0.917	0.905	56	1.473	1.763	1.362
26	0.847	0.877	0.879	58	2.322	2.399	1.729
28	0.756	0.840	0.851	60	1.754	1.993	1.768
30	0.868	0.901	0.891				

Table B.5 50mm sample transmission direction (1) – tabular data

Angle(º)	500nm	600nm	700nm	Angle(º)	500nm	600nm	700nm
0	0.926	0.925	0.923	32	0.842	0.867	0.855
2	0.917	0.923	0.915	34	0.845	0.867	0.845
4	0.917	0.919	0.922	36	0.846	0.866	0.835
6	0.921	0.926	0.923	38	0.813	0.836	0.811
8	0.919	0.924	0.922	40	0.796	0.818	0.788
10	0.919	0.927	0.924	42	0.751	0.786	0.774
12	0.912	0.920	0.920	44	0.755	0.775	0.743
14	0.910	0.918	0.916	46	0.738	0.765	0.747
16	0.920	0.928	0.924	48	0.731	0.758	0.729
18	0.910	0.915	0.898	50	0.703	0.739	0.718
20	0.913	0.923	0.918	52	0.700	0.731	0.699
22	0.905	0.913	0.890	54	0.674	0.702	0.683
24	0.899	0.911	0.901	56	0.659	0.700	0.674
26	0.894	0.899	0.862	58	0.649	0.685	0.667
28	0.884	0.898	0.889	60	0.656	0.700	0.690
30	0.884	0.891	0.864				

Table B.6 50mm sample transmission direction (2) – tabular data

Angle(º)	500nm	600nm	700nm	Angle(º)	500nm	600nm	700nm
0	0.927	0.932	0.928	32	0.854	0.869	0.867
2	0.923	0.929	0.926	34	0.755	0.780	0.774
4	0.921	0.930	0.925	36	0.821	0.835	0.833
6	0.916	0.926	0.923	38	0.782	0.783	0.774
8	0.907	0.918	0.926	40	0.803	0.813	0.809
10	0.917	0.929	0.927	42	0.763	0.773	0.764
12	0.922	0.931	0.928	44	0.762	0.774	0.768
14	0.915	0.928	0.925	46	0.732	0.748	0.729
16	0.919	0.928	0.924	48	0.719	0.727	0.726
18	0.908	0.916	0.914	50	0.695	0.702	0.707
20	0.901	0.913	0.911	52	0.677	0.691	0.692
22	0.836	0.848	0.848	54	0.666	0.689	0.684
24	0.884	0.902	0.905	56	0.640	0.665	0.659
26	0.778	0.791	0.799	58	0.626	0.656	0.653
28	0.863	0.879	0.877	60	0.617	0.664	0.645
30	0.811	0.803	0.799				

Table B.7 70mm sample transmission direction (1) – tabular data

Angle(º)	500nm	600nm	700nm	Angle(º)	500nm	600nm	700nm
0	0.904	0.901	0.904	32	0.765	0.792	0.806
2	0.905	0.905	0.907	34	0.792	0.810	0.815
4	0.896	0.898	0.900	36	0.729	0.770	0.777
6	0.888	0.888	0.894	38	0.744	0.779	0.783
8	0.899	0.895	0.899	40	0.726	0.772	0.780
10	0.863	0.872	0.880	42	0.718	0.760	0.773
12	0.889	0.897	0.896	44	0.682	0.723	0.735
14	0.890	0.899	0.903	46	0.631	0.684	0.700
16	0.870	0.883	0.892	48	0.595	0.650	0.673
18	0.847	0.862	0.874	50	0.592	0.652	0.661
20	0.850	0.857	0.870	52	0.564	0.617	0.635
22	0.853	0.870	0.865	54	0.548	0.622	0.640
24	0.816	0.839	0.844	56	0.583	0.658	0.667
26	0.826	0.847	0.849	58	0.569	0.637	0.643
28	0.801	0.822	0.831	60	0.516	0.583	0.588
30	0.815	0.842	0.839				

Table B.8 70mm sample transmission direction (2) – tabular data

Angle(º)	500nm	600nm	700nm	Angle(º)	500nm	600nm	700nm
0	0.904	0.909	0.903	32	0.772	0.807	0.813
2	0.899	0.905	0.902	34	0.781	0.831	0.832
4	0.892	0.902	0.902	36	0.775	0.803	0.818
6	0.897	0.904	0.902	38	0.751	0.787	0.791
8	0.897	0.907	0.905	40	0.708	0.746	0.755
10	0.883	0.896	0.892	42	0.656	0.707	0.733
12	0.885	0.898	0.897	44	0.682	0.736	0.747
14	0.874	0.880	0.882	46	0.671	0.714	0.720
16	0.851	0.867	0.868	48	0.619	0.684	0.700
18	0.820	0.842	0.853	50	0.619	0.656	0.693
20	0.874	0.894	0.889	52	0.613	0.660	0.687
22	0.843	0.863	0.871	54	0.576	0.623	0.644
24	0.834	0.859	0.859	56	0.539	0.587	0.603
26	0.814	0.848	0.859	58	0.518	0.592	0.604
28	0.839	0.862	0.862	60	0.513	0.567	0.565
30	0.781	0.819	0.831				

Table B.9 70mm sample transmission direction (3) – tabular data

Angle(º)	500nm	600nm	700nm	Angle(º)	500nm	600nm	700nm
0	0.882	0.886	0.890	32	0.703	0.750	0.756
2	0.875	0.883	0.887	34	0.669	0.729	0.733
4	0.867	0.879	0.882	36	0.665	0.724	0.726
6	0.864	0.875	0.879	38	0.656	0.715	0.711
8	0.844	0.861	0.869	40	0.632	0.691	0.689
10	0.831	0.851	0.857	42	0.597	0.655	0.658
12	0.827	0.841	0.853	44	0.572	0.630	0.633
14	0.826	0.851	0.855	46	0.554	0.611	0.619
16	0.815	0.842	0.851	48	0.540	0.592	0.600
18	0.806	0.834	0.841	50	0.502	0.563	0.575
20	0.794	0.826	0.830	52	0.477	0.534	0.547
22	0.776	0.813	0.824	54	0.440	0.510	0.531
24	0.758	0.803	0.813	56	0.411	0.484	0.502
26	0.736	0.783	0.795	58	0.398	0.471	0.482
28	0.723	0.773	0.790	60	0.378	0.447	0.444
30	0.722	0.765	0.778				

Table B.10 70mm sample transmission direction (4) – tabular data

Angle(º)	500nm	600nm	700nm	Angle(º)	500nm	600nm	700nm
0	0.881	0.890	0.890	32	0.739	0.781	0.789
2	0.881	0.891	0.888	34	0.726	0.767	0.772
4	0.878	0.888	0.888	36	0.706	0.747	0.755
6	0.880	0.890	0.888	38	0.678	0.721	0.731
8	0.872	0.884	0.881	40	0.653	0.700	0.709
10	0.840	0.851	0.861	42	0.630	0.679	0.688
12	0.860	0.874	0.873	44	0.605	0.648	0.659
14	0.852	0.870	0.870	46	0.580	0.633	0.645
16	0.846	0.865	0.869	48	0.560	0.613	0.625
18	0.838	0.857	0.857	50	0.529	0.587	0.595
20	0.826	0.850	0.854	52	0.500	0.562	0.573
22	0.819	0.844	0.850	54	0.478	0.538	0.543
24	0.796	0.831	0.839	56	0.447	0.511	0.512
26	0.785	0.821	0.827	58	0.419	0.483	0.480
28	0.770	0.807	0.815	60	0.396	0.455	0.446
30	0.754	0.792	0.799				

APPENDIX C

SUPPORT MOUNT REFLECTIVITY (MOUNT-TO-AIR)

The support mounts consist of silver with silicon dioxide coating. Figure C.1 shows the reflectivity of the support mounts for two measured samples. Variation in the reflectivity for the mounts shown may be a result of the surface quality of the mounts tested. Note that the measured values may not be perfectly accurate due to an angular variation of the reflected beam approaching the Thorlabs S142C detector. The mount reflectivity is measured such that the reflectivity at 45 degrees corresponds to normal incidence into the detector. The beam into the detector is swept horizontally.

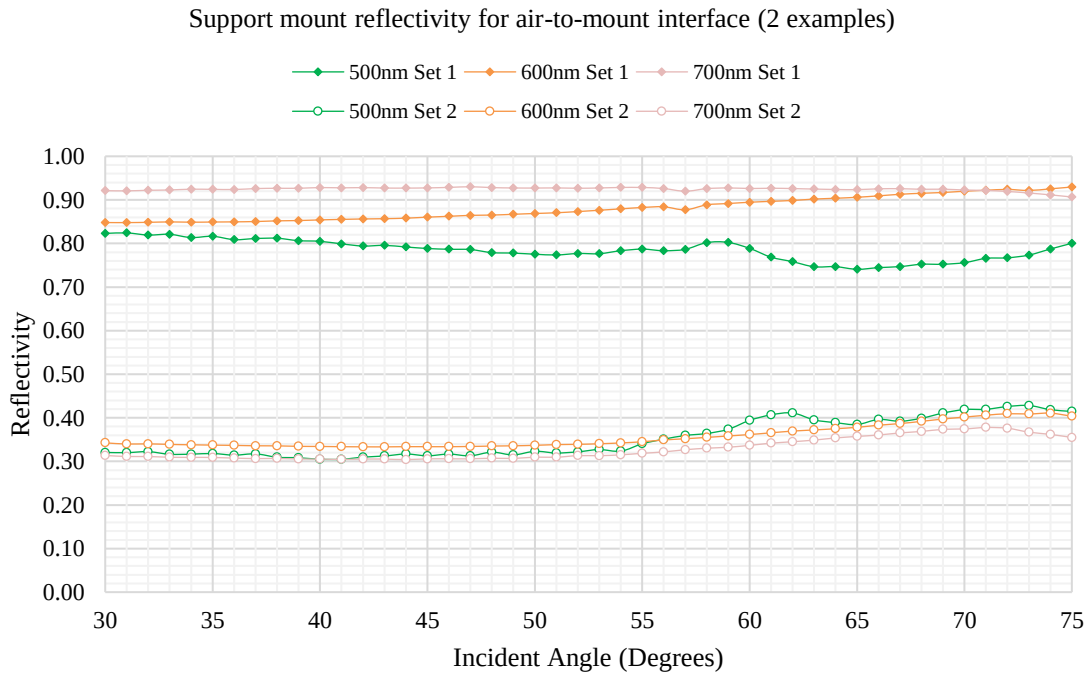

Figure C.1 Reflectivity of support mounts (Ag with SiO_2 coating) for 2 instances

APPENDIX D

EXPERIMENTAL VERSUS SIMULATED OUTPUT DISTRIBUTION

Figure D.1 shows the measured output intensity pattern of a 70mm light pipe sample 20mm away from the input facet for various input incident angles. The half angle divergence of the ring pattern follows approximately the incident angle at the input. We observe such an effect for our other samples, however the ring pattern is less prominent in the 30mm sample. In general, we also observe higher intensity at the points planar to the input incident angle where the output angle follows approximately the input incident angle such as that shown in Figure D.1(c)-(e).

The simulation however shows a ray output angular distribution centered around the input incident angle, shown in Figure D.2 for 20, 40 and 60 degrees incident angle, for 100 simulation runs, for a 50mm sample. This discrepancy is subject to further investigation.

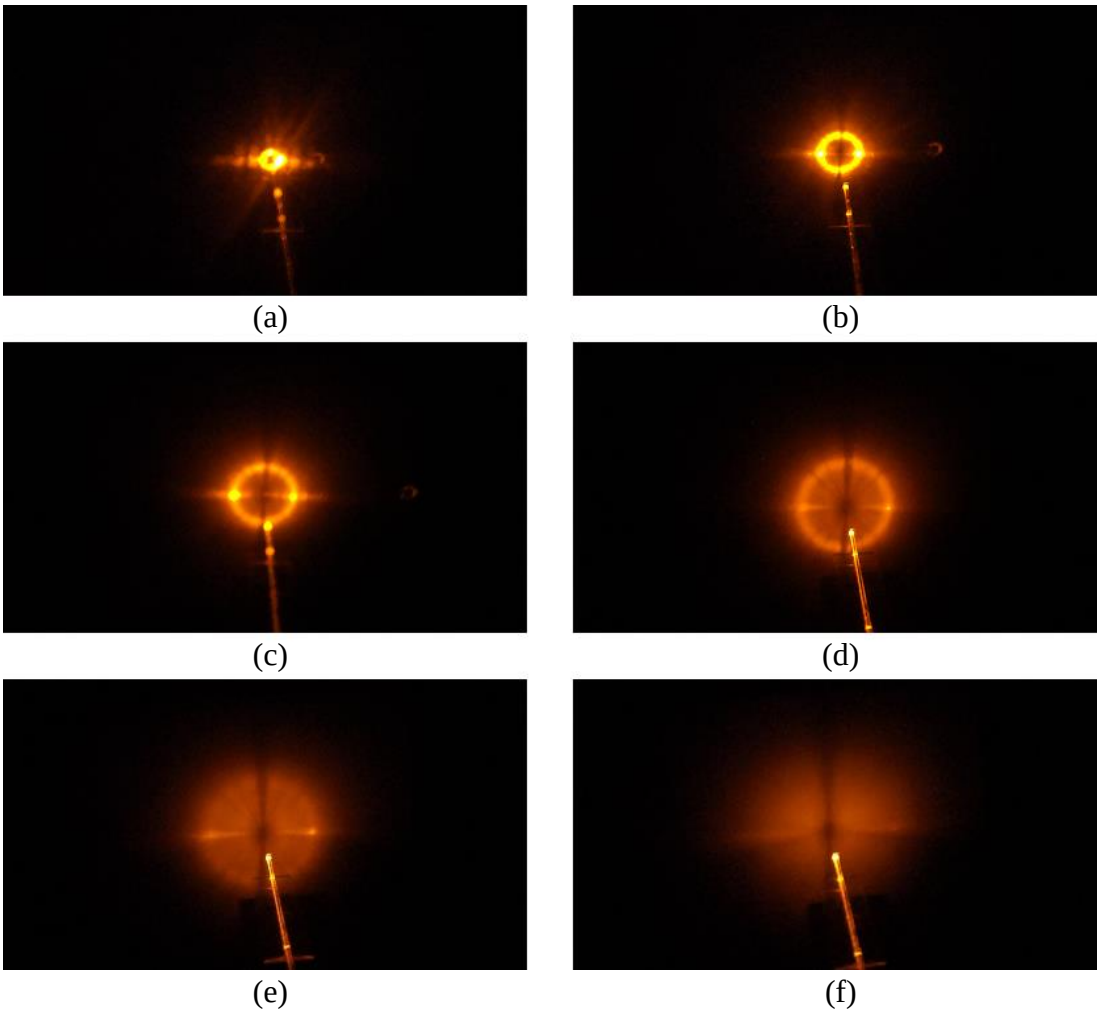

Figure D.1 Power distribution of 70mm sample for varying input incident angles 20mm from output facet; (a) 10°, (b) 20°, (c) 30°, (d) 40°, (e) 50°, (f) 60°

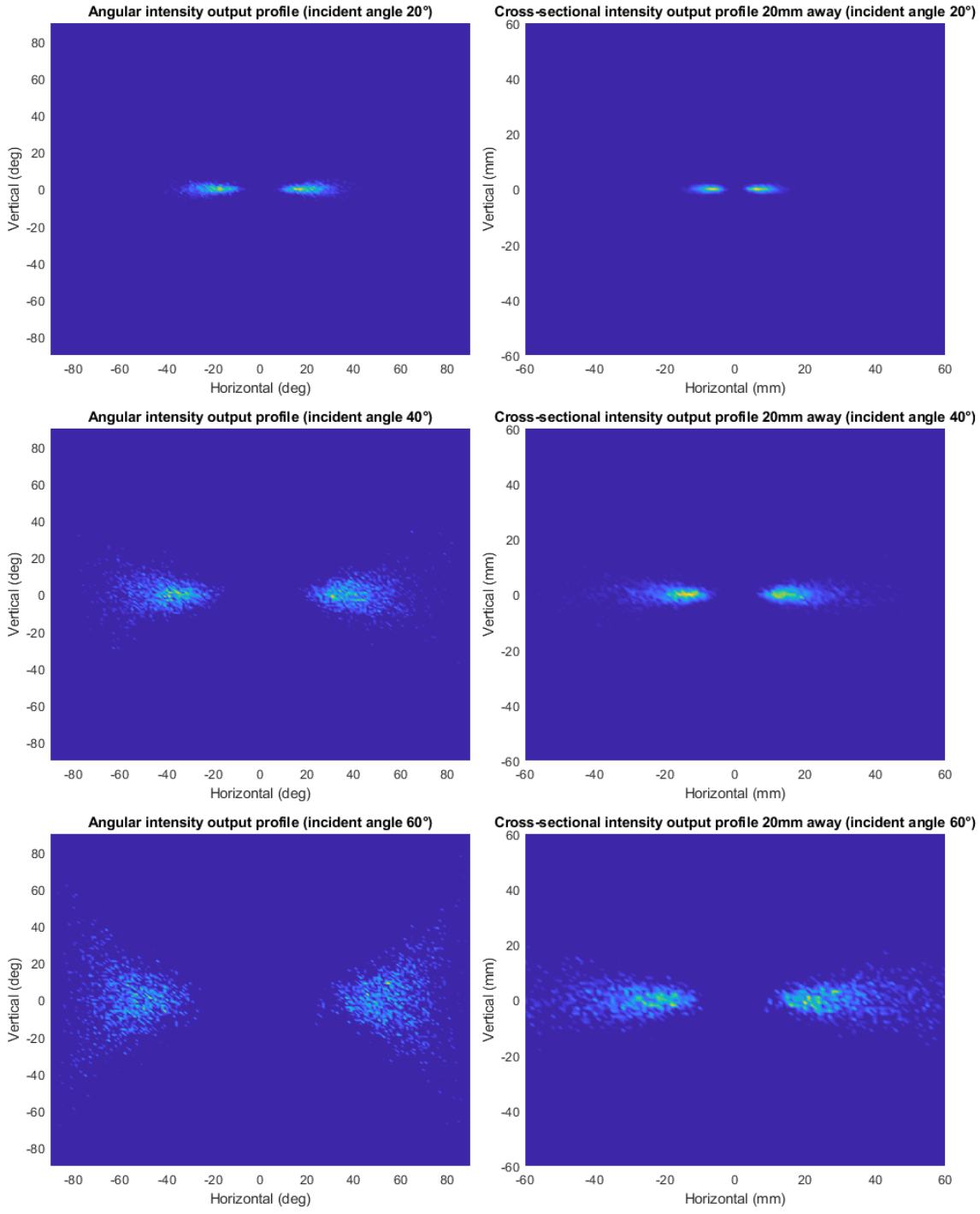

Figure D.2 Power distribution of simulated 50mm sample showing angular distribution and intensity image 20mm from output facet